

**SYNTHESIS AND ELECTROCHEMICAL STUDY OF
MnO₂-TITANIUM TITANATE NANOTUBES (TNTs)
FOR SUPERCAPACITOR APPLICATION**



**A thesis Submitted in Partial Fulfillment of the Requirements for the
Degree of Master of Science in Applied Physics
Suranaree University of Technology
Academic Year 2018**

การสังเคราะห์และศึกษาสมบัติทางไฟฟ้าเคมีของแมงกานีสออกไซด์และ
ท่อไทเทเนียมไทเทเนตเพื่อประยุกต์ใช้ในตัวเก็บประจุยิ่งยวด



นางสาววิญญา ศิวะวงศ์เกษม

วิทยานิพนธ์นี้เป็นส่วนหนึ่งของการศึกษาตามหลักสูตรปริญญาวิทยาศาสตรมหาบัณฑิต

สาขาวิชาฟิสิกส์ประยุกต์

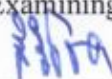
มหาวิทยาลัยเทคโนโลยีสุรนารี

ปีการศึกษา 2561

**SYNTHESIS AND ELECTROCHEMICAL STUDY OF
MnO₂-TITANIUM TITANATE NANOTUBES (TNTs)
FOR SUPERCAPACITOR APPLICATION**

Suranaree University of Technology has approved this thesis submitted in partial fulfillment of the requirements for a Master's Degree.

Thesis Examining Committee



(Assoc. Prof. Dr. Sirichock Jungthawan)

Chairperson



(Prof. Dr. Santi Maensiri)

Member (Thesis Advisor)



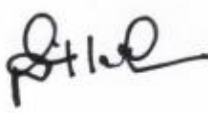
(Asst. Dr. Theeranun Siritanon)

Member

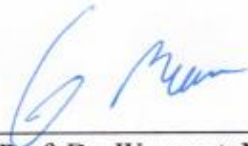


(Dr. Wittawat Saenrang)

Member



(Prof. Dr. Santi Maensiri)
Vice Rector for Academic Affairs
and Internationalization



(Assoc. Prof. Dr. Worawat Meevasana)
Dean of Institute of Science

ขวัญตา ศิวะวงศ์เกษม : การสังเคราะห์และศึกษาสมบัติทางไฟฟ้าเคมีของวัสดุแมงกานีสออกไซด์และท่อไทเทเนียมไทเทเนต เพื่อประยุกต์ใช้ในตัวเก็บประจุยิ่งยวด (SYNTHESIS AND ELECTROCHEMICAL STUDY OF MnO_2 -TITANIUM TITANATE NANOTUBES (TNTs) FOR SUPERCAPACITOR APPLICATION.) อาจารย์ที่ปรึกษา : ศาสตราจารย์ ดร.สันติ แม่นศิริ, 125 หน้า.

ไฟฟ้าเคมี/ แมงกานีสออกไซด์/ ท่อนาโนไทเทเนต/ ตัวเก็บประจุยิ่งยวด

การศึกษาวัสดุแมงกานีสออกไซด์และท่อไทเทเนียมไทเทเนตเพื่อใช้เป็นวัสดุขั้วอิเล็กโทรดในตัวเก็บประจุยิ่งยวด แมงกานีสออกไซด์และท่อไทเทเนียมไทเทเนตได้จากการสังเคราะห์ด้วยสารตั้งต้นท่อไทเทเนียมไทเทเนตและสารละลายต่างหัตถิมที่อุณหภูมิให้ความร้อนในหม้ออัดไอดีด้วยอุณหภูมิแตกต่างกัน ศึกษาผลของอุณหภูมิที่เหมาะสมโดยเริ่มที่ 60 80 100 125 และ 150 องศาเซลเซียส นาน 24 ชั่วโมง เงื่อนไขอุณหภูมิที่ให้สมบัติที่ดีที่สุดจะถูกนำไปใช้สำหรับศึกษาผลของปริมาณแมงกานีสออกไซด์ที่เหมาะสมต่อท่อไทเทเนียมไทเทเนต ซึ่งกำหนดได้จากความเข้มข้นของสารละลายต่างหัตถิมคือ 0.005 0.01 และ 0.05 โมลาร์ วัสดุท่อไทเทเนียมไทเทเนตได้จากการสังเคราะห์ด้วยวิธีการไฮโดรเทอร์มอลที่อุณหภูมิ 130 องศาเซลเซียส นาน 24 ชั่วโมง จากผงไทเทเนียมไดออกไซด์ร่วมกับสารละลายโซดาไฟที่มีความเข้มข้นสูง การวิเคราะห์และศึกษาลักษณะโครงสร้างทางสัณฐานด้วยเทคนิคต่าง ๆ ดังนี้ เทคนิคการเลี้ยวเบนด้วยรังสีเอ็กซ์ การส่องกราดและส่องผ่านด้วยกล้องลำแสงอิเล็กตรอนพร้อมศึกษาธาตุองค์ประกอบด้วยการกระจายพลังงานของรังสีเอ็กซ์ สารตัวอย่างถูกกระตุ้นด้วยพลังงานแสงช่วงแสงอินฟราเรด และเทคนิคการกระตุ้นสารตัวอย่างด้วยรังสีเอ็กซ์เพื่อวัดค่าพลังงานพันธะ ศึกษาสมบัติการดูดซับบนพื้นผิว ด้านสมบัติทางไฟฟ้าเคมีอธิบายด้วยเทคนิคไซคลิกโวลแทมเมตรี หลักการอัดและคายประจุ และการวัดค่าอิมพีแดนซ์จากการจ่ายสัญญาณไฟฟ้ากระแสสลับฟังก์ชันไซน์

ที่อุณหภูมิสังเคราะห์ 60 องศาเซลเซียส พบว่าโครงสร้างสารตัวอย่างสามารถแยกเฟสของไทเทเนียมไทเทเนตและแมงกานีสออกไซด์ได้ชัดเจน เริ่มมีการรวมเฟสที่ 80-100 องศาเซลเซียส จากนั้นเริ่มเปลี่ยนที่ 125 องศาเซลเซียส และมีกรเปลี่ยนเฟสอย่างชัดเจนที่ 150 องศาเซลเซียส เฟสเหล่านี้สัมพันธ์ไปถึงลักษณะทางสัณฐานคือ เมื่อเกิดเฟสร่วมกันอย่างสมบูรณ์จะพบว่าแม่แมงกานีสออกไซด์บางส่วนจะเกาะตามท่อแต่ยังมีกระจายอยู่ตามช่องว่างระหว่างท่อไทเทเนตด้วย โดยที่

อุณหภูมิค่านั้นไม่พบ เมื่ออุณหภูมิการสังเคราะห์สูงขึ้นจะมีการเปลี่ยนรูปร่างและขนาดอย่างชัดเจน คำนวณหาค่าพื้นที่ผิวดูดซับจำเพาะ ปริมาตรและขนาดรูพรุนของวัสดุสารตัวอย่างทั้งหมด หมู่ฟังก์ชันที่เกาะบนพื้นผิวและใน โครงสร้างของสารให้ผลว่ามีโมเลกุลของน้ำรวมอยู่ใน โครงสร้างแมงกานีสออกไซด์และท่อนาโนไทเทเนตจริง สถานะออกซิเดชันของธาตุแมงกานีสกับไทเทเนียม คือ Mn^{4+} และ Ti^{4+} เนื่องจากมีพื้นที่ผิวที่ดูดซับสูงทำให้สารตัวอย่างที่อุณหภูมิสังเคราะห์ 80 องศาเซลเซียส แสดงสมบัติทางไฟฟ้าเคมีใน โหมดไซคลิกโวลแทมเมตริกกับช่วงเวลาการคายประจุที่กว้างกว่าเงื่อนไขอื่น ค่าการกักเก็บประจุในเงื่อนไขนี้จึงคำนวณได้ค่าสูงในตัวอย่างทั้งหมด แต่ที่อุณหภูมิการสังเคราะห์ 100 องศาเซลเซียส นั้นมีความเสถียรสูงสุดเนื่องจากมีขนาดและปริมาตรรูพรุนใหญ่กว่าเงื่อนไขอื่น จากนั้นอุณหภูมิการสังเคราะห์ที่ 80 องศาเซลเซียสนี้ถูกใช้สำหรับการสังเคราะห์เพื่อศึกษาอัตราส่วนร่วมของการเพิ่มขึ้นของแมงกานีสออกไซด์ พบว่าเมื่อปริมาณแมงกานีสออกไซด์มากขึ้นพื้นที่ผิวดูดซับกลับลดลง และมีค่าการกักเก็บประจุเพิ่มขึ้นกับความเสถียรที่ 1000 รอบดีขึ้นด้วย แสดงถึงประสิทธิภาพการกักเก็บประจุของแมงกานีสออกไซด์ที่ดีกว่าท่อนาโนไทเทเนียมไทเทเนต



มหาวิทยาลัยเทคโนโลยีสุรนารี

KWUNTA SIWAWONGKASEM : SYNTHESIS AND
ELECTROCHEMICAL STUDY OF MnO₂-TITANIUM TITANATE
NANOTUBES (TNTs) FOR SUPERCAPACITOR APPLICATION
THESIS ADVISOR : PROF. SANTI MAENSIRI, D.Phil. 125 PP.

ELECTROCHEMICAL/ MnO₂/ TITANATE NANOTUBES/ SUPERCAPACITOR

Manganese oxide-Titanium Titanate nanotubes (MnO₂-TNTs) were used as electrode materials for supercapacitor applications. The synthesis process of MnO₂-TNTs is TNTs treated with KMnO₄ solution media by hydrothermal method. The reaction temperature varies on 60, 80, 100, 125, and 150 °C for 24 h. That optimization of reaction temperature was chosen to synthesis in composition ratios effect. The concentrate of KMnO₄ solution are 0.005M, 0.01M, and 0.05M used to MnO₂ variation on TNTs.

TNTs precursor were synthesized by hydrothermal method at 130 °C for 24 h. Anatase TiO₂ and highly concentrated of NaOH use as TNTs product then decorated with hierarchically MnO₂. MnO₂-TNTs were characterized by x-ray diffraction technique (XRD), scanning electron microscopy (SEM), energy dispersive spectroscopy (EDX), transmission electron microscopy (TEM), Fourier transform infrared (FTIR), x-ray photoelectron spectroscopy (XPS), and Brunauer-Emmett-Teller (BET) method. Electrochemical properties were investigated in order to the performance of electrode materials to application of supercapacitor. Cyclic voltammetry (CV), galvanostatic charge discharge (GCD) and electrochemical impedance spectroscopy (EIS) were used for explaining the capacitive behavior and

specific capacitance. The effect of hydrothermal temperature exhibits composition of $\text{H}_2\text{Ti}_2\text{O}_5 \cdot \text{H}_2\text{O}$ and Birnessite-type MnO_2 on phase formation of MnO_2 -TNTs. The phase compositions are gradually completely with 60-100°C and have change of phase with 125-150°C. These phase formations were presented that many MnO_2 in the space between nanotubes and shape of MnO_2 was changed at high temperature treatment. All of samples include with water adsorbed on surface and structure consist of hydroxyl group. However, the surface chemical composition and oxidation state showed Ti^{4+} and Mn^{4+} in all conditions. Because the highest specific surface area. CV and GCD results show best in 80°C hydrothermal temperature. At 80°C showed highest specific capacitance whereas 100°C had good capacity retention. All of composition ratios effect were synthesized at 80°C reacting temperature. The phase formations showed main peak is birnessite type MnO_2 with increase of MnO_2 content. Even though, BET surface area decreasing with high MnO_2 contents. The specific capacitances increase and high stability which caused by electrochemical effective of MnO_2 .

School of Physics

Academic Year 2018

Student' Signature Kurinta

Advisor' Signature [Signature]

ACKNOWLEDGMENT

I would like to express the deepest appreciation to my supervisor, Prof. Dr. Santi Maensiri who give constant encouragement, guidance, patience and understanding throughout and without whom it was impossible to accomplish the end task. This work had been a reaching experience for my graduate student life and research skills. I would like to thank all members at Advance Materials Physics Laboratory (AMP), kind help and support during my study at Suranaree University of Technology (SUT). They always be by my side with the comprehensive time, thesis proposal and teach the living.

I would like to thank my committee members, Assoc. Prof. Dr. Sirichock Jungthawan, Asst. Dr. Theeranun Siritanon and Dr. Wittawat Saenrang for serving on my thesis defense.

The physical support and the technical contribution of School of Physics, Institute of Science at SUT is highly appreciated, AMP Laboratory, the center for scientific and technological equipment, SUT, Synchrotron Light Research Institute (Public Organization), Nakhon Ratchasima, Thailand. Without their care and funding, it was impossible to reach the goal.

Finally, I very grateful to my family, especially parents for the continuous supported me, my sisters and grandchild for all the love and encouragement.

Kwunta Siwawongkasem

CONTENTS

	Page
ABSTRACT IN THAI	I
ABSTRACT IN ENGLISH	III
ACKNOWLEDGEMENTS	V
CONTENTS	VI
LIST OF TABLES	IX
LIST OF FIGURES	XI
LIST OF ABBREVIATIONS	XVII
CHAPTER	
I INTRODUCTION	1
1.1 Background and significance of the study.....	1
1.2 Objective of the dissertation.....	4
1.3 Scope and limitation of the study	4
1.4 Expected results	5
II LITERATURE REVIEW	6
2.1 Electrochemical capacitors	6
2.1.1 Electric double layer supercapacitors	8
2.1.2 Pseudocapacitors	10
2.2 Electrochemical study for supercapacitor	12
2.2.1 Cyclic voltammetry	13
2.2.2 Galvanostatic charge-discharge	14

CONTENTS (Continued)

	Page
2.2.3 Electrochemical impedance spectroscopy	15
2.3 MnO ₂ -TNTs as electrode materials	16
III RESEARCH METHODOLOGY	36
3.1 Materials	36
3.2 MnO ₂ -TNTs Preparation	36
3.2.1 Synthesis of TNTs precursor	36
3.2.2 Synthesis of MnO ₂ -TNTs materials	37
3.3 Basic characterization	38
3.3.1 X-ray Diffraction technique	38
3.3.2 Scanning electron microscopy	40
3.3.3 Transmission electron microscopy	43
3.3.4 Fourier Transform Infrared spectroscopy	44
3.3.5 X-ray Photoelectron spectroscopy	44
3.3.6 Brunauer-Emmett-Teller method	45
3.4 Electrochemical properties measurement	48
3.4.1 MnO ₂ -TNTs electrode fabrication	48
3.4.2 Electrochemical measurement technique	49
IV RESULTS AND DISCUSSION	51
4.1 Synthesis and characterization of TNTs precursor	51
4.2 Synthesis and characterization of MnO ₂ -TNTs samples	55
4.2.1 MnO ₂ -TNTs materials	55
4.2.2 XRD characterization of MnO ₂ -TNTs materials	56

CONTENTS (Continued)

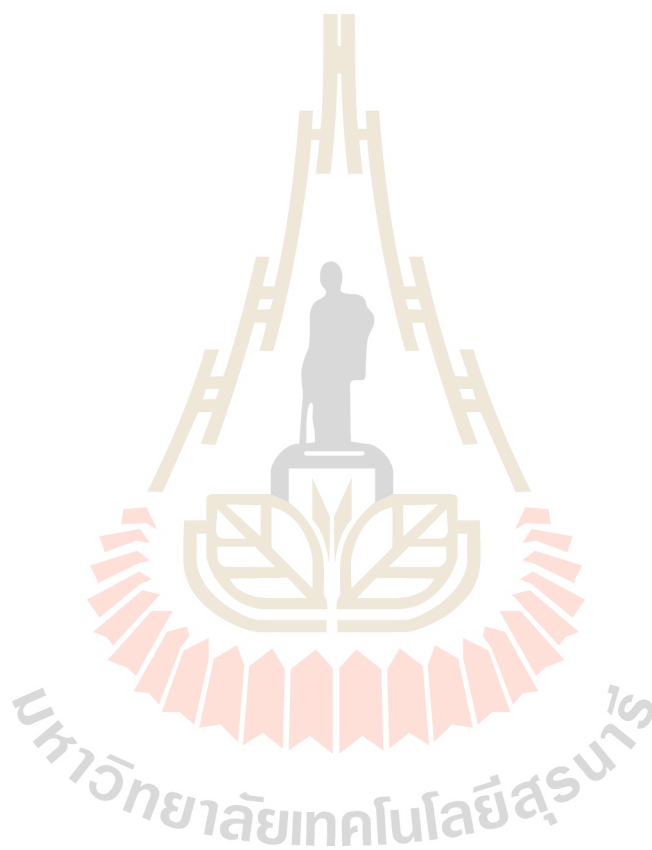
	Page
4.2.3 SEM and TEM characterization of MnO ₂ -TNTs materials	59
4.2.4 FTIR and XPS characterization of MnO ₂ -TNTs materials	65
4.2.5 Adsorption analysis of MnO ₂ -TNTs materials	79
4.3 Electrochemical properties of MnO ₂ -TNTs materials	82
4.3.1 Na ₂ SO ₄ electrolyte	82
4.3.2 The effect of hydrothermal temperatures on electrochemical properties	85
4.3.3 The effect of composition ratios of MnO ₂ -TNTs on electrochemical properties	95
V CONCLUSION	101
5.1 Synthesis of MnO ₂ -TNTs materials	101
5.2 MnO ₂ -TNTs electrode materials	102
5.3 Suggestion	103
REFERENCES	105
APPENDIX	123
CURRICULUM VITAE	125

LIST OF TABLES

Table	Page
2.1 The summarize of different types of supercapacitor on electrode materials and charge storage mechanism	12
2.2 Crystallographic form of some MnO ₂ based materials	20
2.3 Comparison of the three preparation methods for fabrication of 1D TiO ₂ -derived nanomaterial	27
2.4 List of difference TiO ₂ based electrode materials	30
2.5 Electrode materials synthesis and their the specific capacitance of MnO ₂ with TiO ₂ -based materials performed in Na ₂ SO ₄ aqueous electrolyte	34
2.6 Energy density versus power density of MnO ₂ -TiO ₂ electrode-based materials	35
3.1 IUPAC classification of pores	46
4.1 The list of absorption bands for chemical bonding are found in the FTIR spectra.....	67
4.2 Results of peak fitting for MnO ₂ -TNTs in the Mn 2p region	71
4.3 Results of peak fitting for MnO ₂ -TNTs in the Ti 2p region	73
4.4 Results of peak fitting for MnO ₂ -TNTs in the O 1s region	77
4.5 Specific surface area, pore volume and diameter of MnO ₂ -TNTs materials	81

LIST OF TABLES (Continued)

Table		Page
4.6	Fitted equivalent circuit elements of MnO ₂ -TNTs electrode materials	93
4.7	Fitted equivalent circuit elements of MnO ₂ -TNTs electrode materials	98
4.8	Comparison the specific capacitance of MnO ₂ -TiO ₂ electrode materials	100



LIST OF FIGURES

Figure	Page
2.1	The Ragone plots of various energy storage devices 8
2.2	Schematic of charge storage mechanism of an EDLC when a charge object is placed into a liquid electrolyte 9
2.3	Schematic of different charge storage mechanism of an pseudocapacitive (a) underpotential deposition, (b) redox pseudocapacitance and (c) intercalation pseudocapacitance 10
2.4	(a) CV curves and (b) GCD duration of electrochemical study 14
2.5	(a) Nyquist plot of the impedance diagram at each excitation frequency and (b) Randles equivalent circuit of electrochemical cell 16
2.6	Pseudocapacitance and electronic conductivity of alternative metal oxides 17
2.7	Crystallographic form and tunnel of MnO ₂ based materials 18
2.8	The specific capacitance, ionic conductivity, and surface area of MnO ₂ forms electrode materials were perform in 0.5M K ₂ SO ₄ electrolyte 19
2.9	Crystal structure of TiO ₂ polymorphs are (a) Rutile, (b) Anatase, (c) Brookite (orthorhombic), and (d) TiO ₂ (B) 21
2.10	Crystal structure of (a) monoclinic titanate H ₂ Ti ₃ O ₇ , (b) orthorhombic titanate H _x Ti _{2-x/4} □ _{x/4} O ₄ (□ is vacancy), (c) monoclinic titanate H ₂ Ti ₄ O ₉ . The (010) plan projection of (d) monoclinic titanate and (e) orthorhombic titanate 22

LIST OF FIGURES (Continued)

Figure	Page
2.11	Schematic diagram show (a) a presentation of displacement vector AA' when wrapping up a sheet to form a scroll-type nanotube and (b) cross sectional view of the $H_2Ti_3O_7$ trititanate nanotubes 24
2.12	Schematic drawing of the exfoliation and scrolling mechanism of nanosheets to nanotubular production 25
2.13	The flower like aggregates of (a) sodium titanate nanofiber (STNF120) and (b) Na free TiO_2 (anatase) developed by washing the STNF. (c) The phase formation of STNF as various reaction temperatures and (c) the specific capacitance as various scan rate 29
2.14	The specific capacitance of TiO_2 based electrode materials as a function of electrolytes and their morphology 31
2.15	(a-b) The TiO_2 covered with a layer of dense MnO_2 ultrathin nanoflakes and (c) the specific capacitance versus current density 33
2.16	Ragone plots of MnO_2 - TiO_2 electrode-based materials 35
3.1	Flow chart of MnO_2 -TNTs preparation by hydrothermal method 38
3.2	Diffraction of x-rays by a crystal 39
3.3	Diagram showing backscattered and secondary electron collection of these signals by the Everhart–Thornley detector 41
3.4	The principles in forming Bremsstrahlung x-ray radiation and characteristic x-ray radiation 42
3.5	The schematic structure of a transmission electron microscope 42
3.6	Diagram of photo electric effect 45

LIST OF FIGURES (Continued)

Figure	Page
3.7	Type of physisorption of isotherm and hysteresis loop 48
3.8	Electrochemical measurement setup at Advance Materials Physics Laboratory 49
4.1	(a) TNTs aqueous solution after washing process and (b) white solid prepared TNTs powder 52
4.2	(a) Morphological nanotubes of TNTs powder imaging by SEM with (b) distribution of diameter about 71 nm and (c) Ti, O and Na element composition 53
4.3	(a-b) Tubular characteristics and (c) phase of $H_2Ti_2O_5 \cdot H_2O$ for TNTs were synthesis by hydrothermal method at $130^\circ C$ for 24h (inset a is a SAED pattern) 54
4.4	The MnO_2 -TNTs aqueous form after hydrothermal treatment as (a) various temperature and (b) MnO_2 compositions 55
4.5	XRD pattern of $xMnO_2$ -TNTs ($x = 0.01M$) with different hydrothermal temperature for 24h. The pattern corresponding to $H_2Ti_2O_5 \cdot H_2O$ and MnO_2 composition phase that transform to TiO_2 anatase and $MnOOH$ phase 57
4.6	XRD patterns of $xMnO_2$ -TNTs powder was synthesized at $80^\circ C$ for 24h with a content of MnO_2 58
4.7	EM image for MnO_2 distribute on TNTs which $xMnO_2$ -TNTs ($x=0.01M$) sample were synthesized at (a) $60^\circ C$, (b) $80^\circ C$, $100^\circ C$, (c) $80^\circ C$ and (d) $150^\circ C$ for 24h 60

LIST OF FIGURES (Continued)

Figure	Page
4.8	EDX analysis of $x\text{MnO}_2\text{-TNTs}$ (where $x = 0.01\text{M}$) samples were synthesized at (a) 60°C , (b) 80°C , 100°C , (c) 125°C and (d) 150°C for 24h 61
4.9	TEM image of $x\text{MnO}_2\text{-TNTs}$ ($x = 0.01\text{M}$) were synthesized at (a-b) 60°C , (c-d) 80°C , (e-f) 100°C , (g-h) 80°C and (i-j) 150°C for 24 h. And the high magnification of TEM images (b, d, f, h, and j) 62
4.10	SEM image and EDX analysis of $x\text{MnO}_2\text{-TNTs}$ synthesized at 80°C for 24h where (a, c) $x = 0.005\text{M}$ and (b, d) $x = 0.05\text{M}$ 63
4.11	TEM image of $x\text{MnO}_2\text{-TNTs}$ where (a) $x = 0.005\text{M}$ and (c) $x = 0.05\text{M}$, and (b and d) the high magnification 64
4.12	FTIR spectra of (a) $x\text{MnO}_2\text{-TNTs}$ ($x = 0.01\text{M}$) with different hydrothermal temperatures and (b) composition ratios effect 66
4.13	XPS survey scan of (a) $x\text{MnO}_2\text{-TNTs}$ ($x = 0.01\text{M}$) with different hydrothermal temperatures and (b) a compositions effect 68
4.14	XPS Mn 2p spectra of $\text{MnO}_2\text{-TNTs}$ as (a) a function of temperatures reaction and (b) composition ratios effect 70
4.15	XPS K 2p spectra and splitting energy of $\text{MnO}_2\text{-TNTs}$ as a function of (a) temperatures reaction and (b) composition ratios effect 72
4.16	XPS measurement results of Ti 2p spectra and splitting energy of $\text{MnO}_2\text{-TNTs}$ 75

LIST OF FIGURES (Continued)

Figure	Page
4.17	XPS Na 1s spectra and splitting energy of MnO ₂ -TNTs as a function of temperature reaction and composition ratios effect 76
4.18	XPS O 1s spectra and splitting energy of MnO ₂ -TNTs as a function of temperatures reaction and composition ratios effect 78
4.19	The isotherm N ₂ adsorption and desorption of MnO ₂ -TNTs were treat with (a) different hydrothermal temperature and (b) composition ratios. 80
4.20	A pore volume distribution of MnO ₂ -TNTs materials 81
4.21	The schematic of electrochemical chamber consist of electrodes are performing in (a) 1M and (b) 0.5M Na ₂ SO ₄ solution after 1000 cycles. 82
4.22	CV curve of MnO ₂ -TNTs electrode as a function of (a) 1M and (b) 0.5M Na ₂ SO ₄ electrolyte. (c-d) CV curves obtained at low (5 mV/s) and high (100 mV/s) scan rate present the electrochemical Behavior against different Na ₂ SO ₄ electrolyte concentration 83
4.23	The GCD duration of MnO ₂ -TNTs electrode as a function of (a) 1M and (b) 0.5M Na ₂ SO ₄ electrolyte with current density of 1-5 A/g. The specific capacitance calculated from (c) CV and (d) GCD curves. (e) The capacity retention as different of Na ₂ SO ₄ electrolyte concentration after 1000 cycles 84
4.24	CV of MnO ₂ -TNTs electrode materials were synthesized at (a) 60 °C, (b) 80 °C, (c) 100 °C, (d) 125 °C and (e) 150 °C 86

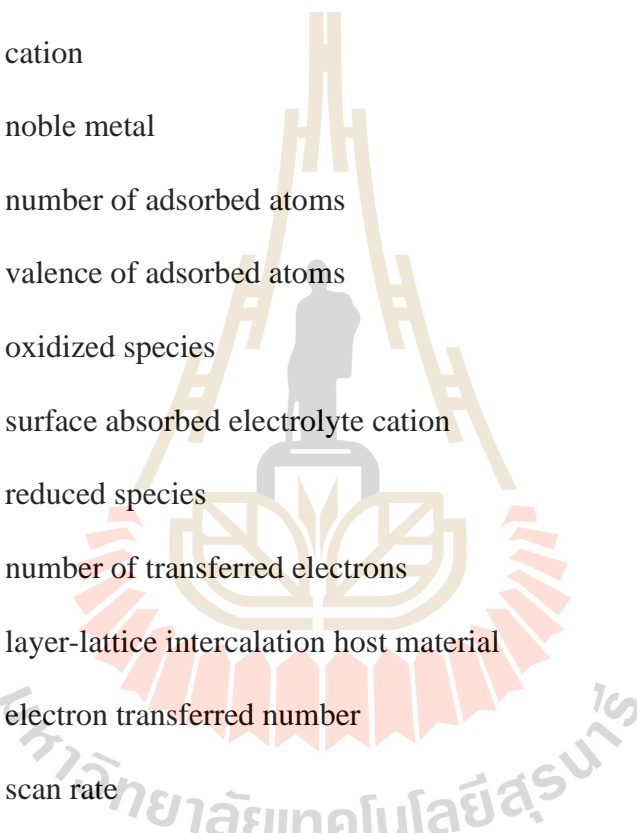
LIST OF FIGURES (Continued)

Figure	Page
4.25	GCD curve of MnO ₂ -TNTs electrode materials were synthesized (a) 60°C, (b) 80°C, (c) 100°C, (d) 125°C and (e) 150°C 87
4.26	CV curve of MnO ₂ -TNTs electrode for rating scan (a) 5 mV/s and (b) 200 mV/s 88
4.27	(a) GCD duration and (b) specific capacitance of MnO ₂ -TNTs electrode materials synthesized by different hydrothermal temperature 90
4.28	Specific capacitance related with BET surface area and of MnO ₂ -TNTs synthesized as various hydrothermal temperature 91
4.29	(a) CV curve of TNTs and TNTs treatment at 80°C and (b) specific capacitance of MnO ₂ electrode against hydrothermal temperature 91
4.30	Cycling stability of MnO ₂ -TNTs electrode materials with 1000 cycles. Capacity retention calculate from the specific capacitance of discharge time which GCD tested at 3 A/g current density 92
4.31	(a) Nyquist plot of MnO ₂ -TNTs electrode materials synthesized by different hydrothermal temperature, (b) The equivalent circuit fitted and (c) enlargement of impedance 93
4.32	Ragone plot for MnO ₂ -TNTs electrode materials as a different hydrothermal temperature 95
4.33	CV curve of MnO ₂ -TNTs electrode materials which consist with different MnO ₂ on TNTs. (a) low scan rate is 5 mV/s and (b) high scan rate is 200 mV/s 96

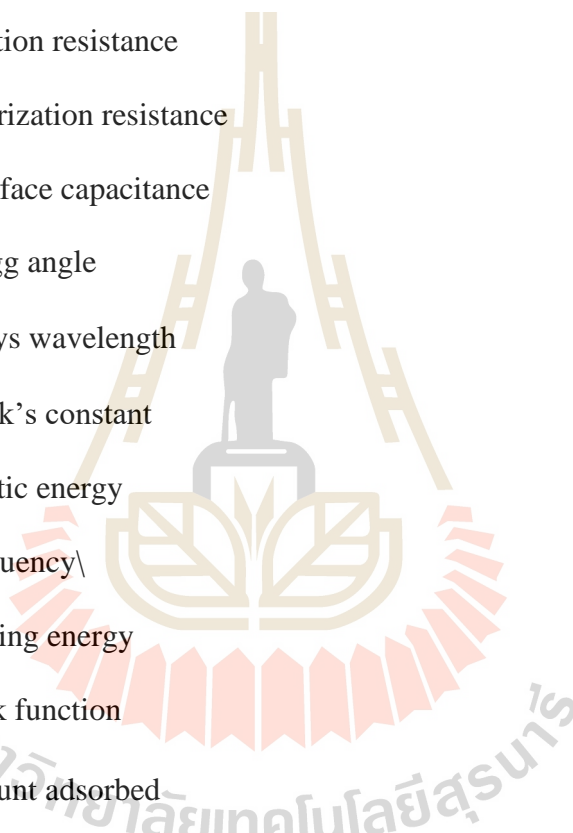
LIST OF FIGURES (Continued)

Figure	Page
4.34 (a) GCD plots and (b) the specific capacitance versus current density (0.5-5 A/g) of MnO ₂ -TNTs electrode materials which consist with different MnO ₂	96
4.35 Capacity retention of MnO ₂ -TNTs electrode materials whit different MnO ₂ content	97
4.36 (a) Nyquist plot of xMnO ₂ -TNTs electrode materials with different MnO ₂ content. (b) The equivalent circuit fitted and (c) enlargement of impedance	98
4.37 Ragone plot of MnO ₂ -TNTs electrode materials as a various of MnO ₂ contents comparation with energy storage devices	99

LIST OF ABBREVIATIONS



E	electrodes
A	anion
C	cation
M	noble metal
x	number of adsorbed atoms
z	valence of adsorbed atoms
O _x	oxidized species
C	surface adsorbed electrolyte cation
Red	reduced species
a	number of transferred electrons
MA _y	layer-lattice intercalation host material
x	electron transferred number
v	scan rate
V	voltage boundaries
C _s	specific capacitance
t	time relation
R	resistance
I	current
m	weight of active materials
C	complex capacitance

LIST OF ABBREVIATIONS (Continued)

C'	real part of complex capacitance
C''	imaginary part of complex capacitance
ω	an angular frequency
R_s	solution resistance
R_p	polarization resistance
C_{dl}	interface capacitance
θ	Bragg angle
λ	x-rays wavelength
h	Plank's constant
E_k	kinetic energy
ν	Frequency\
BE	binding energy
ϕ	work function
n_a	amount adsorbed
p/p_0	relative pressure
n_m^a	monolayer capacity
C	BET constant
A_s	specific surface areas
a_s	total surface area

LIST OF ABBREVIATIONS (Continued)

L	Avogadro constant
a_m	molecular cross section area
m	molecular weight adsorbent
V_{ads}	adsorbent of gas volume
V_m	molar volume of liquid adsorbate
R	gas constant
T	ambient temperature
χ^2	chi-squares

CHAPTER I

INTRODUCTION

1.1 Background and significance of the study

Energy sources has been limiting hence energy storage are requirement for power system. Batteries, fuel cells and electrochemical capacitors (ES) are the application areas of energy conversion and storage technology. ES also named supercapacitor or ultracapacitors could be considered as an alternative to conventional batteries. They are used in many application such as hybrid electric vehicles (Chu and Braatz, 2002), trolleybuses (Bartłomiejczyk and Mirchevski, 2014), and uninterruptible power supplies (UPS) (Zhan *et al.*, 2015). ES is a component that can store and accommodate certain amount of energy in a very short time (Libich *et al.*, 2018), high-power density, long life cycle and fast charging rate. A type of ES includes electrochemical double layer capacitor (EDLC) and pseudocapacitor (faradaic supercapacitors). These based on charge storage mechanism of surface reaction at the electrode materials/electrolyte interface and faradaic redox reactions occurs into the surface of electrode materials (Wang *et al.*, 2012). The specific capacitance and energy density are depend on surface area of carbon electrode materials (Liu *et al.*, 2013). Transition metals oxide use as pseudocapacitive electrode materials show faradaic processes on oxidation states for electron transferring during faradaic reactions with the

reversible adsorption, redox reactions and reversible electrochemical doping-dedoping (Conway and Pell, 2003). In general, morphologies of material can tailor the specific surface area which shortens the path of ions and electrons contribute to improvement of electrochemical supercapacitor performance. Previous report, the nanorod showed high specific capacitance more than nanosphere, nanosheet and nanoflower because of their specific surface area (Ye *et al.*, 2017). The cost and environmental effect are significant key in practical applications. Titanium dioxide (TiO_2) is the most attention of transition metals oxide materials. The hollow nanotubes allowed the ions to diffusion with a short distance that interlayer positions providing a large specific surface area. This is a prerequisite for electrochemical pseudocapacitance more than nanorod structure (Zhang *et al.*, 2008). Titanium Titanate nanotubes (TNTs) is 1-dimensional nanostructured TiO_2 materials that was studied after discovery of the carbon nanotubes (Cesano *et al.*, 2009). Nanotube materials have intrinsic multifunctionality because of tube opening, inner, outer and interstitial regions. The cost productions, chemical stability, friendly material, large surface area, ion-exchangeable and wide band gap are factor of semiconducting materials. The potential applications of TNTs are electrode materials in dye-sensitized solar cells (Yun *et al.*, 2014), lithium anode material (Fang *et al.*, 2008), methanol fuel cells (Mohamed *et al.*, 2016), hydrogen chemical sensing (Sikhwivhilu *et al.*, 2012), photocatalytic activity (Shi *et al.*, 2014), photochromic (Miao *et al.*, 2007), thermoelectric (Miao *et al.*, 2010), and dielectric materials (Hu *et al.*, 2009). Many methods to TNTs synthesized by example surfactant-assisted self-assembly (Shen *et al.*, 2006), organogel template (Jung *et al.*, 2002), and hydrothermal method which most interested because simplicity methods and growth of large area number (Shi *et al.*, 2014; Vu *et al.*, 2014; Zhang *et al.*, 2007; Manfroi *et al.*, 2014).

TNTs was formed through dissolution of TiO_2 raw materials, accompanied by growth sodium TNTs layered sheets, then sheets exfoliation and folding into tubular structures. The large surface area due to layer and tunnel of Na-TNTs can be used as new electrode materials for high energy and power densities, anode materials for hybrid Na-ion capacitor and high performance in asymmetric supercapacitors. Nevertheless, the poor electrical conductivity of electrode materials is a key factor for enhancing the performance of electrode materials.

Manganese oxide (MnO_2) is one of based material which has been much attention use as electrode material due to high theoretical specific capacitance of 1370 F/g. High specific capacitance value is expected that from redox process involving one electron per manganese atom (Lang *et al.*, 2011; Toupin *et al.*, 2004). And their low cost, structural flexibility, nature abundance, and environmentally (Ye *et al.*, 2017). There are many technique in MnO_2 synthesized as sol-gel (Ching *et al.*, 1997), high temperature decomposition (Gaillot *et al.*, 2003), microwave assisted emulsion (Yu *et al.*, 2009), and hydrothermal method (Zhang *et al.*, 2014). However, the electrochemical performance of MnO_2 were improved through the control of electronic conductivity and densely packed behavior without porous structure. Therefore, the various substrates with large surface area and high electronic conductivity have been used to composite MnO_2 material for improving their electrochemical properties.

Here, MnO_2 -TNTs materials were interested to study owing to MnO_2 is alternative metal oxides with highly theoretical specific capacitance. While TNTs substrate expected that composited MnO_2 improving the performance of electrode material. MnO_2 -TNTs electrode material focus on the effect of phase structure with

hydrothermal treatment temperature relation and the composition ratios effect between MnO_2 and TNTs to electrochemical properties.

The phase structure, morphology, composition, and surface adsorption were investigated by x-ray diffraction (XRD), scanning electron microscopy (SEM), energy dispersive x-ray microscopy (EDX), transmission electron microscopy (TEM), Fourier transform infrared spectroscopy (FTIR), x-ray photoelectron spectroscopy (XPS) and Brunauer-Emmett-Teller (BET) method. Cyclic voltammetry (CV), Galvanostatic charge-discharge (GCD), and the electrochemical impedance spectroscopy (EIS) uses for explaining the electrochemical properties.

1.2 Objective of the dissertation

- 1.2.1 To synthesize the electrode material of MnO_2 -TNTs by hydrothermal method.
- 1.2.2 To characterize the prepared MnO_2 -TNTs materials by XRD, SEM, TEM, FT-IR, BET, and XPS techniques.
- 1.2.3 To study the electrochemical properties of the MnO_2 -TNTs electrode materials.

1.3 Scope and limitation of the study

- 1.3.1 The effect of temperature and composition ratios in MnO_2 -TNTs material synthesized by hydrothermal method.
- 1.3.2 The crystal structure, morphology, and composition are investigated.

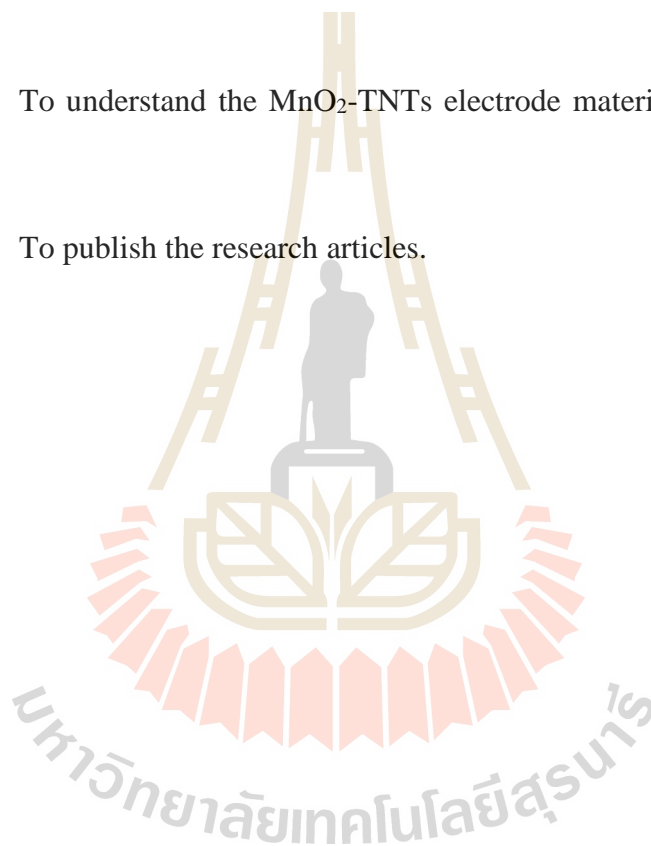
1.3.3 The electrochemical properties of MnO_2 -TNTs electrode material are explained.

1.4 Expected results

1.4.1 To improve the skill in synthesis and characterization of MnO_2 -TNTs materials.

1.4.2 To understand the MnO_2 -TNTs electrode material on electrochemical properties.

1.4.3 To publish the research articles.



CHAPTER II

LITERATURE REVIEW

2.1 Electrochemical capacitors

Ideal capacitor consists of two parallel electrodes separated by non-conductive materials. A voltage is applied across the capacitor, during charging the positive and negative charges are migrated to opposite's polarity of surface of electrodes. The ratio of electric charge (Q) on each electrode to the voltage (V) difference between them that is

$$C = \frac{Q}{V} \quad (1)$$

where C is an electrical capacitance with directly proportional to the area (A) of each electrode. The medium dielectric constant (ϵ) are inversely to a distance (D) between the electrodes present as

$$C = \frac{\epsilon_0 \epsilon_r A}{D} \quad (2)$$

where ϵ_0 is the permittivity of free space and ϵ_r is dielectric constant of the material between the plates (Libich *et al.*, 2018). Energy and power densities are primary parameter for determining capacitor of a quantity per unit weight or per unit volume. The energy is a quantity can be stored in capacitor was calculate by equation (3), it will enhanced by varying the voltage or the capacitance of electrode materials (Yassine and Fabris, 2017).

The power density derived from energy per unit time present as in equation (4) derived from energy per unit time present as in equation (4) which illustrate the rate of energy delivery. Considering with the resistance of component are often matched with impedance that give rise to equation (5)

$$E = \frac{1}{2} C \Delta V^2 \quad (3)$$

$$P = \frac{E}{\Delta t} \quad (4)$$

$$P_{\max} = \frac{V_{\max}^2}{ESR} \quad (5)$$

where E is energy density, C is capacitance, V is voltage, P is power density, Δt is time, and ESR is equivalent series resistance.

Special kind in energy storage device is high power and energy densities which based on principles of conventional capacitor. ES provided by a function of energy and power densities are represented in horizontal and vertical axes, respectively. Also called Ragone plots as show in Figure 2.1(a) (Hameer and Niekerk, 2015). There is a combination of traditional capacitor and battery/fuel cell with high power and relate to low energy density. Supercapacitors is very attend with their long life cycles and high charge rates (González *et al.*, 2016).

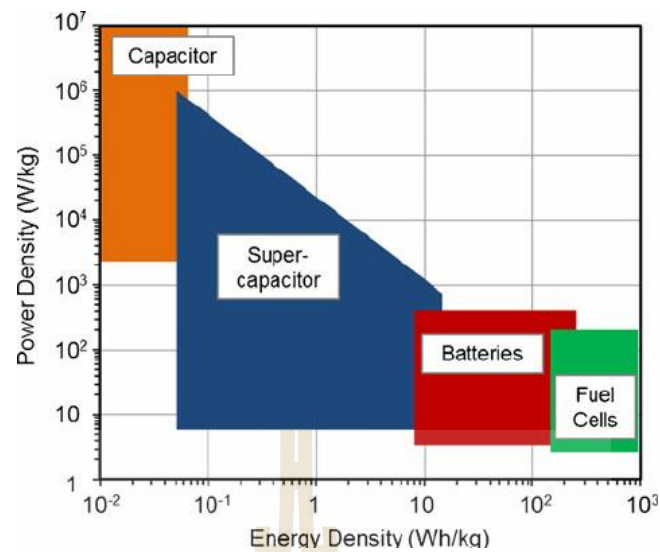


Figure 2.1 The Ragone plots of various energy storage devices (Meng *et al.*, 2013).

2.1.1 Electric double layer supercapacitors

EDLC or electrostatic supercapacitor is similar to traditional capacitor for charging separation. There has been higher substantially amount of energy because the charge separation take place across very small distance in the electrical double layer. Interphase of electrode, electrolyte and other the charge large number can be stored by extended surface area of electrode materials (Pandolfo and Hollenkamp, 2006). When charging the electrons travel from the negative electrode to the positive electrode through external load. The cations from electrolyte move towards the negative electrode while the anions move toward positive electrode. These reverse take place during discharge. A typical of electrochemical supercapacitors divided by charge transfers across the electrode/electrolyte interface. This without ion exchanges occur between the electrode and electrolyte. The concentration of electrolyte constant during charge and discharge processes refer to energy stored in the double layer interface (Wang *et al.*, 2012).

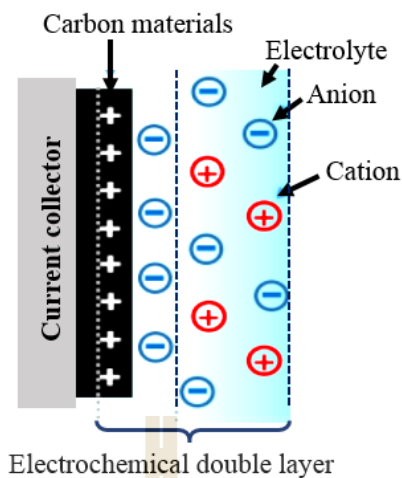


Figure 2.2 Schematic of charge storage mechanism of an EDLC when a charge object is placed into a liquid electrolyte (Shao *et al.*, 2018) .

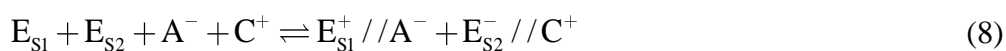
Energy storage mechanism between two electrode and electrolyte in electrochemical processes can be expressed (Zheng *et al.*, 1997; Vol'fkovich and Serdyuk, 2002) as follow equation at one positive electrode:



one negative electrode:



and the overall charging-discharging process:



where the two electrodes can be noted as E_{S1} and E_{S2} , an anion as A^{-} , a cation as C^{+} , and the electrode/electrolyte interface as //, respectively.

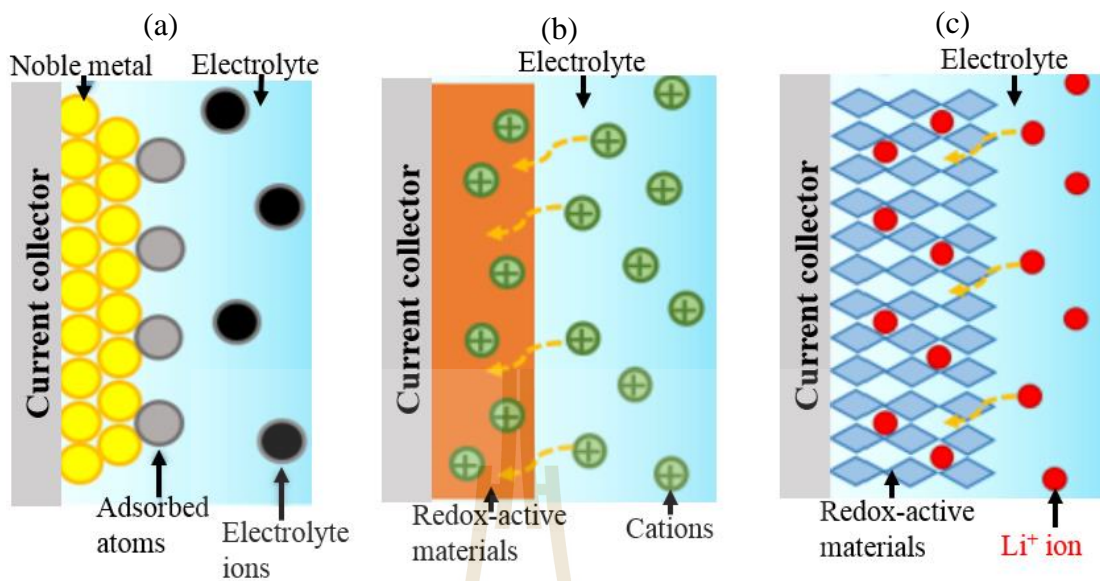


Figure 2.3 Schematic of different charge storage mechanism of an pseudocapacitive (a) underpotential deposition, (b) redox pseudocapacitance and (c) intercalation pseudocapacitance (Shao *et al.*, 2018).

2.1.2 Pseudocapacitors

Different type of charge storage mechanism of a pseudocapacitive arise by underpotential deposition, redox pseudocapacitance, and intercalation/insertion. Well known for the adsorption of hydrogen atom on catalytic noble metal along with the electrodeposition of metal cations described by



where M is noble metal, x is number of adsorbed atoms, z is the valence of adsorbed atoms, and xz is number of transferred electrons. Redox pseudocapacitance based on electron transfer between an oxidized species and a reduced species. Cations adsorption on oxidized species surface with fast and reversible electron transfer cross the interface between the electrode and electrolyte as show



where Ox is oxidized species, C is the surface absorbed electrolyte cations, Red is reduced species, and a is number of transferred electrons. Intercalation/insertion are also occurred by metal valence change to maintain electric neutrality as



where MA_y is the layer-lattice intercalation host material and x are the electron transferred number. This a cation intercalation pseudocapacitance as transitional behavior between Li-ion batteries and supercapacitor (Shao *et al.*, 2018). Three reactions in pseudocapacitive are occurred at electrode. The first is surface reversible adsorption of ions from the electrolyte. The second type is redox reactions that involve ions from the electrolyte which depend on surface mechanism and surface area. Other type is doping-dedoping of electrically conducting polymers in the electrode (Wang *et al.*, 2012).

Asymmetry or hybrid electrochemical capacitor, there are asymmetric hybrid, symmetric composite hybrid, and battery-like hybrid. Asymmetry concept is one electrode consists of electrostatic material while the other consists of faradaic capacitance material. The different electrode materials can be used for improving the performance of supercapacitor for overall cell voltage, power and energy density. Summary of types of supercapacitor devices present as Table 2.1.

Table 2.1 The summarize of different types of supercapacitor on electrode materials and charge storage mechanism (Zhi *et al.*, 2013).

Supercapacitor	Electrode material	Charge storage mechanism
1). EDLC	Carbon	Electrochemical double layer (EDL) and non-Faradaic process
2). Pseudocapacitor	Metal oxide, conducting polymer	Redox reaction, Faradaic process
3). Hybrid capacitor -asymmetric hybrid	Anode: pseudo capacitance materials, cathode: Carbon	Anode: redox reaction, cathode: EDL
-symmetric composite hybrid	Metal oxide/Carbon, conducting polymer/Carbon	Redox reaction plus EDL
-battery-like hybrid	Anode: Li-insertion materials, cathode: Carbon	Anode: Lithiation/delithiation, cathode: EDL

2.2 Electrochemical study for supercapacitor

The electrochemical properties were evaluated by transient technique such as cyclic voltammetry, chronopotentiometry, and chronoamperometry, etc. Stationary technique such as electrochemical impedance spectroscopy, and rotating disk electrode, etc. Electrochemical cell comprises three-electrodes configuration are the counter electrode (CE) and the working electrode (WE). The current flows through CE and WE

before voltage is measured (or controlled) in comparison with the reference electrode (RE) and WE. The RE used in ideal nonpolarizable behavior reveal that constant voltage over large current densities. This WE voltage is accurately measured (or controlled) (Lu, 2013).

2.2.1 Cyclic voltammetry

Cyclic voltammetry (CV) is technique that explains the surface and electrolyte reaction of supercapacitance behavior, this possible to measure the voltage window of an electrode. The principle is applying a linear voltage ramp to electrode by two voltage limits. Current-voltage curve is usually obtained present as in Figure 2.4(a). The applied voltage is as follows

$$V(t) = V_0 + vt \quad \text{for } V \leq V_1 \quad (12)$$

$$V(t) = V_0 - vt \quad \text{for } V \geq V_2 \quad (13)$$

where V_1 and V_2 are the boundary of voltage window and v is the voltage scan rate (V/s). The volume metric specific capacitance can be calculated as

$$C = \int_{V_1}^{V_2} \frac{I}{v} dV \quad (14)$$

where C is the specific capacitance and dV is the integral area of current (I) with respect to V . However, CV technique is useful to explain the qualitative and kinetic analysis via cycling and can be calculated their capacitance. But in the laboratory cells are difficulty to handle with large device. Galvanostatic cycling is better in experiments and can extend to industrial.

2.2.2 Galvanostatic charge-discharge

Galvanostatic charge-discharge (GCD) technique is a method most used in determining the specific capacitance, cycle lifetime, energy, and power density of supercapacitor. GCD is also called chronopotentiometry that current applied and the voltage is detected as a function of time as in Figure 2.4(b). The voltage variation is

$$V(t) = Ri + \frac{t}{C}i \quad (15)$$

$$R = \frac{V_{\text{drop}}}{\Delta I} \quad (16)$$

where V is the voltage potential (V), C is specific capacitance (F/g), t are time relation and R is the series resistance (Ω) deduced from the voltage drop (V_{drop}) occurring over the current inversion (ΔI). The specific capacitance was calculated by following relations as

$$C_s = \frac{\Delta I \times \Delta t}{\Delta V \times m} \quad (17)$$

where I , Δt , ΔV , and m are the constant current (A), time (s), the total potential difference (V), and the weight of active materials (g), respectively.

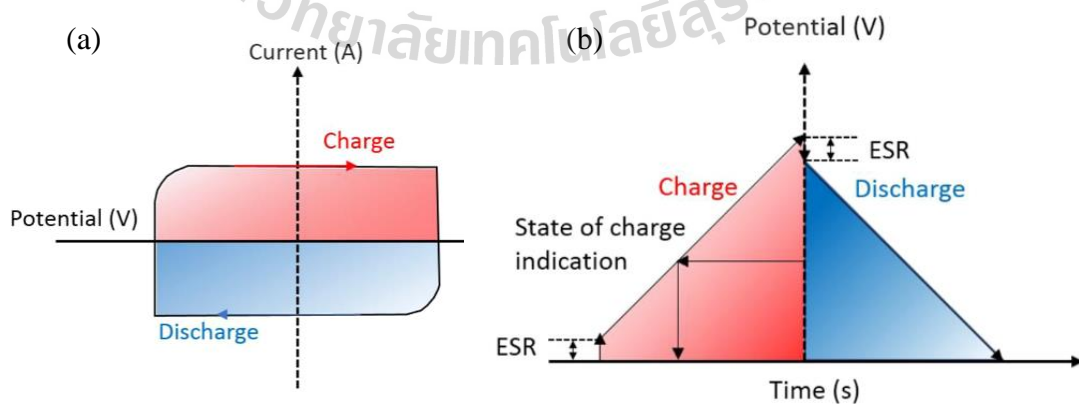


Figure 2.4 (a) CV curves and (b) GCD duration of electrochemical study (Shao *et al.*, 2018).

2.2.3 Electrochemical impedance spectroscopy

Electrochemical impedance spectroscopy (EIS) useful tool for explaining the electrode-electrolyte interface and the properties of electrode materials. The small amplitude alternative voltage signal was applied to cell with the wide frequency range fin analyze electrical characteristic. The impedance response was recorded and normally show as Nyquist plots which illustrated the imaginary and real impedance or resistance. An alternative approach is to consider the complex capacitance as

$$C'(\omega) = C''(\omega) + jC''(\omega) \quad (15)$$

$$C'(\omega) = \frac{Z''(\omega)}{\omega|Z(\omega)|^2} \quad (16)$$

$$C''(\omega) = \frac{Z'(\omega)}{\omega|Z(\omega)|^2} \quad (17)$$

where $C'(\omega)$ and $C''(\omega)$ are the real and imaginary part of complex capacitance $C(\omega)$, $Z'(\omega)$ and $Z''(\omega)$ are the real and imaginary part of complex impedance $Z(\omega)$ while ω is an angular frequency (Taberna *et al.*, 2003). Nyquist plots format on electrochemical impedance data also known as a Cole-Cole plot or a complex impedance plane plot. Where R_s is the solution resistance, R_p is the polarization resistance and C_{dl} is interface capacitance. Figure 2.5 is Nyquist plot and randles circuit show as

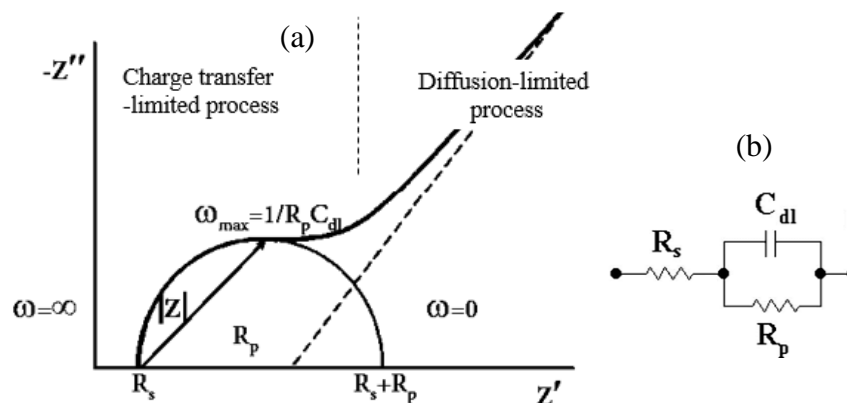


Figure 2.5 (a) Nyquist plot of the impedance diagram at each excitation frequency and (b) equivalent circuit of electrochemical cell (Fernández-Sánchez *et al.*, 2005).

2.3 MnO₂-TNTs as electrode materials

Ideal electrode materials require to high specific surface area for conducting specific capacitance. Porosity affects the specific capacitance and rate capability meanwhile electronic conductivity is role to rate capability and power density. In addition, the stability of thermal and chemical are significant in cyclic stability. Focused on pseudocapacitance materials are suitable with electroactive site for charging storage mechanism. As Figure 2.6 the metals oxide are considered by theoretical capacitance and electronic conductivity relation. RuO₂ is highest conductivity whereas highest capacitance in the Co₃O₄. Thus, capacitance of electrode material depending with many parameter as system testing or effective of electrolyte ions (Zhi *et al.*, 2013). However, MnO₂ is alternative electrode materials that high theoretical specific capacitance. MnO₂ based materials exhibit different dimensional arrangements built on MnO₆ Octahedra assemblies. MnO₆ share their corners, face and edges to channeled (1D), layered (2D) and interconnected (3D) as Figure 2.7

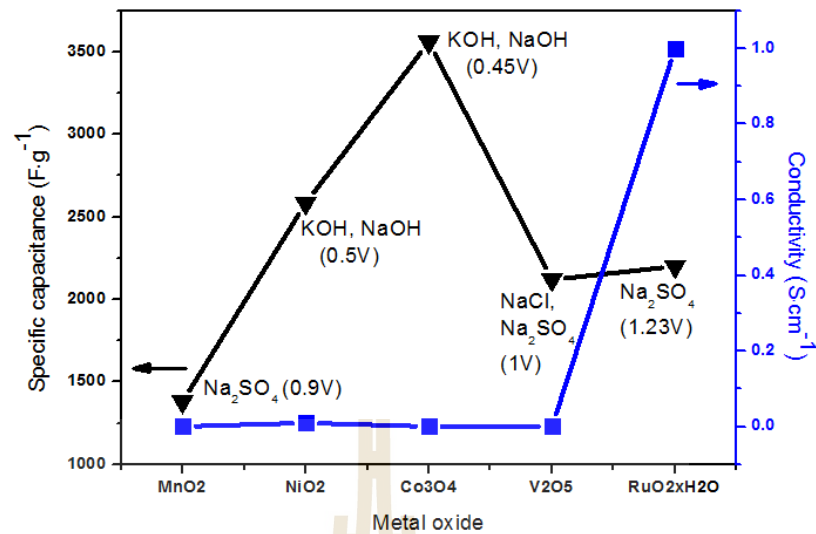


Figure 2.6 Pseudocapacitance and electronic conductivity of alternative metal oxides (adapted from Zhi *et al.* (2013)).

Ghodbane *et al.* (2009) reported MnO₂ electrode materials were study on microstructural effect. The crystallographic of MnO₂ pyrolusite, ramsdellite, cryptomelane, Ni-todorokite, Octahedra molecular sieve (OMS-5), birnessite, and spinel show as figure 2.7(a-g). Figure 2.8 shows the largest specific capacitance relatively with the highest specific surface area in spinel form. In spite of the OMS-5 shows highest ionic conductivity. Among of various form, the 3D microstructure shows highest value of specific capacitance and followed by 2D and 1D.

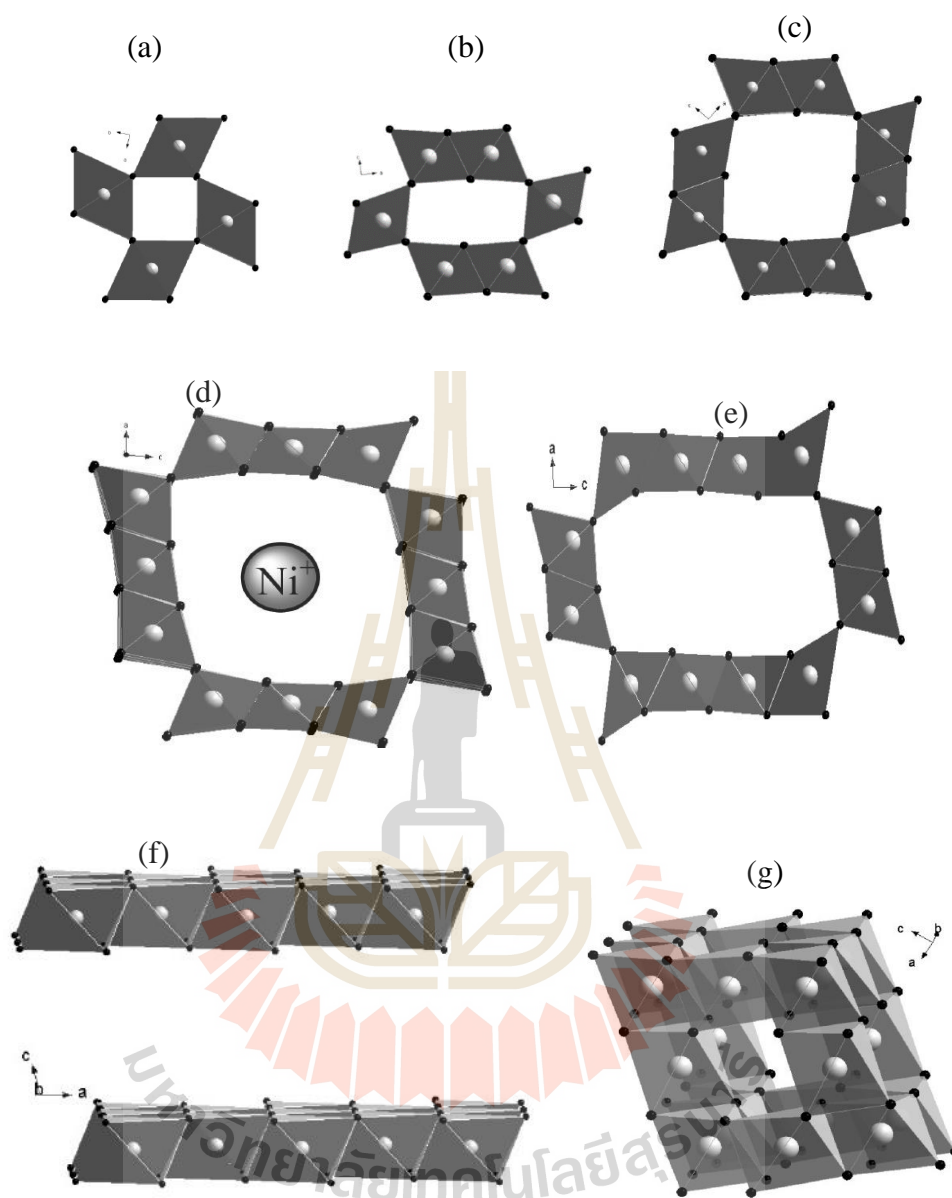


Figure 2.7 Crystallographic forms of MnO₂ based materials (Ghodbane *et al.*, 2009).

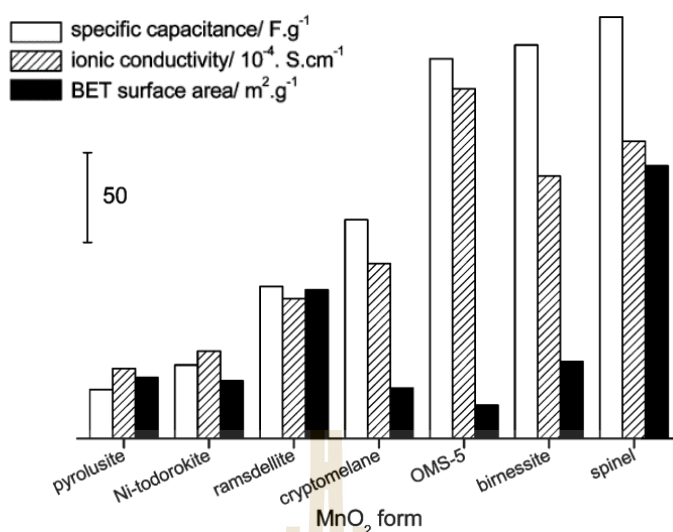


Figure 2.8 The specific capacitance, ionic conductivity, and surface area of MnO₂ forms electrode materials were performed in 0.5M K₂SO₄ electrolyte (Ghodbane *et al.*, 2009).

Generally, Birnessite-type MnO₂ may be called manganous-manganite or δ-MnO₂ are most common form that poorly crystalline oxide of tetravalent manganese. δ-MnO₂ is composed of ions such as Na, Ca, and K etc. which are nonessentials (McKenzie, 1971). The δ-MnO₂ has been lamellar layered structure with MnO₆ octahedra layer for intercalated the different species within. δ-MnO₂ nanoflower was assembled by hierarchical of nanosheets for shorten transport path length of electrons and cations. They were constructed by hydrothermal method with different KMnO₄ proportional. The specific capacitance of MnO₂ derived from high KMnO₄ concentration more than at low concentration. This ascribe to the multi branched hierarchical self-assembled with very thin nanosheets structure for large contact area with electrolyte ions (Zhao *et al.*, 2015). The morphology effected γ-MnO₂ which contains pyrolusite and ramsdellite on supercapacitor application. The nanorod show

highest specific capacitance followed with nanoflower, nanosheets and nanosphere since the high crystallization and specific surface area (Ye *et al.*, 2017).

Table 2.2 Crystallographic form of some MnO₂ based materials (Ghodbane *et al.*, 2009; Ye *et al.*, 2017).

Compound	Mineral	Crystal symmetry	Features
α -MnO ₂	Hollandite	Tetragonal (I4/m)	(2×2) tunnel
R-MnO ₂	Ramsdellite	Orthorhombic (Pbnm)	(1×2) tunnel
β -MnO ₂	Pyrolusite	Tetragonal (P42/mnm)	(1×1) tunnel
γ -MnO ₂	Nsutite	Complex tunnel	(2×2)/(1×2)
δ -MnO ₂	Birnessite	Rhombohedral (R-3m)	(1×∞) layer
Mg-Bir	Mg-Birnessite	Monoclinic (C2/m)	(1×∞) layer
Na-Bir	Na-Birnessite	Monoclinic (C2/m)	(1×∞) layer
ϵ -MnO ₂	Akhtenkite	Hexagonal (P63/mmc)	Dense stack
λ -MnO ₂	Spinel	Cubic (Fd3m)	(1×1) tunnel
ψ -MnO ₂	Psilomelane	Monoclinic (P2/m)	(2×3) tunnel
T-MnO ₂	Todorokite	Monoclinic (P2/m)	(3×3) tunnel

The Charge storage mechanism of MnO₂ electrode used in aqueous electrolyte consists of intercalation/deintercalation and surface adsorption. The intercalation/deintercalation of protons (H⁺) or metal cations (C⁺) such as Li⁺, K⁺, Na⁺ from the electrolyte into the bulk structure of material. The reaction was described by



or metal cations



The surface adsorption of electrolyte C^+ on MnO_2 can be expressed as



this mechanism was proposed to a redox reaction in MnO_2 electrode via the III and IV oxidation state of Mn (Toupin *et al.*, 2004).

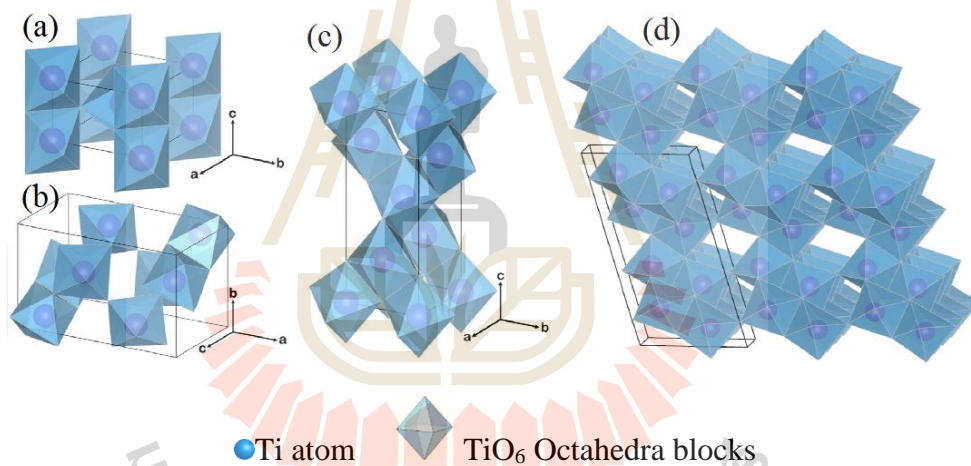


Figure 2.9 Crystal structure of TiO_2 polymorphs are (a) Rutile, (b) Anatase, (c) Brookite (orthorhombic), and (d) $\text{TiO}_2(\text{B})$ (Zhang *et al.*, 2015).

TiO_2 -based material including three distinct polymorphs are rutile, anatase, and brookite as figure 2.9. The crystallinity structures have been titanium cations are six-fold coordinated to oxygen anions, formed distorted TiO_6 octahedra joined by sharing the octahedra edges (some have corner sharing well). The different type of crystal structure provided by structural package in the TiO_6 octahedra building blocks. The rutile, anatase, and pure titania or called $\text{TiO}_2(\text{B})$ are the same chemical formula TiO_2 .

While $\text{TiO}_2(\text{B})$ structural are very open crystal structure and shares more similarity with titanate than other phase.

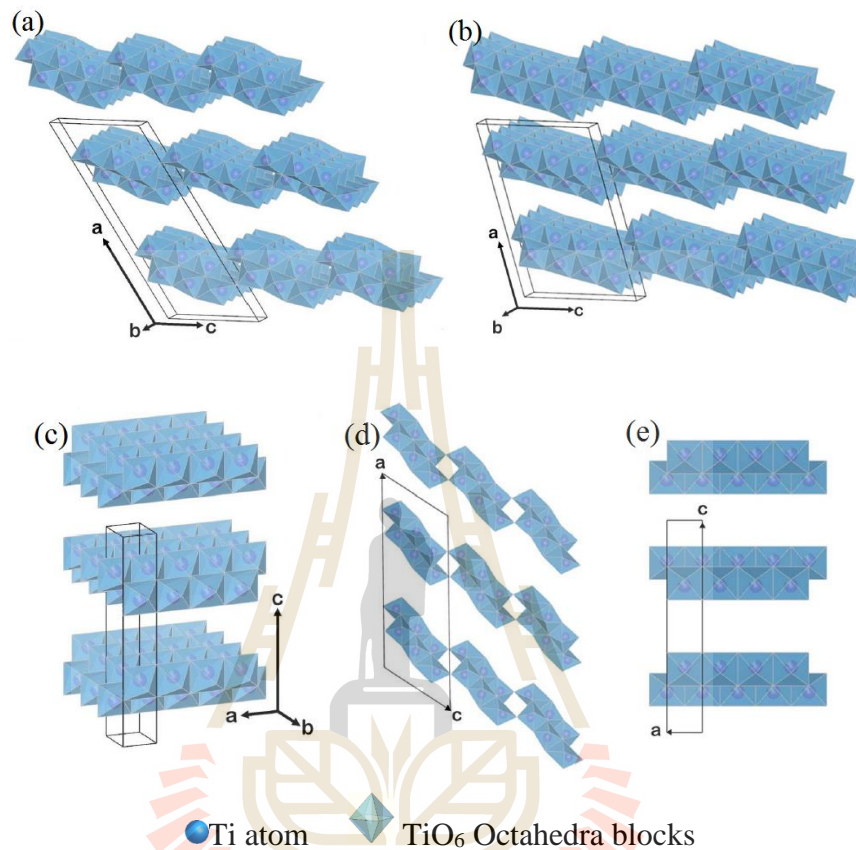


Figure 2.10 Crystal structure of (a) monoclinic titanate $\text{H}_2\text{Ti}_3\text{O}_7$, (b) orthorhombic titanate $\text{H}_x\text{Ti}_{2-x/4}\square_{x/4}\text{O}_4$ (\square is vacancy), (c) monoclinic titanate $\text{H}_2\text{Ti}_4\text{O}_9$. The (010) plan projection of (d) monoclinic titanate and (e) orthorhombic titanate (Zhang *et al.*, 2015).

Normally, Layered titanate material is similar formula as $\text{M}_x\text{Ti}_y\text{O}_{x/2+2y}\cdot z\text{H}_2\text{O}$ (where $\text{M} = \text{H}, \text{Li}, \text{Na}, \text{K}, \text{etc.}$). The structure is 2D layers constructed by connected TiO_6 octahedra blocks which inter-layer spaces confine cation and neutral molecules. Based on crystal symmetry can be divided into monoclinic and orthorhombic. Monoclinic titanate is zigzag layers built upon the structural entity which composed of several collinear edge-sharing TiO_6 octahedra in the (010) plans. The variation

stoichiometry of monoclinic titanate that related to the number of TiO_6 octahedra composing in the structural entity. For example, $\text{H}_2\text{Ti}_3\text{O}_7$ is 3 octahedra blocks entity while $\text{H}_2\text{Ti}_4\text{O}_9$ structure entity has 4 octahedra blocks represent as in Figure 2.10(a) and 2.10(b), respectively. Figure 2.5(c) is orthorhombic crystal structure which frequently termed lepidocrocite titanate. The TiO_6 octahedra arrangement in orthorhombic titanate is closely related to monoclinic titanate visualization. The direction of orthorhombic titanate layer is straight and continuous for the absence of corner-sharing and charge balance must be maintained from partial occupancy of Ti sites. These difficult to predict because their low crystallinity and structural similarity in close characteristic XRD peak positions (Zhang *et al.*, 2015). However, TNTs structure have been wide variety of possible compositions such as $\text{Na}_2\text{Ti}_3\text{O}_7$, $\text{H}_2\text{Ti}_3\text{O}_7$, $\text{Na}_x\text{H}_{2-x}\text{Ti}_3\text{O}_7$, $\text{Na}_x\text{H}_{2-x}\text{Ti}_3\text{O}_7 \cdot n\text{H}_2\text{O}$, $\text{Na}_2\text{Ti}_2\text{O}_4 \cdot (\text{HO})_2$, $\text{Na}_2\text{Ti}_2\text{O}_4 \cdot (\text{HO})_2$, $\text{Na}_2\text{Ti}_2\text{O}_5 \cdot \text{H}_2\text{O}$, $\text{H}_2\text{Ti}_2\text{O}_5 \cdot \text{H}_2\text{O}$ or even the lepidocrocite-type titanates with compositions of $\text{Na}_x\text{Ti}_{2-x/4}\text{O}_4$ or $\text{H}_x\text{Ti}_{2-x/4}\text{O}_4$.

1D nanostructure as titanate nanotubes with crystal structure belongs to monoclinic or orthorhombic system. A Long cylinder with a hollow cavity lying through the center along their length. The crystallite size is very small, close similarity, and the precise position of hydrogen atom inside in the crystals is difficult to find. The walls of titanate nanotubes always multilayered and the number of layers varies from two to ten and tubular scrolled like onion or concentric in type.

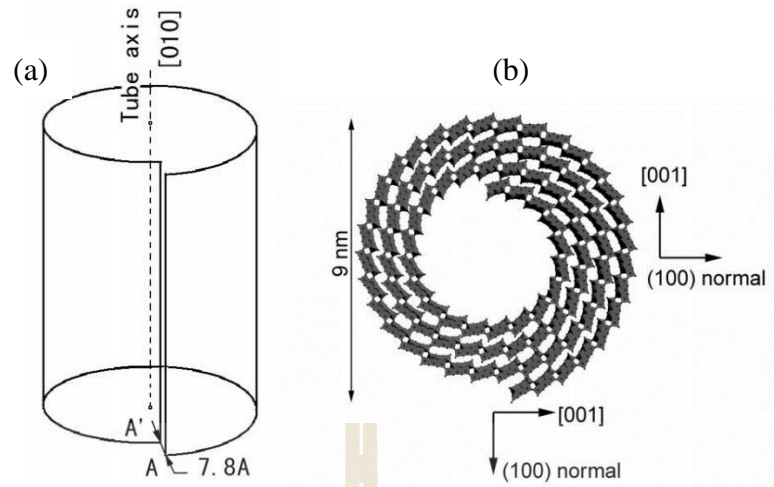
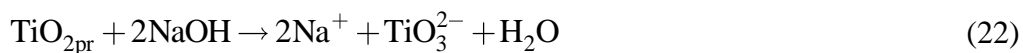


Figure 2.11 Schematic diagram show (a) a presentation of displacement vector AA' when wrapping up a sheet to form a scroll-type nanotube and (b) cross sectional view of the $\text{H}_2\text{Ti}_3\text{O}_7$ trititanate nanotubes (Chen *et al.*, 2002).

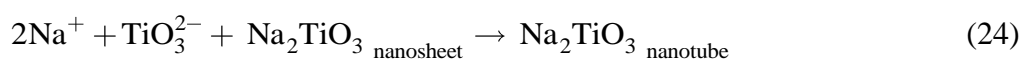
The formation of TNTs, Ti-O-Ti bonds of the TiO_2 powder is broken under the action of NaOH. Second step is the nanosheets were formed before curving to nanotubes. The high surface energy of the nanosheets resulted in their curl and subsequent formation of the nanotubes. The green sample was given by washing process for Na ions exchanged by proton in the solid solution system. These behaviors can be explained as follows (Vu *et al.*, 2014; Bavykin and Walsh, 2009) dissolution of TiO_2 precursor:



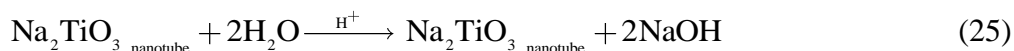
dissolution crystallization of nanosheets:



curving of nanosheets:



washing of nanotubes:



Sodium Hydrogen Titanate ($\text{Na}_y\text{H}_{2-y}\text{Ti}_n\text{O}_{2n+1} \cdot x\text{H}_2\text{O}$) is the product from hydrothermal reaction by TiO_2 particle and NaOH aqueous solution. Hydrogen Titanate or protonate polytitanate ($\text{H}_2\text{Ti}_n\text{O}_{2n+1} \cdot x\text{H}_2\text{O}$) followed by a proton exchange of the sodium hydrogen Titanate washing process (Choi *et al.*, 2010). Many synthetic methods for derive the nanotubes or nanotube arrays that can be grouped into three major synthetic techniques present as Table 2.3.

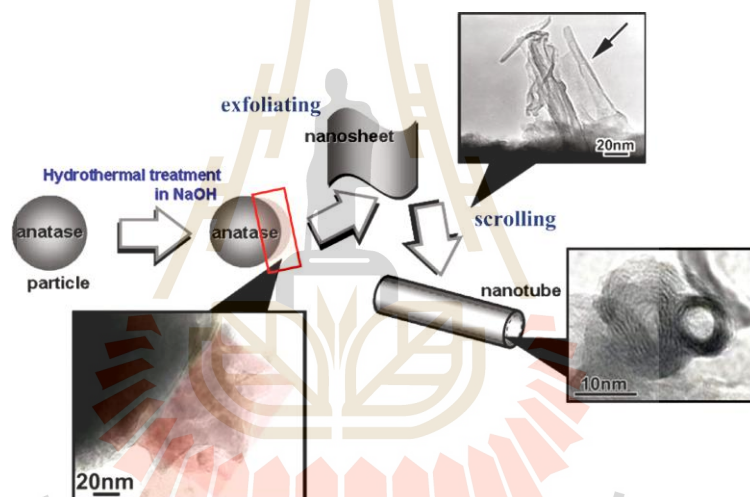


Figure 2.12 Schematic drawing of the exfoliation and scrolling mechanism of nanosheets to nanotubular production (Nakahira *et al.*, 2010).

TNTs based materials have effective in ion-exchange ability because their high charge recombination rate. The band gap found to be 3.3 eV, limit the electron and whole photo generation. Temperature stability of Co-doped TNTs synthesis procedure, undoped and doped were prepare at different temperature. Note that the existence of TNTs phase supports the existence of some Na^+/H^+ replacement in the TNTs structure. Temperature synthesis was compared that structure and morphology of Co-doped TNTs

are maintained homogeneously nanotubular structure. The size of ionic radius effect for increasing oxygen vacancies as a results of ion substitution bring around Co-doping stabilizes with the TNTs in wider synthesis temperature range. This is a significant reduction of the autoclave dwell time thus a cost saving in energy consumption (Ferreira *et al.*, 2013).

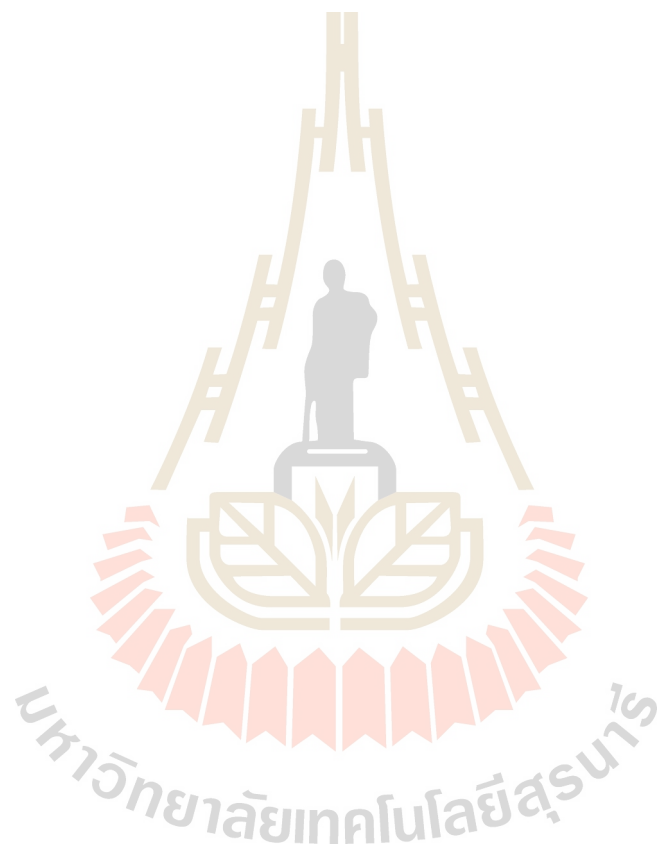


Table 2.3 Comparison of the three preparation methods for fabrication of 1D TiO₂-derived nanomaterial.

Method	Diameter (nm)	Advantages	Disadvantage
Template synthesis	2.5-600	1) Well dimension controlled 2) Wide diameter range	1) Sacrificial template 2) Amorphous 3) Quantity limited
Anodization of Ti foils	20-110	1) Efficient immobilization 2) Ordered array	1) Large diameter and thick wall 2) Fluoride ion needed 3) Low surface area
Alkaline hydrothermal method	10-200	1) Various morphologies 2) Simple and cost effective 3) High specific surface area and aspect ratio 4) Not template needed	1) Poor morphology and dimension controlled 2) Uncontrolled chemical structures

Energy storage application, hydrogen titanate nanotubes have been investigated as lithium intercalation hosts for a remains phase stable after repeated cycling (Li *et al.*, 2006). Three-dimensional pore structure as unique for electron and OH⁻ ions contact

the Co species uniformly distributed on TNTs retain large specific surface area. The enhancement of electrical conductivity was investigated by the EIS technique, Co-functionalized TNTs electrode certain that better electrochemical performance because introduced of Co species (Hou *et al.*, 2011). Layered sodium titanate nanostructure ($\text{Na}_2\text{Ti}_2\text{O}_4(\text{OH})_2$) were use as electrode materials for high energy density supercapacitor under pseudocapacitance storage. Electrochemical evaluation (Figure 2.13(d), highest observed for $\text{Na}_2\text{Ti}_2\text{O}_4(\text{OH})_2$ which predominantly result from the redox process is the reduction which the initial process as



The metal cations C^+ are incorporation of proton/cations and electrons in the $\text{Na}_2\text{Ti}_2\text{O}_4(\text{OH})_2$ lattice. At high scan rate is a reduction reaction which indicating the energy storage under pseudocapacitive. This redox reaction at the thin surface of $\text{Na}_2\text{Ti}_2\text{O}_4(\text{OH})_2$ electrode involving the insertion and extraction of cations could be present as



Charging process show that oxidation state of Ti change from +3 to +4 and reversible reactions occur during discharging. These occurrence pseudocapacitive and electric double layer behavior, results from its layered structure which without in Na free TiO_2 structure relation with XRD results (Aziz *et al.*, 2013) as in Figure 2.11(c).

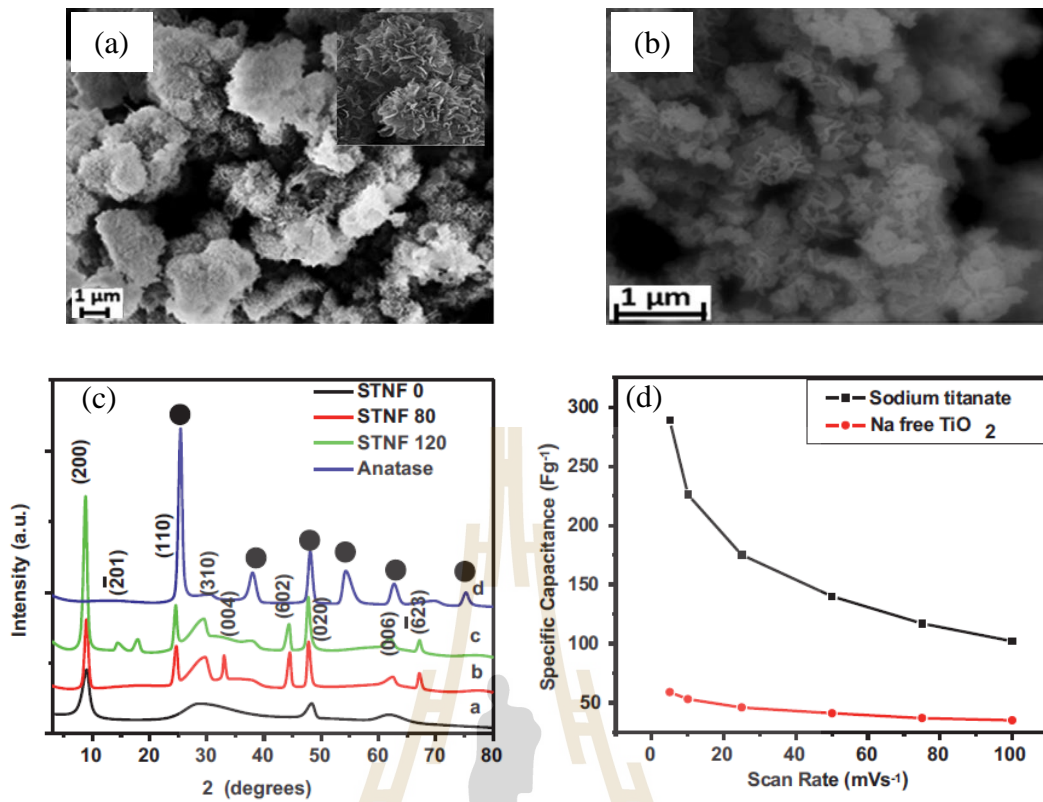


Figure 2.13 The flower like aggregates of (a) sodium titanate nanofiber (STNF120) and (b) Na free TiO₂ (anatase) developed by washing the STNF. (c) The phase formation of STNF as various reaction temperatures and (c) the specific capacitance as various scan rate (Aziz *et al.*, 2013).

Table 2.4 List of difference TiO₂ based electrode materials.

Electrode materials	C _s (F/g)	Electrolyte	Potentials windows (V)	References
TiO ₂ nanorods	8.50	1M Na ₂ SO ₄	0 to 0.8	Ramadoss and Kim (2013)
TiO ₂ nanotubes	19.20	1M NaOH	-0.6 to 0.3	Salari <i>et al.</i> (2012)
TiO ₂ nanofibers	65.80	1M Na ₂ SO ₄	0 to 0.4	He <i>et al.</i> (2016)
10NiO _x /TiO ₂ nanotubes	698.30	1M KOH	0 to 0.6	Cui <i>et al.</i> (2016)
CoS/TNTs nanotubes	362.00	2M KOH	-0.2 to 0.6	Ray <i>et al.</i> (2015)
	427.00	2M KCl	-1.0 to 0	
	374.00	1M Na ₂ SO ₃	-1.0 to 0	
	493.00	1M Na ₂ SO ₄	-1.0 to 0	
Na ₂ Ti ₃ O ₇	300.00	1M KOH	-0.2 to 0.7	Aziz <i>et al.</i> (2013)
TiO ₂ nanoflowers	60.00	1M KOH	-0.1 to 0.6	

Table 2.4 show the electrochemical supercapacitance performance of the different TiO₂ based materials. Morphology of nanotube could be more effective and lower effective in the TiO₂ structured which compared by complex TNTs structured. However, TiO₂ based materials showed high performance for composite with NiO_x and CoS that can be perform in different electrolyte as in Na₂SO₄, NaOH, KOH, Na₂SO₃, and KCL etc. The data from table 2.4 was illustrated by Figure 2.14.

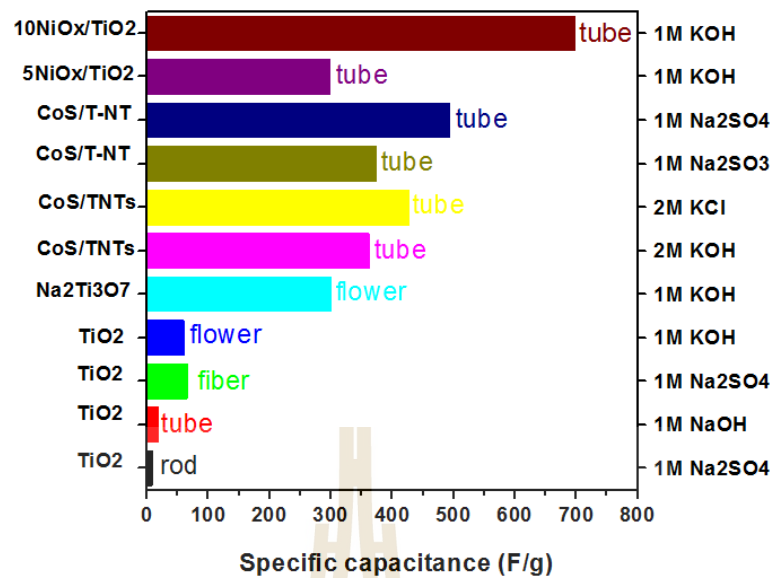


Figure 2.14 The specific capacitance of TiO₂ based electrode materials as a function of electrolytes and their morphology (data adapted from Table 2.4).

The electronic conductivity of MnO₂ are $10^{-6} - 10^{-5}$ S/cm while TiO₂ show $10^{-5} - 10^{-2}$ S/cm (Lu *et al.*, 2013). Zhou *et al.* (2016) report MnO₂ deposited on TiO₂ nanotube arrays has a stabilization effect on the cycling stability because of

(i) The thinnest shell of MnO₂ builds on TiO₂ nanotube walls that showed smallest electrical conduction and ion diffusion resistance in the MnO₂.

(ii) 1D nanotube structure as unblock pathway for reducing the ion diffuse and diffusion time to contact with active materials.

(iii) The conductive TiO₂ core as superhighway in the charge storage and the delivery that minimizes the electron transport resistance in the electrode of MnO₂.

(iv) The TiO₂ scaffold counteracts the strain during ion intercalation into the MnO₂ matrix.

The combination of MnO₂ with TiO₂ nanosheets for improving electrode stability and enhancing the ion/charge transport properties at the electrode and

electrolytic surface of MnO_2 . The combined effect in the facilitated charge transfer to the MnO_2 phase induced by the addition of TiO_2 suggest that can be increased surface area accessibility for electrolyte ion transport derived from 3D tremella-on-sheet structure. However, high addition caused to second growing of MnO_2 active materials which some overlayer active materials enlarge the diffusion path for electron transfer (Zhu *et al.*, 2015).

Hierarchically birnessite type MnO_2 nanoflakes with different titania based nanowires (i.e. $\text{MnO}_2/\text{H}_2\text{Ti}_3\text{O}_7$ and $\text{MnO}_2/\text{TiO}_2$). As in Figure 2.11 for morphology and the specific capacitance which show good electrochemical behavior with $\text{MnO}_2/\text{TiO}_2$ electrode material. This is because the highly porous structure and surface texture of TiO_2 facilitate the ion transfer into porous structure which would lead to substantial redox faradic reactions and surface adsorption of electrolyte cations. Moreover, asymmetric supercapacitor of these electrode by activated graphenes as $\text{MnO}_2/\text{H}_2\text{Ti}_3\text{O}_7//\text{AG}$ and $\text{MnO}_2/\text{TiO}_2//\text{AG}$ are investigate in comparison. The energy density value of $\text{MnO}_2/\text{TiO}_2//\text{AG}$ supercapacitor showed more than twice of $\text{MnO}_2/\text{H}_2\text{Ti}_3\text{O}_7//\text{AG}$ asymmetric supercapacitor (Zhang *et al.*, 2014).

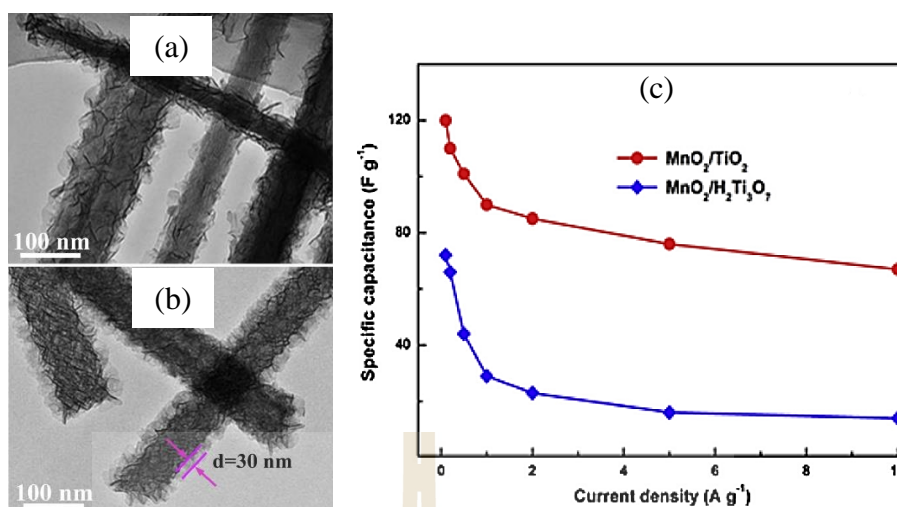


Figure 2.15 (a-b) The TiO₂ covered with a layer of densed MnO₂ ultrathin nanoflakes and (c) the specific capacitance versus current density (Zhang *et al.*, 2014).

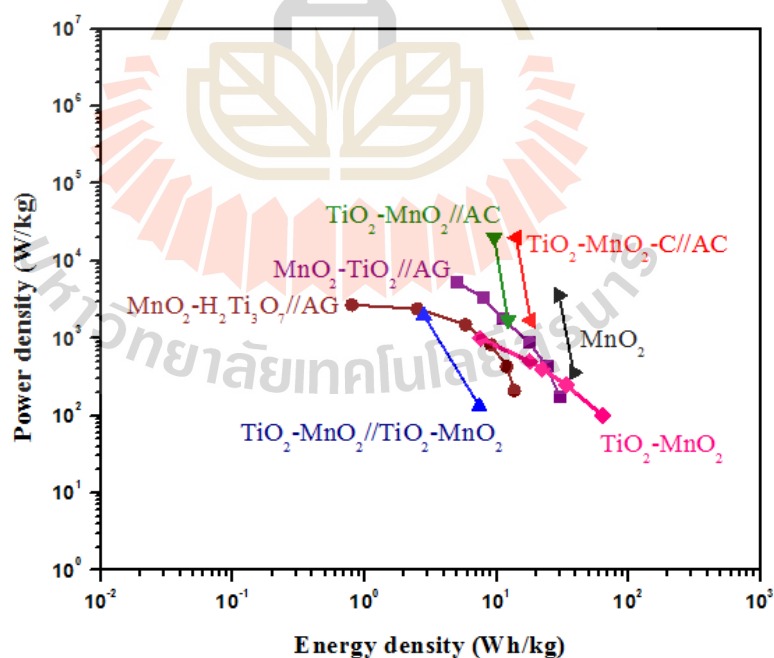
Although Sodium TNTs (Na₂Ti₂O₄(OH)₂) electrode showed higher effective compared with Na free TiO₂ when performed in KOH electrolyte. In the Na₂SO₄ electrolyte MnO₂/H₂Ti₃O₇ has more effective than MnO₂/TiO₂ comparison. However, TiO₂ supported by MnO₂ perform much better in Na₂Ti₃O₇ with the calculated specific capacitance and stability retention. Possibly, Na₂Ti₃O₇ materials is the poor electronic conductivity. And the electrostatic repulsion between Na⁺ in the Na₂Ti₃O₇ network and Na⁺ in the electrolyte which migrates toward the surface or insert into the bulk of MnO₂ (Liu *et al.*, 2017). MnO₂-TNTs as electrode-based materials were reported their specific capacitance and condition test with 3-electrode system show in Table 2.5.

Table 2.5 MnO₂-TiO₂ electrode based-materials the specific capacitance in Na₂SO₄ aqueous electrolyte.

Electrode materials	Cs (F/g)	Current density (A/g)	Reference
Electrodeposition method			
MnO ₂ nanospheres on C paper	120.00	1	Ye <i>et al.</i> (2017)
MnO ₂ nanosheets on C paper	150.00	1	
MnO ₂ nanoflowers on C paper	175.00	1	
MnO ₂ nanorods on C paper	280.00	1	
Hydrothermal method			
MnO ₂ nanospheres (60 °C 12h)	180.00	1	Liu <i>et al.</i> (2012)
MnO ₂ nanoflowers (160 °C 12h)	197.00	1	Zhao <i>et al.</i> (2015)
MnO ₂ (120 °C 16h)	200.00	1	Zhang <i>et al.</i> (2014)
MnO ₂ (200 °C 16h)	106.25	1	
MnO ₂ nanotubes (140 °C 24h)	325.00	1	Huang <i>et al.</i> (2014)
MnO ₂ /MnO ₂ (140 °C 12h)	108.00	5	Shao <i>et al.</i> (2015)
TiO ₂ /MnO ₂ (160 °C 5h)	128.40	1	Luo <i>et al.</i> (2013)
MnO ₂ /TiO ₂ (140 °C 24h)	250.00	1	Zhang <i>et al.</i> (2014)
MnO ₂ /H ₂ Ti ₃ O ₇ (140 °C 24h)	132.00	1	
MnO ₂ /TiO ₂ (140 °C 24h)	286.69	1	Zhu <i>et al.</i> (2015)

Table 2.6 Energy power densities of MnO₂-TiO₂ electrode-based materials.

Electrode materials	Energy density (Wh/kg)	Power density (kW/kg)	Reference
MnO ₂	38.5 to 29.75	0.36 to 3.57	Yu <i>et al.</i> (2009)
TiO ₂ /MnO ₂	63.7 to 7.5	0.10 to 1.00	Xiong <i>et al.</i> (2016)
MnO ₂ /TiO ₂ //AG	29.8 to 4.9	0.18 to 5.40	Zhang <i>et al.</i> (2014)
MnO ₂ /H ₂ Ti ₃ O ₇ //AG	13.6 to 0.8	2.10 to 2.70	
TiO ₂ /MnO ₂ //TiO ₂ /MnO ₂	7.4 to 2.8	0.13 to 1.98	Zhou <i>et al.</i> (2016)
TiO ₂ -MnO ₂ //AC	12.2 to 9.6	1.70 to 20.00	Xiong <i>et al.</i> (2016)
TiO ₂ -MnO ₂ -C//AC	18.1 to 14.1	1.70 to 20.00	

**Figure 2.16** Ragone plots of MnO₂-TiO₂ electrode-based materials (adapted from Table 2.5).

CHAPTER III

RESEARCH METHODOLOGY

3.1 Materials

3.1.1 Titanium dioxide (TiO_2), MW= 79.87 g/mol, 99.00%, Riedel-de Haën

3.1.2 Sodium hydroxide (NaOH), MW = 40 g/mol, 99.00%, Merck kGaA

3.1.3 Potassium Permanganess (KMnO_4), MW= 158.034 g/mol, 99.00%,

UNIVAR

3.1.4 Sodium sulfate (Na_2SO_4). MW= 142.24 g/mol

3.1.5 Potassium chloride (KCl)

3.1.6 Acetylene black

3.1.7 Polyvinylidene difluoride (PVDF)

3.1.8 N-methyl-2 pyrrolidinone (NMP)

3.1.9 Nickle foam

3.2 MnO_2 -TNTs Preparation

3.2.1 Synthesis of TNTs precursor

TiO_2 powders 2 g were dissolved in distilled water 160 mL under stirring continuously. After 1 h. NaOH powder 64 g added into TiO_2 solution and magnetically stirred for 24 h. Homogeneous solution was transferred into a Teflon-lined stainless-steel and hydrothermal reaction operated at 130°C under 150 rpm constant stirrer for

24 h. The precipitated TNTs leached with distilled water by several times until neutral pH then oven dried at 70°C.

3.2.2 Synthesis of MnO₂-TNTs materials

To study the effect of reaction temperature, 25 g of TNTs powder and 40 mL of 0.01M KMnO₄ solution were transferred to the ultra-sonicate for 10 min. Purple solution was transferred into Teflon-lined stainless-steel autoclave and hydrothermal reaction was operated at various temperature as 60, 80, 100, 125, and 150°C for 24h. The MnO₂-TNTs brown precipitated was dried at 70°C in the oven for MnO₂-TNTs powder. The effect of reaction temperatures, samples were labeled as “temperature_MnTNTs” for 60C_MnTNTs, 80C_MnTNTs,..., 150C_MnTNTs.

To study the effect composition ratios between MnO₂ and TNTs, preparation procedure is the same as previously described in figure 3.1. However, the composition ratios between MnO₂ and TNTs were varied are 0.005M:25g, 0.01M:25g, 0.05M:25g of KMnO₄:TNTs. These samples were labeled as “xMnTNTs” where x = 0.005M, 0.01M, and 0.05M.

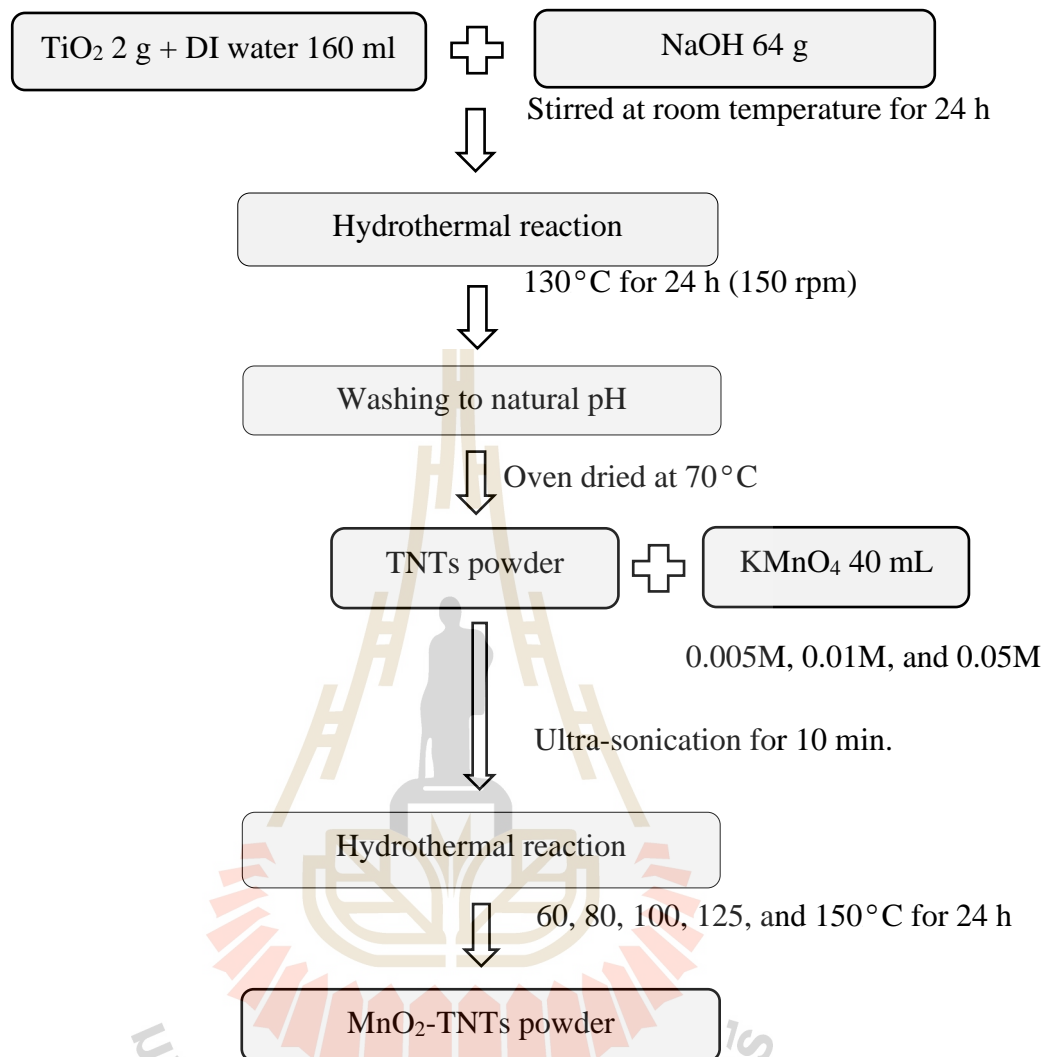


Figure 3.1 Flow chart of MnO_2 -TNTs preparation by hydrothermal method.

3.3 Basic characterization

3.3.1 X-ray Diffraction technique

X-ray diffraction (XRD) is a technique for evaluating the information of phase structure. The existence of certain phase relations between two or more waves are take place.

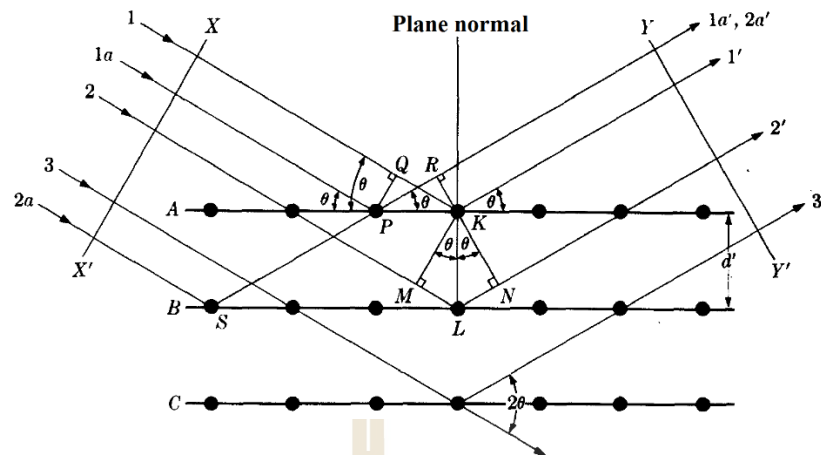


Figure 3.2 Diffraction of x-rays by a crystal (Cullity and Stock, 2001).

When a crystal diffracts x-ray present as in Figure 3.2. The diffraction of x-rays by a crystal which atoms were arranged by parallel set planes A, B, C, D, ... with spaced a distance d' part. The wavelength is the incident beam on crystal for creating angle θ , called the Bragg angle. Where θ was measured by the incident beam and the crystal planes under consideration. Different path and phase were measured in the wavelengths of x-rays. Incident rays 1 and 1a are strike the atoms at in the K and P plane then scatted in all directions. A diffracted beam may be defining as a beam is composed of many scattered rays reinforcing one another. The indirection $1'$ and $1a'$ were scattered by all of atoms in the first plane. This will be true of all the separately planes and it remains to finding the condition for reinforcing the scattered rays at atom in different planes.

Rays 1 and 2 are scattered by atoms K and L, and the difference path of rays is

$$ML - LN = d' \sin \theta + d' \sin \theta \quad (28)$$

This is also the difference path for overlapping rays was scattered by S and P, there is no path difference between rays scattered by S and L or P and K. The scattered rays $1'$

and 2' will be completely in phase if this path difference is equal to a whole number n of wavelength which formulated by W.L. Bragg's is known as Bragg's law

$$n\lambda = 2d' \sin \theta \quad (29)$$

The order of diffraction is n , it may take on any integral value consistent with $\sin \theta$. Value λ and d' were fixed there may be several angles of incident at which diffraction occur. This first order, the scattered rays 1' and 2' would differ in length of path and in phase by one wavelength. Rays 1' and 3' by two wavelengths and rays 1' and 4' by three wavelengths and so on throughout the crystal to form diffracted beam (Cullity and Stock, 2001).

TNTs and MnO₂-TNTs powder were XRD characterized by Bruker D2 PHASER of Bruker AXS GmbH, Germany. XRD instrument useable at the center for scientific and technology equipment. Suranaree University of Technology.

3.3.2 Scanning electron microscopy

Scanning electron microscopy (SEM) is used tool visualize the structure present as image. When the signal collected from the beam specimen interacts with one location to another. The electron beam impinges the specimen, many types of signal are generated that can be displayed as an image. The detector system converts the signals with point by point intensity and produces an image. Secondary electrons (SE) and backscattered electrons (BSE) are most detected as in Figure 3.3. The signals are collected when a positive voltage is applying to the collector screen in front of the detector while a negative voltage on the collector screen. BSE signal is captured because the low SE are repelled by the scintillator/photomultiplier (PMT) are then amplified (Amp) for display on the cathode ray tube (CRT).

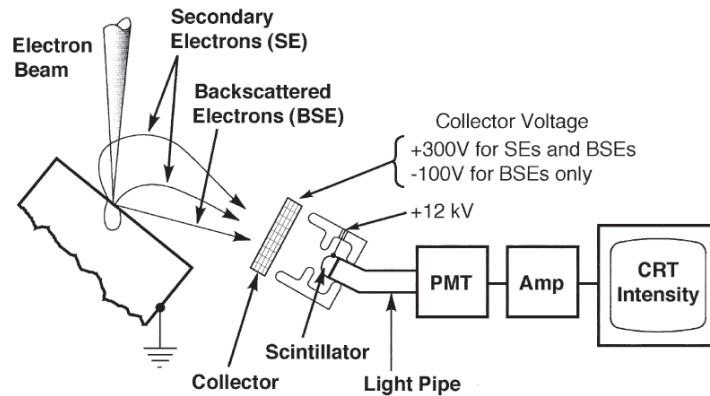


Figure 3.3 Diagram of backscattered and secondary electron collection of these signals by the Everhart–Thornley detector (Goldstein *et al.*, 2003).

Energy dispersive x-ray spectroscopy (EDX) in scanning electron microscopy were used to analysis energy characterization that enable the chemical element of sample. Primary electron transverse a path through sample, electron undergo interaction that generate x-ray without colliding directly with another electron. This produce the continuous distribution of x-ray type that called Bremsstrahlung x-ray radiation. The characteristic of x-ray radiation shows as Figure 3.4. The electron is scattered with little loss of energy and if collide directly with another electron that remove the electron from its orbit led to electronic vacancy, which is filled by an electron from an outer electronic layer and of higher energy. During this transition the electron loses energy by emitting an X-ray. This is characteristic X-ray radiation reveal that energy value of the X-ray emitted during this electronic transition is characteristic for each chemical element, electronic layer, and electronic transition. The energy characteristic is captured by dispersive x-rays detector (de Assumpção Pereira-da-Silva and Ferri, 2017).

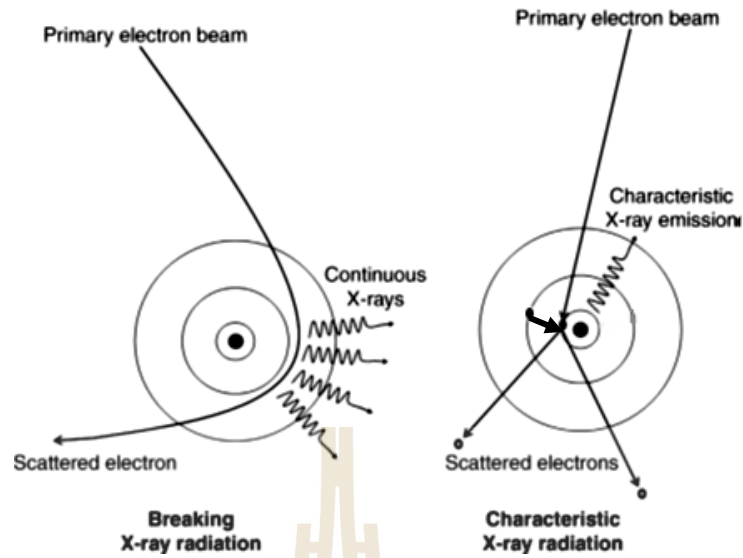


Figure 3.4 The principles in forming Bremsstrahlung and characteristic X-ray radiation (de Assumpção Pereira-da-Silva and Ferri, 2017).

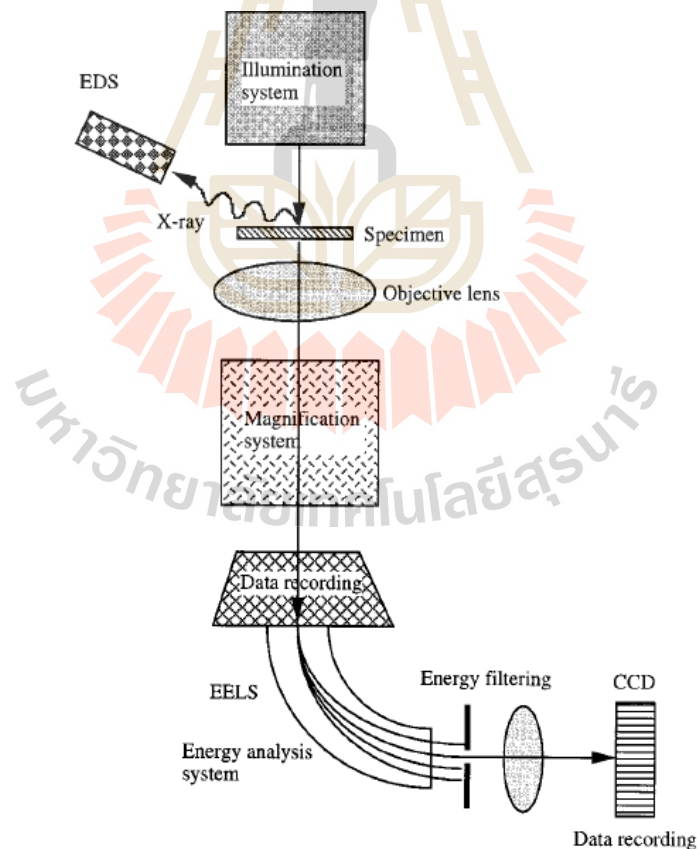


Figure 3.5 The schematic structure of a transmission electron microscope (Wang, 2001)

SEM image and EDX analysis of all the sample are also evaluated by SEM of JEOL JSM 7800F from Japan. SEM instrument is available at the center for scientific and technology equipment. The scientific center of Suranaree University of Technology.

3.3.3 Transmission electron microscopy

Transmission electron microscopy (TEM) was using to perform a real space image on the atom distribution in the nanocrystal and on its surface. As in Figure 3.5 TEM composed of illumination system, a specimen stage, an objective lens system, the magnification, the data recording and the chemical analysis system (Wang, 2001). The specimen stage is a key for carrying out structure analysis, because it can be used to perform in-situ observations of phenomena induced by annealing, electric field or mechanical stress giving the possibility to characterize the physical properties of individual nanostructures. Objective lens is the heart of a TEM for determines the limit of image resolution. Magnification system consists of intermediate lenses and projection lenses. The data recording system tends to be digital with the use of a charge couple device (CCD), allowing quantitative data processing and quantification. Finally, the chemical analysis system is the energy dispersive x-ray spectroscopy (EDS) and electron energy-loss spectroscopy (EELS). EDS and EELS can be used complimentary to quantify the chemical composition of the specimen, EELS can also provide information about the electronic structure of the specimen.

All the sample were investigated by TEM equipped with FEI TECNAI G² 20. The instrument is available at research instrument center. Khon Kaen University.

3.3.4 Fourier Transform Infrared spectroscopy

Infrared absorption also called FTIR or mid-IR absorption. FTIR use in the context of chemical analysis. When the monochromatic light of energy encounter matter and there are reflected, absorbed, or scattered. IR radiation is absorbed by molecules in the sample, transitions between vibrational energy states of the chemical bonds occur. These energy vibrations with respect to chemical bonds which contain the information of function groups and chemical structure of the compounds in the sample (Bouyanfif *et al.*, 2018).

FTIR spectra was recorded by Tensor 27 spectrometer in the attenuated total reflection (ATR) mode. The sample holder was use as background spectra with 64 scans and were taken from 4000 to 400 cm^{-1} with a resolution of 60 cm^{-1} . The FTIR spectra of sample are present to the transmittance correlate with wave number. FTIR Tensor 27 available at the center for scientific and technology equipment. Suranaree University of Technology.

3.3.5 X-ray Photoelectron spectroscopy

X-ray Photoelectron spectroscopy (XPS). XPS technique was analyzed the surface chemical state. The surface chemistry of materials information and valuable quantity can be obtained by scanning x-ray beam across the sample surface. The core electrons are emitted from a sample and adsorb incident photons from an X-ray source. The kinetic energy of the emitted core electrons was determined by conservation of energy. The photoelectron ejects are kinetic energy that measured relatively with the energy required to just remove the electron concerned from initial to fermi level of solid (Zhi *et al.*, 2013; Aziz and Ismail, 2017). Work function of solid are involve as correlation to equation (30)

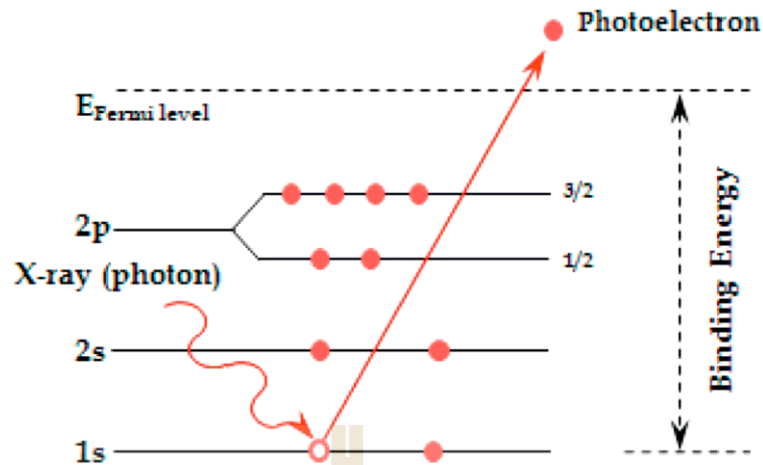


Figure 3.6 Diagram of photo electric effect (Engelhard *et al.*, 2017).

$$E_k = hv - BE - \phi \quad (30)$$

where E_k is the kinetic energy, h is the Planck's constant, v is the frequency, BE is binding energy and ϕ is the work function of solid. The peak of photoelectrons detected versus binding energy were plot in resulting.

All sample was characterized by XPS at beamline 5.3, available at the synchrotron light research institute (SLRI) public organization.

3.3.6 Brunauer-Emmett-Teller method

Brunauer-Emmett-Teller method also know BET. BET technique uses for determining nitrogen adsorption at surface area of porous materials. In the linear form BET equation as

$$\frac{p}{n^a(p_0 - p)} = \frac{1}{n_m^a C} + \frac{(C-1)p}{n_m^a C p_0} \quad (31)$$

where n_a the amount adsorbed at the relative pressure p/p_0 , n_m^a is the monolayer capacity, and C is the BET constant. BET method use calculates the total and specific surface area as follows equation

$$A_s(\text{BET}) = n_m^a L a_m \quad (32)$$

$$a_s(\text{BET}) = \frac{A_s(\text{BET})}{m} \quad (33)$$

where $A_s(\text{BET})$ and $a_s(\text{BET})$ are the specific surface areas and total surface area. L , a_m , and m are the Avogadro constant, molecular cross section area, and molecular weight adsorbent, respectively.

The total pore volume (V_T) derived the amount of vapor adsorbed at a relative pressure. This close to unity that assume the pores filled with condensed adsorptive in the normal liquid state. The pore shape structure is generally assumed to be either cylindrical or slit shape. The average pore size or pore width (r_p) can be obtained from the following

$$V_T = \frac{p_0 V_{\text{ads}} V_m}{RT} \quad (34)$$

$$r_p = \frac{2V_T}{a_s} \quad (35)$$

where V_{ads} is adsorbent of gas volume, V_m is the molar volume of liquid adsorbate, R is gas constant and T is ambient temperature, respectively. The pore size distribution was classified into three class with pore diameter illustrated in Table 3.1.

Table 3.1 IUPAC classification of pores.

Classification	Pore diameter (nm)
Micropore	Up to 2
Mesopore	2 to 50
Macropore	50 or more

Physisorption isotherm grouped as in figure 3.7. Type I is given by microporous solids relatively with small external surfaces. Where the limiting uptake is governed by the accessible micropore volume rather than by the internal surface area. Type II Isotherm is the normal form of isotherm obtained by a non-porous or microporous adsorbent which represent unrestricted monolayer-multilayer adsorption. Point B in the beginning of the almost linear middle section indicate the stage at monolayer coverage is complete and multilayer adsorption. Type III isotherm is not common and there are number of systems which give isotherms with gradual curvature and an indistinct point B such as adsorbate-adsorbate interactions play an important role. Type IV isotherm are its hysteresis loop which associated with capillary condensation taking place in mesopores. Initial part of the type IV isotherm is attributed to monolayer-multilayer adsorption since it follows the same path as the corresponding part of a type II isotherm obtained with the given adsorptive on the same surface area of the adsorbent in a non-porous form. Type V isotherm is uncommon which relate to the type III isotherm in that the adsorbent-adsorbate interaction is weak and obtained with certain porous adsorbents. Type VI isotherm are sharpness of the steps depends on the system and the temperature, represents stepwise multilayer adsorption on a uniform non-porous surface. The step high show represents the monolayer capacity for each adsorbed layer. Hysteresis loops may exhibit a wide variety of shapes, two extreme type show as H_1 and H_4 while types H_2 and H_3 may be regarded as intermediate between these two extremes. A feature common to many hysteresis loops is that the steep region of the desorption branch leading to the lower closure point occur at the relative pressure which is almost independent of the nature of the porous adsorbent but depend on the nature of the adsorptive (Sing, 1985).

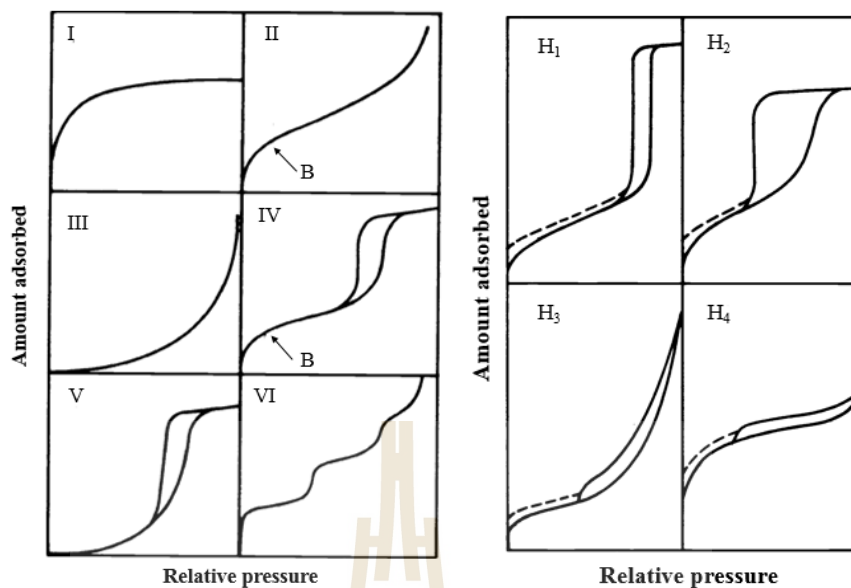


Figure 3.7 Type of physisorption of isotherm and hysteresis loop (Sing, 1985).

The surface adsorption of MnO_2 -TNTs samples was characterized by BELSORP mini II. At The center for scientific and technology equipment. Suranaree University of Technology.

3.4 Electrochemical properties measurement

3.4.1 MnO_2 -TNTs electrode fabrication

MnO_2 -TNTs powders were mixed acetylene black and polyvinylidene difluoride (PVDF) in the weight ratio of 70:20:10. Active mass of working electrode is 70% of weight. Mixed powder was dispersed by shaking in NMP for 1 h into slurry formed, coat on foam nickel as current collector. This fabricated electrode or working electrode was dried at 70°C in the oven and pressed with 1 MPa for 1 min before measurement process. 3-electrode system consist of our working electrode (WE), Pt plate and saturated Ag/AgCl electrode used as counter (CE) and reference electrodes (RE), respectively. This study Na_2SO_4 solution use as natural electrolyte. Figure 3.8

shows Potentiostat-Galvanostat Autolab Methrom (PGSTAT302N) of 3-electrode system were performed by NOVA 1.11 software.

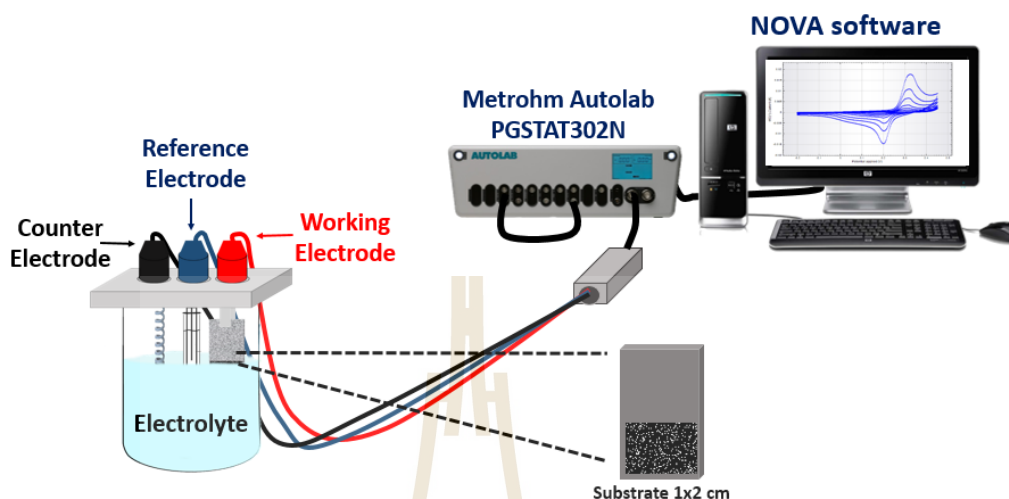


Figure 3.8 Electrochemical measurement setup at Advance Materials Physics (AMP) Laboratory.

3.4.2 Electrochemical measurement technique

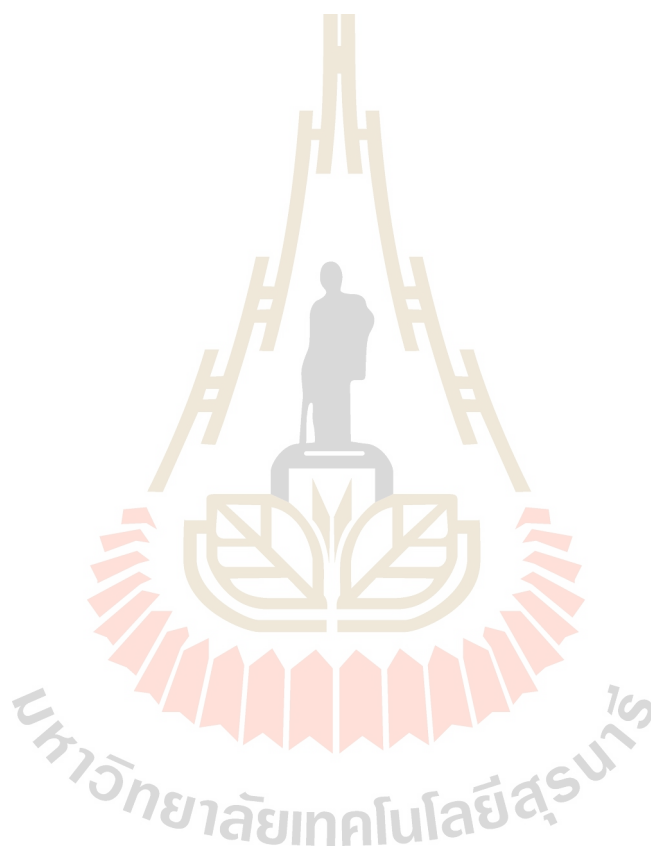
Three-electrode system are made up by RE, CE, and WE. RE has been stable over the reference level during potential measurement. The CE was collected all current flowing via WE. The electrochemical properties of our WE will be examined by CV, GCD, and EIS technique.

CV technique was measured within potential windows range 0 to 1V. Potential windows was scanned by different scan rates of 2, 5, 10, 20, 50, 100 and 200 mV/s. The current response obtained was normalized by active mass of each working electrode.

On the same potential windows, G-CD technique was measured with voltage against time. The current was applying at different current density of 0.5, 1, 2, 3, and 5 A/g. Furthermore, this technique will be cycling test with 1000 cycles for studying their

stability of electrode at current density of 5 A/g. The specific capacitance, energy and power densities were evaluated from discharge time with G-CD technique.

EIS technique was testing over the frequency range from 1 kHz to 0.1 Hz at 0.1 V disturbance. This testing on galvanostat mode and the equivalent circuits was fitted by using NOVA 1.11 software.



CHAPTER IV

RESULTS AND DISCUSSION

4.1 Synthesis and characterization of TNTs precursor

The anatase TiO₂ and NaOH solution are raw materials for synthesis TNTs samples with hydrothermal process at 130°C for 24 h. Stirring process increased the contact ability between TiO₂ and NaOH as declining the transforming time to nanotubes (Vu *et al.*, 2014). After hydrothermal method, TNTs suspension washed with deionized water neutralized until a pH 7 and dry in oven for white TNTs powder. 2 g of anatase TiO₂ were disperse in 180 ml of 10M NaOH (10 g/mol) can produce TNTs of 2 g powder quantities. The alkaline hydrothermal treatment was employed to synthesized large TNTs product. The nanotube morphology was investigated by SEM show different length and average diameter of 71.20 ± 1.60 nm. TNTs is made up of Titanium (Ti), Oxygen (O) and Sodium (Na) elements which confirmed by EDX analysis. The TNTs phase was obtained by XRD technique as pattern in Figure 4.3. The diffractogram was recorded in a range of 2θ from 5-70° (0.02 min⁻¹) at room temperature. XRD pattern shows peak center and plan indexing of $2\theta \sim 9.4^\circ$ (200), 24.5° (110), 28.4° (310), 48.6° (220) and 61.9° (200). Diffraction pattern indicated with titanate nanotubes typical of hydrogen titanium oxide hydrate (H₂Ti₂O₅·H₂O) (JCPDs No. 47-0124).

The most intense peak about 9.4° was attributed interlayer distance of TNTs neighboring walls (Yin and Zhao, 2008). It is clear that all diffraction peaks are indexed to layered titanate (Zhang *et al.*, 2008). The peak at 24.5° can be associated with the presence of hydrogen trititanate which reveal that Na^+/H^+ exchange in the TNTs interlayer region has occurred to some extent after the sample washing process (Ferreira *et al.*, 2013) and a common of TiO_6 building block reflection at 48.6° (Yoshida *et al.*, 2009). However, XRD peak was broadened because of the nanometer size and the bending of some atom planes of the tube (Chen *et al.*, 2002) (Chen *et al.*, 2002). TEM image given rise to multiple wall nanostructure of interior nanotubes. The crystalline structure from selected area electron diffraction (SAED) pattern were indexed to (220) and (110) plan that corresponding with XRD results.



Figure 4.1 (a) TNTs aqueous solutions after washing process and (b) white solid prepared TNTs powder.



Figure 4.2 (a) SEM image of TNTs powder, (b) distribution of diameter about 71 nm and (c) EDX analysis of Ti, O and Na elements.

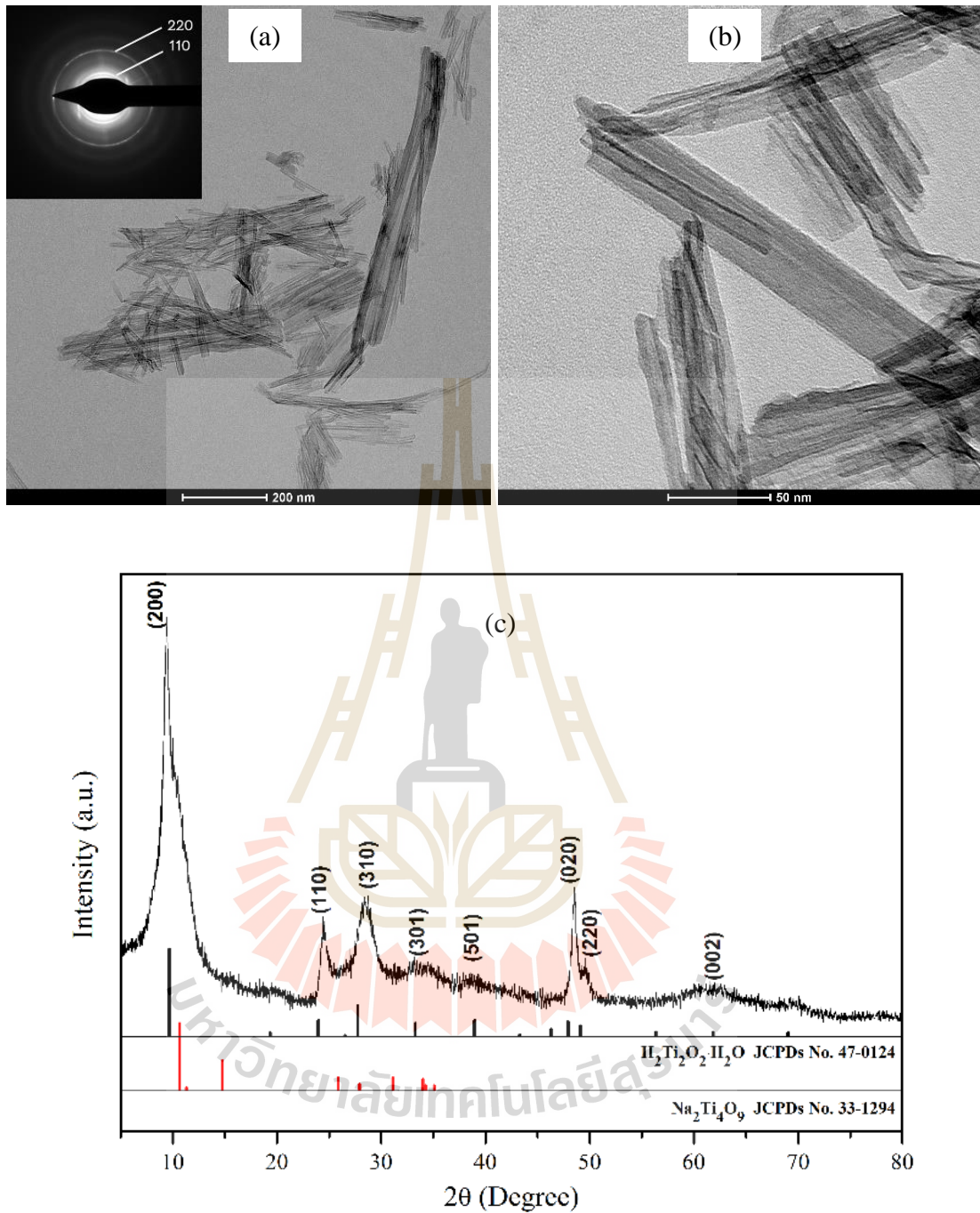


Figure 4.3 (a-b) Tubular characteristics and (c) phase of TNTs was synthesis by hydrothermal method at 130°C for 24h (inset (a) is a SAED pattern).

4.2 Synthesis and characterization of MnO₂-TNTs samples

4.2.1 MnO₂-TNTs materials

The TNTs powder are to be dissolved in 0.01M KMnO₄ solution for studying the influence of the reaction temperature on their properties. MnO₂-TNTs solutions were transferred into Teflon-lined stainless steel. Hydrothermal reaction was done as various temperature of 60, 80, 100, 125, and 150 °C. Firstly observe that the brown solution after TNTs was treated with KMnO₄ solution media at 60 °C whereas another shows the precipitation with increasing of temperature.

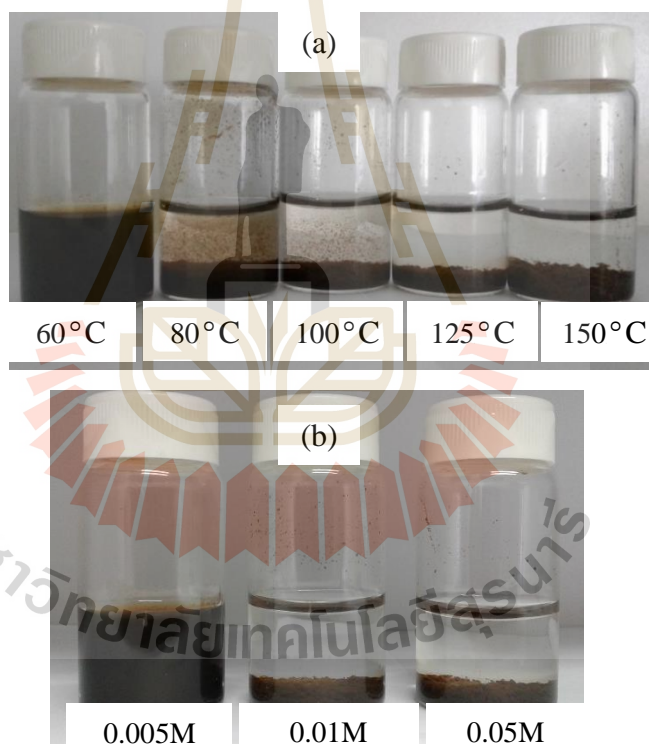


Figure 4.4 The MnO₂-TNTs aqueous form after hydrothermal treatment as (a) various temperature and (b) MnO₂ compositions.

Effect of composition ratios are also studied by different concentrate KMnO₄ for 0.005M, 0.01M, and 0.05M for control of MnO₂ content and hydrothermal reaction

were heated at 80 °C for 24h. These sample labeled by xMnTNTs where molarity $x = 0.005\text{M}$, 0.01M , and 0.05M . In figure 4.4, after hydrothermal treatment, observed that low MnO_2 content, the MnO_2 -TNTs aqueous have been a brown solution whereas precipitation with increasing of MnO_2 content.

4.2.2 XRD characterization of MnO_2 -TNTs materials

TNTs as precursor which was dispersed in KMnO_4 media and transfer to second step hydrothermal method for preparing MnO_2 -TNTs samples. Thermal stability, weak remarkable of $2\theta \sim 9.4^\circ$ intensity peak was observed after second hydrothermal treatment meanwhile other were maintained. The formation of TNTs, Na^+ ions which could play a role in peeling surface into sheet and rolled them to form a tubular shape. XRD show low crystalline characteristics with relatively large specific surface area.

Interest studied the TNTs was hydrothermal treatment with DI water for 12h present tubular characteristics which in agreement with the originated TNTs. Some provide a formation rice-shaped titanate nanoparticle with increase treatment time to 48h then uniformly small size of rice shaped at 72h treatment. Case studied of TNTs was treated by hydrothermal method with 10M NaOH solution and DI water suggest that the aqueous solution would not provide any internal change of the prepared TNTs (Charinpanitkul *et al.* (2011)). The thermal stability of TNTs powder obtained from the thermogravimetric curves. The temperature ranges from 35 up to 800 °C measured on the mass change of sample. Significant weight loss occurring at lower temperatures due to the dehydration of physisorbed water take place (Umek *et al.*, 2007).

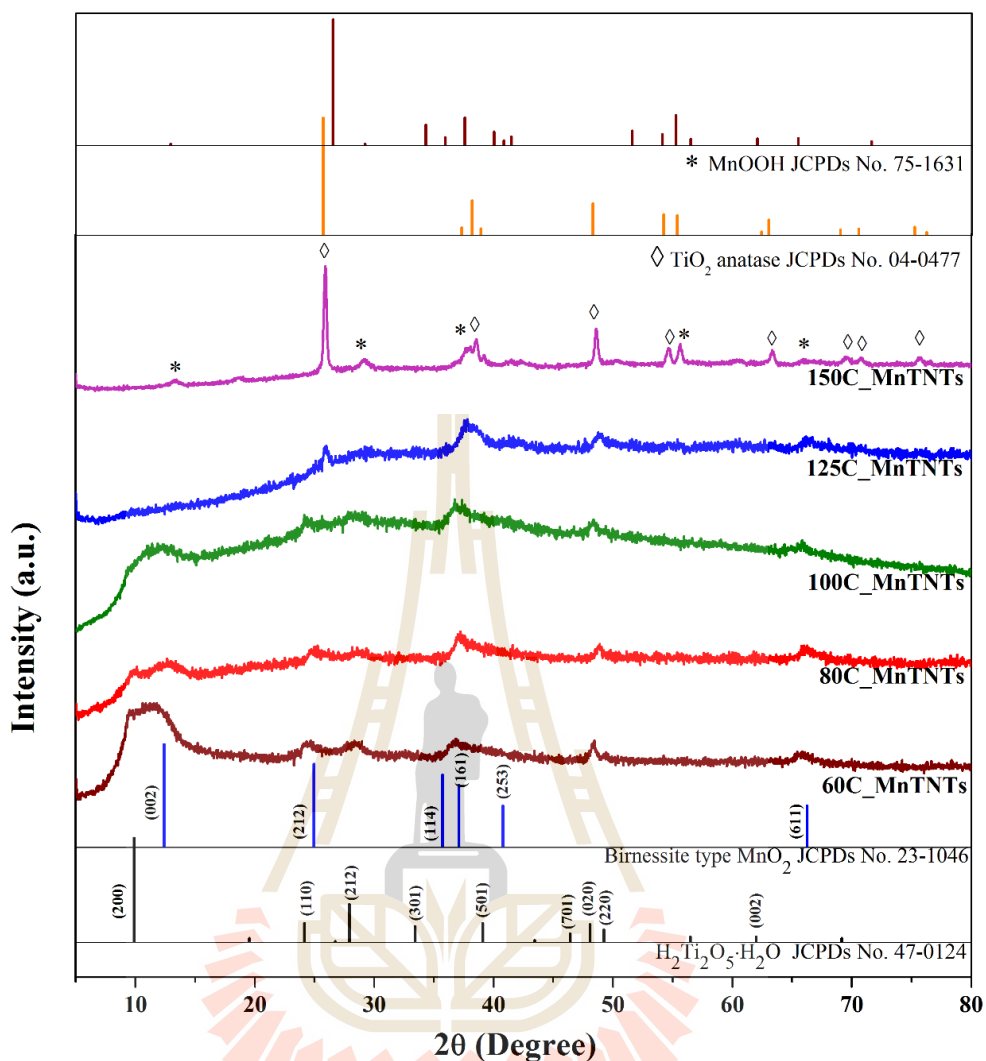


Figure 4.5 XRD pattern of $x\text{MnO}_2\text{-TNTs}$ ($x = 0.01\text{M}$) with different hydrothermal temperature for 24h. The pattern corresponding to $\text{H}_2\text{Ti}_2\text{O}_5\cdot\text{H}_2\text{O}$ and MnO_2 composition phase that transform to TiO_2 anatase and MnOOH phase.

XRD diffractogram shows abroad peak after TNTs was decorated by MnO_2 . This owing to the amorphous of Birnessite-type MnO_2 structure ($\delta\text{-MnO}_2$). Figure 4.5 and 4.6 shows the Birnessite-type MnO_2 characteristic peak located at $2\theta \sim 12.52^\circ$, 24.32° , 36.68° , 48.36° , and 65.79° . This identified peak to (002), (212), (144), (161), (253), and (611) planes of $\delta\text{-MnO}_2$ phase (JCPDs No. 023-1046). $2\theta \sim 12.52^\circ$ relate to

lattice spacing of the layered structure of δ -MnO₂. At low temperature synthesized, XRD results of 60 and 80 °C show clearly seen separation phase between TNTs and MnO₂. At 100 °C has combination phase and there are phases transition above 125 °C. Effect of reaction temperature does show significant change phase of TNTs transformed to anatase TiO₂, most intense peak at 25 ° (101) of anatase TiO₂ was observed (Yılmaz *et al.*, 2013) while δ -MnO₂ is manganese oxide hydroxide (MnOOH).

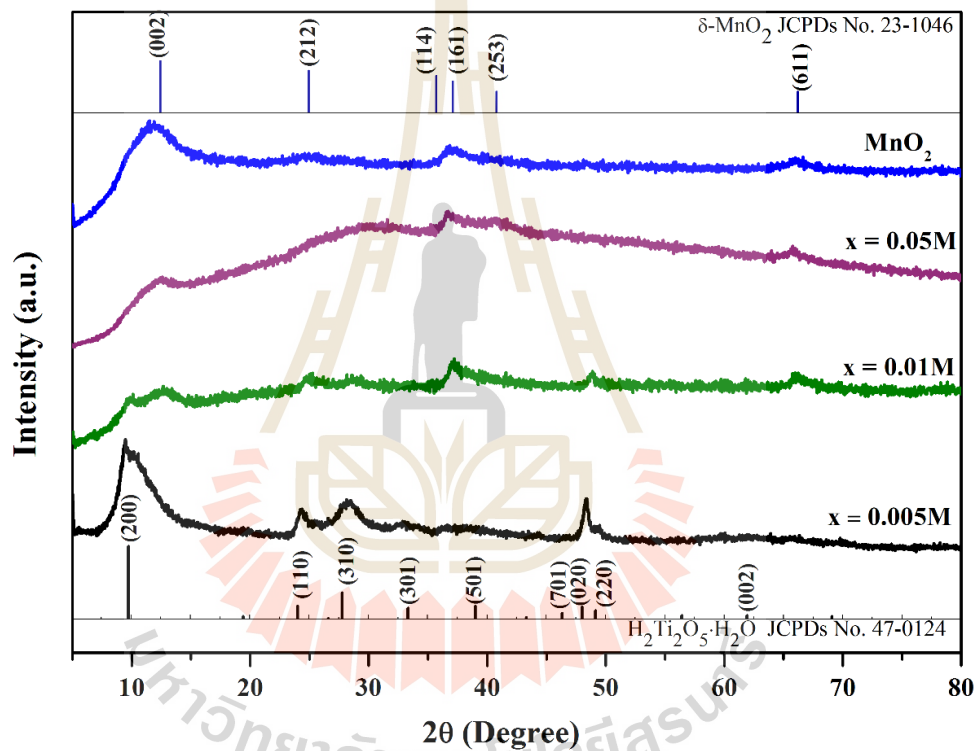


Figure 4.6 XRD patterns of x MnO₂-TNTs powder was synthesized at 80 °C for 24h with a content of MnO₂.

The phase composition studied on XRD analyze, 0.005M of KMnO₄ leading to low active of MnO₂ formation above that will be high MnO₂ formation and hierarchically TNTs. 0.05M shows δ -MnO₂ phase while lower than there is associate phase between MnO₂ and TNTs phase. These relation with the characteristic of MnO₂-

TNTs aqueous after hydrothermal. The reaction and phase combining were completely. However, the broad peak features showed the mixture of amorphous and nanocrystalline nature of the sample.

4.2.3 SEM and TEM characterization of MnO₂-TNTs materials

The low magnification SEM image reveals that the hierarchical nanostructure MnO₂-TNTs samples have been largely agglomeration. The higher magnification image further indicates that MnO₂ nanoflakes growth form on TNTs nanotube and observation MnO₂ are in the space between the nanotubes. The effect of hierarchical nanostructured at different hydrothermal temperature are explain in below follow by step of reaction temperature.

The materials prepared at low temperature treatment (60°C for 24 h) there have been MnO₂ distribute on TNTs nanotubes and low among in between the space, after hydrothermal treatment as in Figure 4.4(a) reveal that the brown solution which may be loss amount materials in washing process. XRD results associate with clearly phase between MnO₂ and TNTs. Figure 4.9(a) present as TEM image of 60C_xMnTNTs (x = 0.01M) which present to MnO₂ thin layer on tube and the tubular show multiwall. At 80-100°C for 24 h, MnO₂ are distribute into TNTs substrate and the space between the nanotubes, this show brown precipitated in solution after hydrothermal treatment process. XRD results starting to composition phase as any peak are overlap until completely with 100°C reaction temperature treatment. The number of MnO₂ are in the space between the nanotubes could be confirming to complete of MnO₂ phase formation. TEM image observed that dense of MnO₂ growth on TNTs tubular this confirm completely of hierarchically of MnO₂-TNTs.

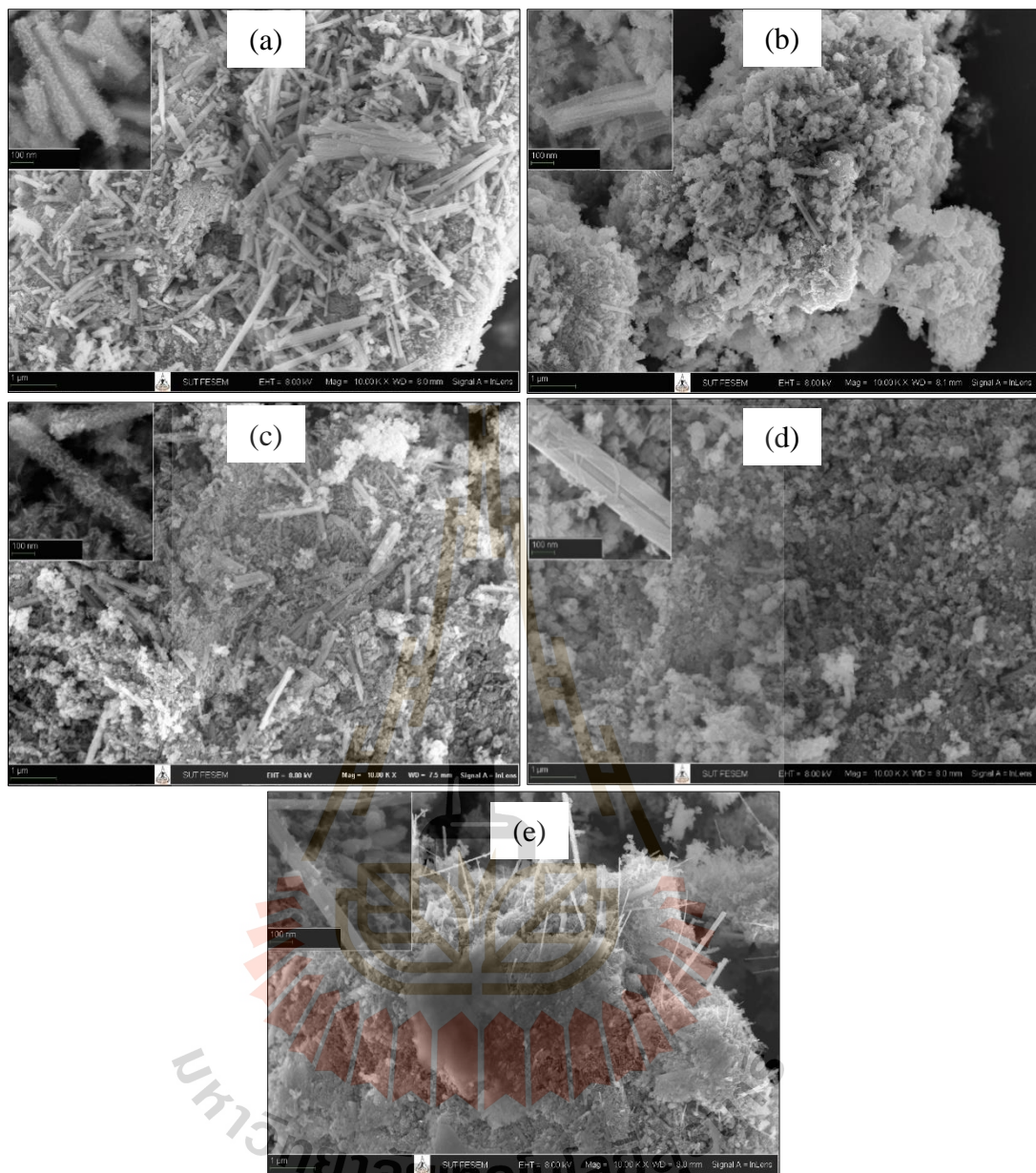


Figure 4.7 SEM image for MnO_2 distribute on TNTs which $x\text{MnO}_2\text{-TNTs}$ ($x=0.01\text{M}$) sample were synthesized at (a) 60°C , (b) 80°C , 100°C , (c) 80°C and (d) 150°C for 24h.

Higher reaction hydrothermal treatment ($125\text{-}150^\circ\text{C}$ for 24 h) upon morphology of $\text{MnO}_2\text{-TNTs}$ changes. The thin of MnO_2 flake are decrease as nanotubular morphology of TNTs which without growth on of MnO_2 on TNTs. Phase

formation were transformed, main phase of $2\theta \sim 12$ for MnO_2 and $2\theta \sim 9$ for TNTs are absence at 125°C and new phase are occurrence after 150°C . TEM image present that characteristic of MnO_2 changes and decrease of MnO_2 decoration are observe.

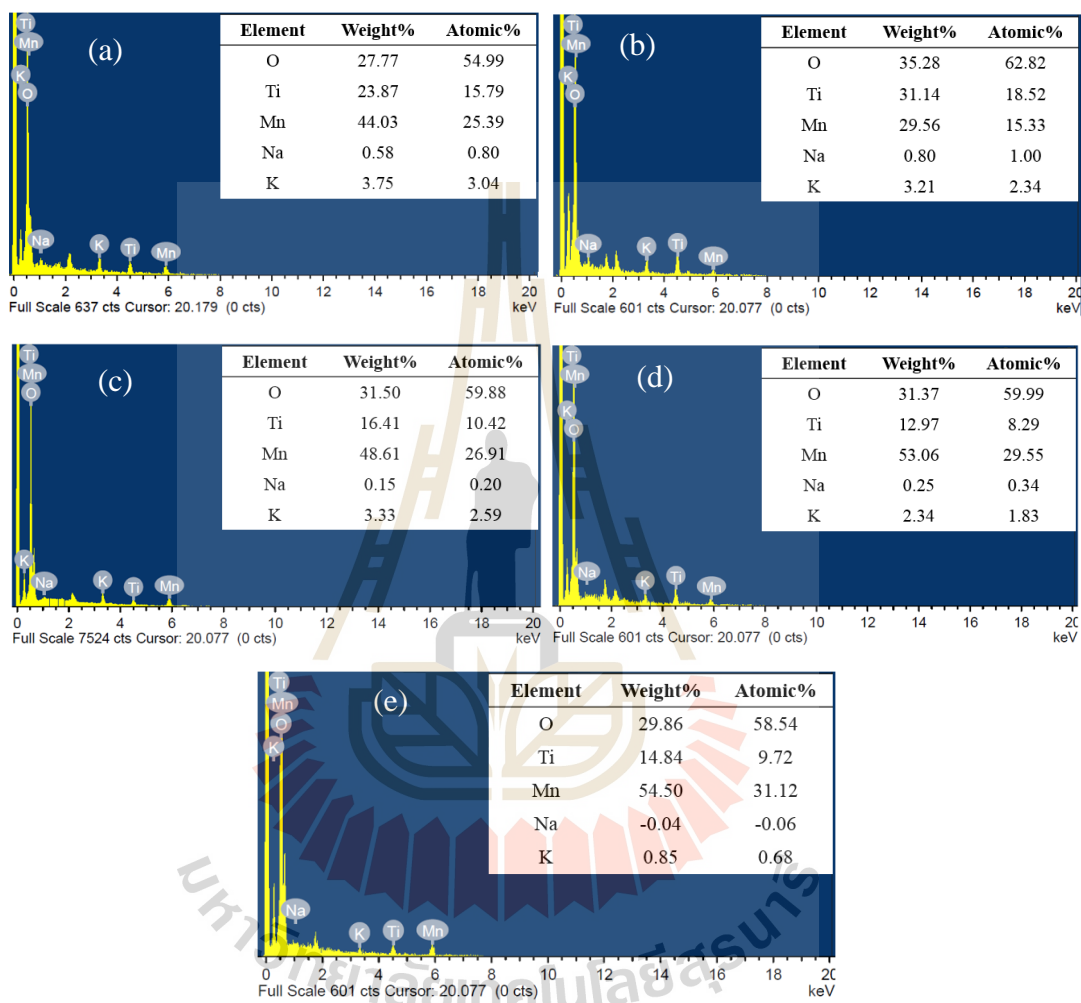


Figure 4.8 EDX analysis of $x\text{MnO}_2\text{-TNTs}$ (where $x = 0.01\text{M}$) sample were synthesized at (a) 60°C , (b) 80°C , 100°C , (c) 125°C and (d) 150°C for 24h.

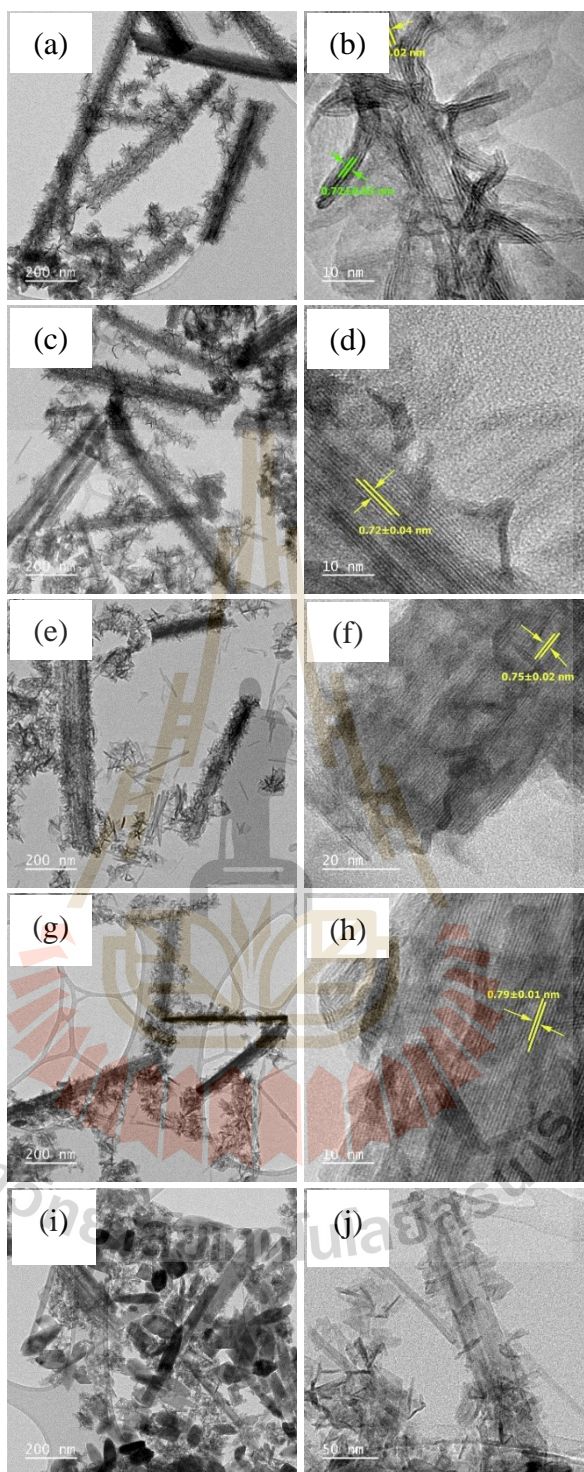


Figure 4.9 TEM image of $x\text{MnO}_2\text{-TNTs}$ ($x = 0.01\text{M}$) were synthesized at (a-b) 60°C , (c-d) 80°C , (e-f) 100°C , (g-h) 80°C and (i-j) 150°C for 24 h. And the high magnification of TEM images (b, d, f, h, and j).

Because the effect of reaction temperature as the limit of hierarchical nanostructure MnO_2 -TNTs. EDX analysis for confirm of Ti, Mn, O, K and small Na elements. To show that TNTs aqueous was washed by DI for ion-exchange. As same as composition ratios between MnO_2 and TNTs materials which prepared by used in 0.01M of KMnO_4 for MnO_2 formation. The weight percentage (wt %) and atomic percentage (at %) ratio reveal that Mn higher number in MnO_2 -TNTs. These EDX results were detected on the nanotube area which MnO_2 distribution.

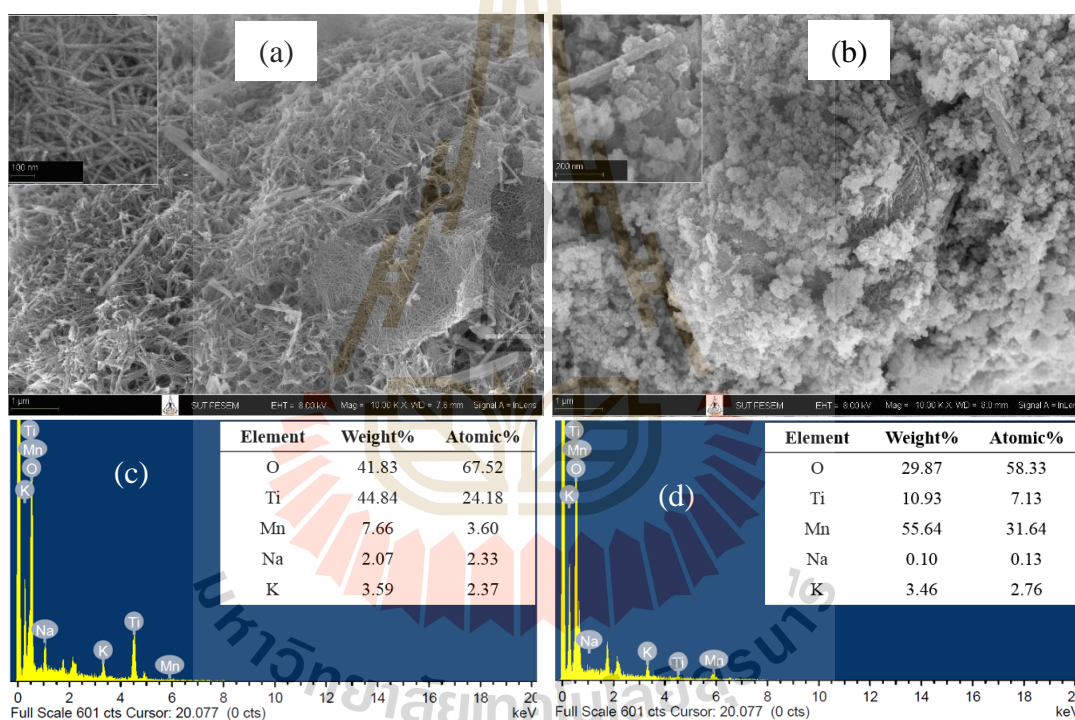


Figure 4.10 SEM image and EDX analysis of $x\text{MnO}_2$ -TNTs synthesized at 80°C for 24h where (a, c) $x = 0.005\text{M}$ and (b, d) $x = 0.05\text{M}$.

Figure 4.10(a, b) and Figure 4.7(b) despite the SEM image for composition ratio effect in comparison. The number of MnO_2 was increase with x in $x\text{MnO}_2$ -TNTs increasing when $x = 0.005\text{M}$, 0.01M , and 0.05M , respectively. As in EDX results confirms the high content of Mn element. Low and high magnification TEM image are

show in Figure 4.11 clearly show the basic morphology the cover of MnO_2 on TNTs. The surface of TNTs is homogeneously decorated with a layer of dense MnO_2 ultrathin nanoflakes. The interconnected MnO_2 nanosheets create a highly porous surface morphology.

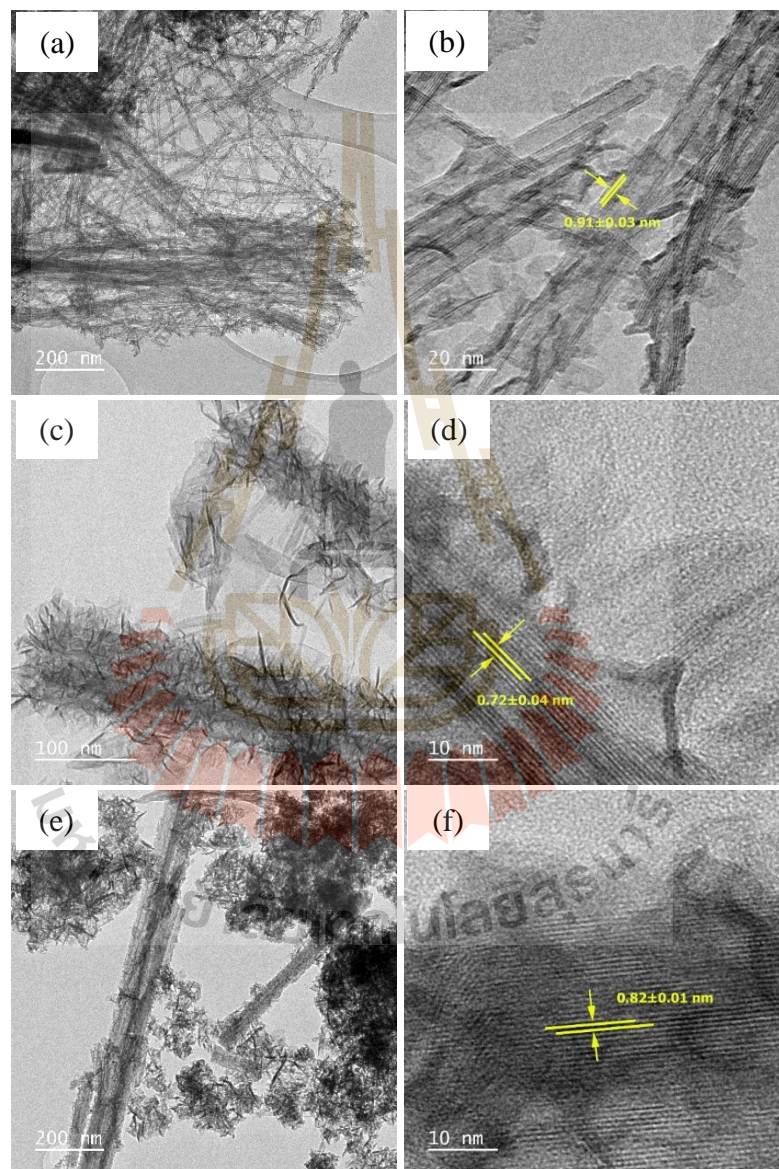


Figure 4.11 TEM image of $x\text{MnO}_2$ -TNTs where (a) $x = 0.005\text{M}$ and (c) $x = 0.05\text{M}$, and (b and d) the high magnification.

4.2.4 FTIR and XPS characterization of MnO₂-TNTs materials

The characteristic vibration of MnO₂-TNTs materials explains by the infrared spectrum. The normally hydroxyl group and interlayer water on the solid surface and water blending mode including hydroxyl group on the surface of TNTs. Vibration of 1400 cm⁻¹ is Mn-OH bending whereas 1100 cm⁻¹ is due to formation of Ti-O groups during alkaline synthesis. Deformation of a hydrogen bond on -OH group present at 919 cm⁻¹. In the range of 600-400 cm⁻¹ are the characteristic band of birnessite type of Mn-O vibration mode. The results show that 517 cm⁻¹ is Mn-O-Mn asymmetric stretching vibration (Misnon *et al.*, 2014). 150C_xMnO₂-TNTs not present IR band at shoulder 2900 cm⁻¹, this peak indicating the interlamellar water was removed and the Ti-O bonds were modified (Shirpour *et al.*, 2013). This confirmed that the phase and structure of MnO₂-TNTs are transform by temperatures dependence. The band at 680 cm⁻¹ attributed to the vibration of bridging oxygen atoms coordinated with Na ions clusters, which were greatly weakened for increasing of MnO₂ contents in MnO₂-TNTs materials (Hu *et al.*, 2009). 478, 652, 910 cm⁻¹ are the occurrence of the TiO₆ octahedra which close to the Mn-O stretching vibrations mode of the octahedral layer. The observation of O-H vibrations in FTIR spectrum suggests the presence of absorbed water molecules within MnO₂-TNTs structure. The hydrous properties of material could enhance the cations diffusion thereby increasing the specific capacitance (Ali *et al.*, 2014). In addition, the band of IR spectrum and explanation are present as Table 4.1 which from these references.

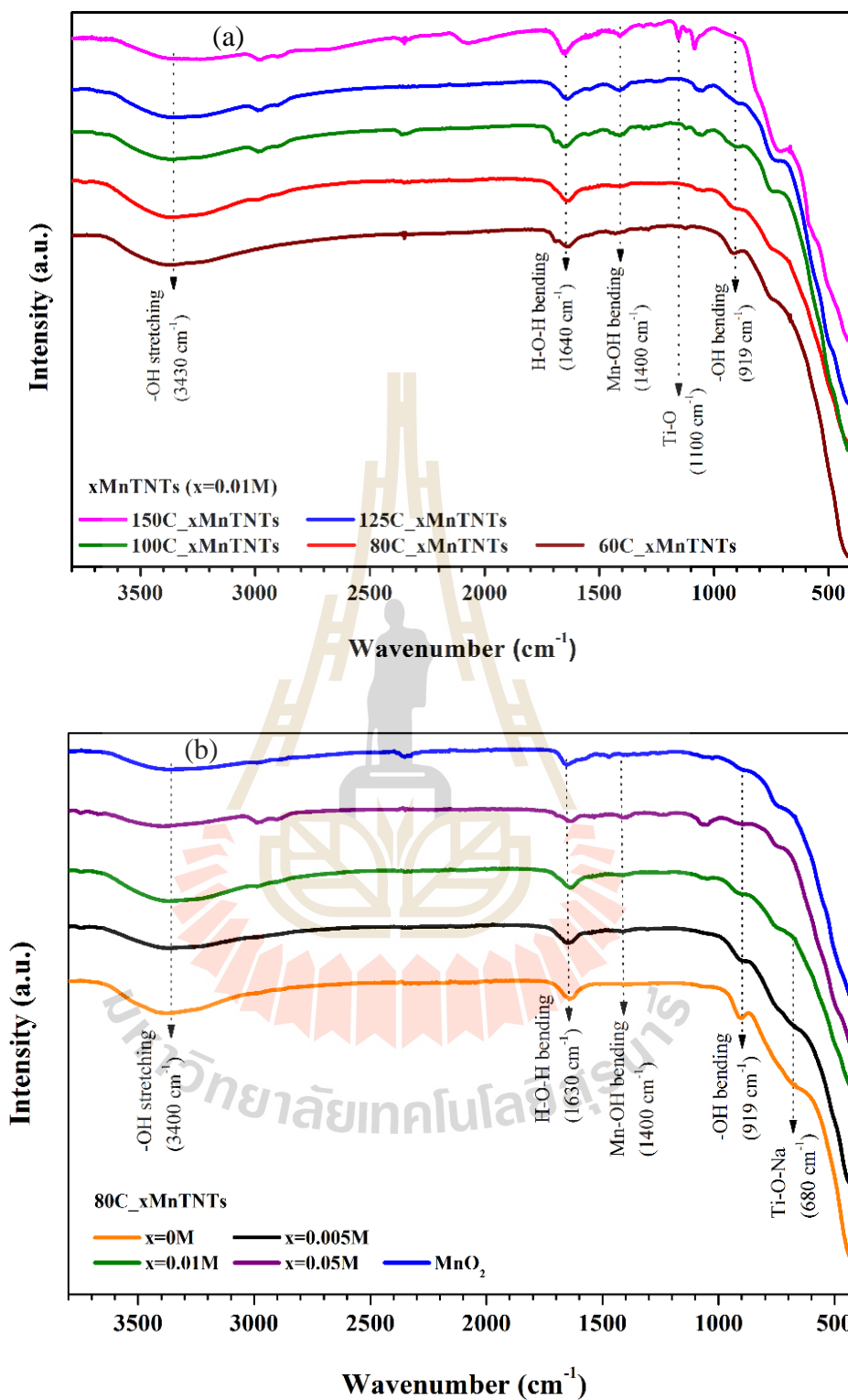


Figure 4.12 FTIR spectra of (a) $x\text{MnO}_2\text{-TNTs}$ ($x = 0.01\text{M}$) with different hydrothermal temperatures and (b) composition ratios effect.

Table 4.1 List of absorption bands for chemical bonding are found in the FTIR spectra.

Band (cm ⁻¹)	Assignment
3700-3000	Hydroxyl group and interlayer water on the solid surface.
3430 and 1630	A dehydrate sample, blending and stretching of OH groups of weakly bonded on the surface of adsorbed water molecule.
1730 and 3150	Bending and stretching mode of the chemisorbed/ interlamellar.
2900	Strong interaction between Ti ions and O-H groups(shoulder).
1400	Mn-OH bending vibration.
1100	Formation of Ti-O groups during alkaline synthesis.
974	Bending vibrations of Ti-OH non-bridging bonds.
919	Deformation of a hydrogen bond on -OH group.
920-910	Ti-O bonds in TiO ₆ Octahedra.
902	Four coordinated Ti-O stretching modes.
680	Vibration of bridging oxygen atoms coordinated with Na ions.
517 and 487	Mn-O stretching modes of the Octahedral layers in the birnessite structure.
470	Ti-O-Ti vibrations of the interconnected octahedral that are rigid units of the tubes wall formation.

The surface chemical composition and valence state of MnO₂-TNTs samples were carried out by XPS technique. XPS spectra fully scanned spectra indicated that Ti, Mn, O, Na, and K elements as in Figure 4.13.

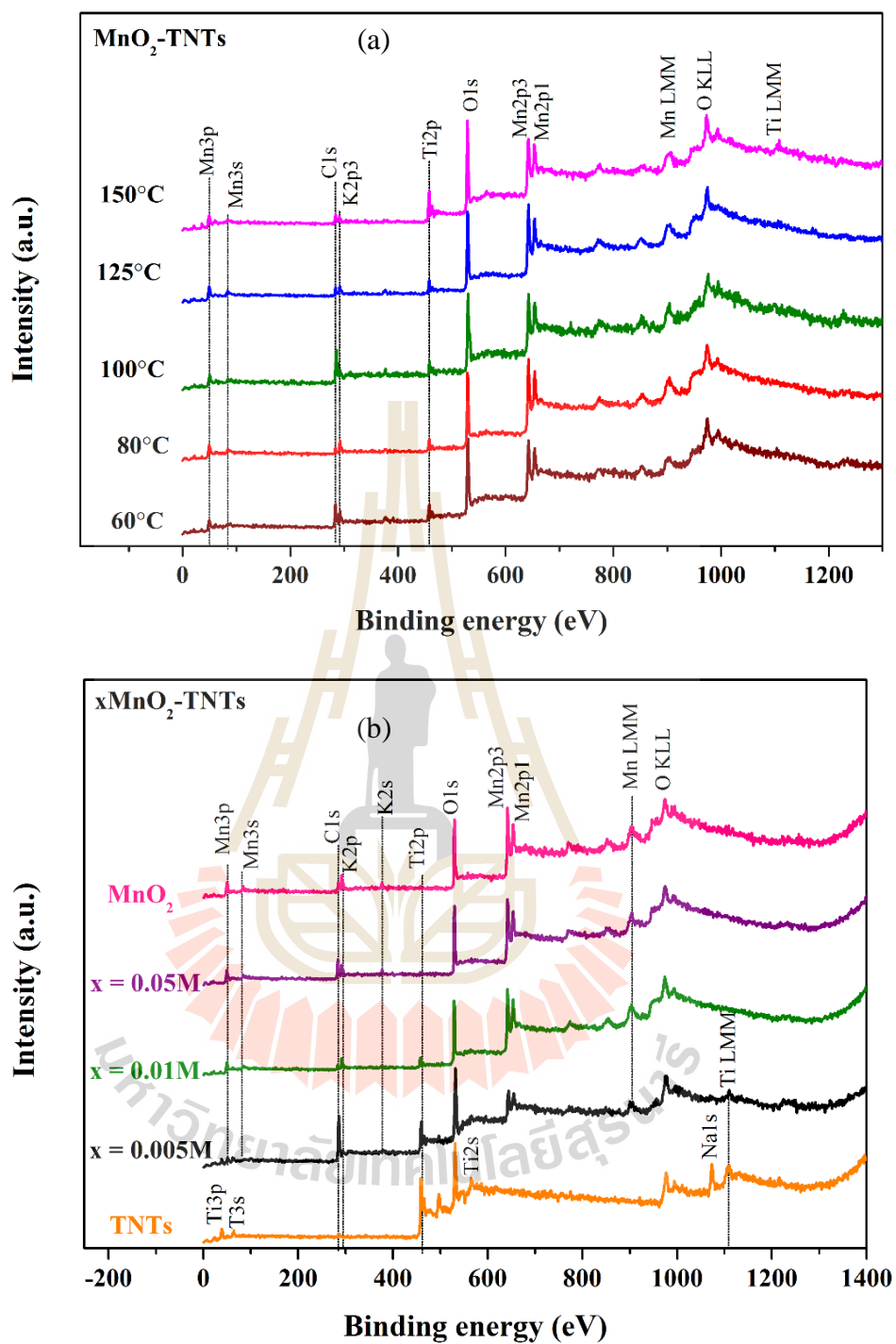


Figure 4.13 XPS survey scan of (a) xMnO₂-TNTs (x = 0.01M) with different hydrothermal temperatures and (b) a compositions effect.

Figure 4.14 XPS Mn 2p spectra of MnO₂-TNTs as a function of temperature reaction and composition ratio effect. The Mn 2p region consists of a spin orbit doublet with binding energy of 654.10-654.84 eV (Mn 2p_{1/2}) and 642.10-642.66 eV (Mn 2p_{3/2}). Two main peaks of the Mn2p XPS spectrum exhibits a spin-energy separation of 11.71, 11.74, 11.82, 11.83, 11.56 eV for 60, 80, 100, 125 and 150°C, respectively. High content of xMnO₂-TNTs shows the spin-energy separation shows 10.99, 11.74, and 11.77 eV where x = 0.005M, x = 0.01M, and x = 0.05M, respectively. The core level spectra of Mn 2p were fitted into four peaks associate with Mn³⁺ and Mn⁴⁺ as detail in Table 4.2. Generally, the near surface of birnessite have assumed Mn²⁺, Mn³⁺, and Mn⁴⁺ which high spin states of the Mn 2p_{3/2} spectrum is make up of more than one species of Mn chemical state (Nesbitt and Banerjee, 1998; Wang *et al.*, 2017). The report have assumed that the Mn⁴⁺ is firstly reduced to Mn³⁺ by electron injection then further reduced to Mn²⁺ (Takashima *et al.*, 2012). Otherwise Mn³⁺ arose on the surface because the electrostatic balance by oxygen vacancies (Li *et al.*, 2017). The Mn 2p XPS results could be confirmed that in all of samples is a mixture of oxidation states.

K 2p spectra was analyze show in Figure 4.15. K 2p spectra are present in all sample and the content increase with increasing of KMnO₄ concentrate. This conclude that more birnessite-type MnO₂ was loaded on the TNTs which high concentration of MnO₄⁻ (Lei *et al.*, 2012). The interlayer space of δ-MnO₂ crystal was presence with K⁺ ions that was quantified the K 2p spectra relatively with Mn 2p. This is due to the incorporation of potassium ion under the autogenous pressure condition into the MnO₂ matrix. However, the present of large K⁺ inside the porous MnO₂ matrix have an appreciable effect on the electrochemical (Subramanian *et al.*, 2005)

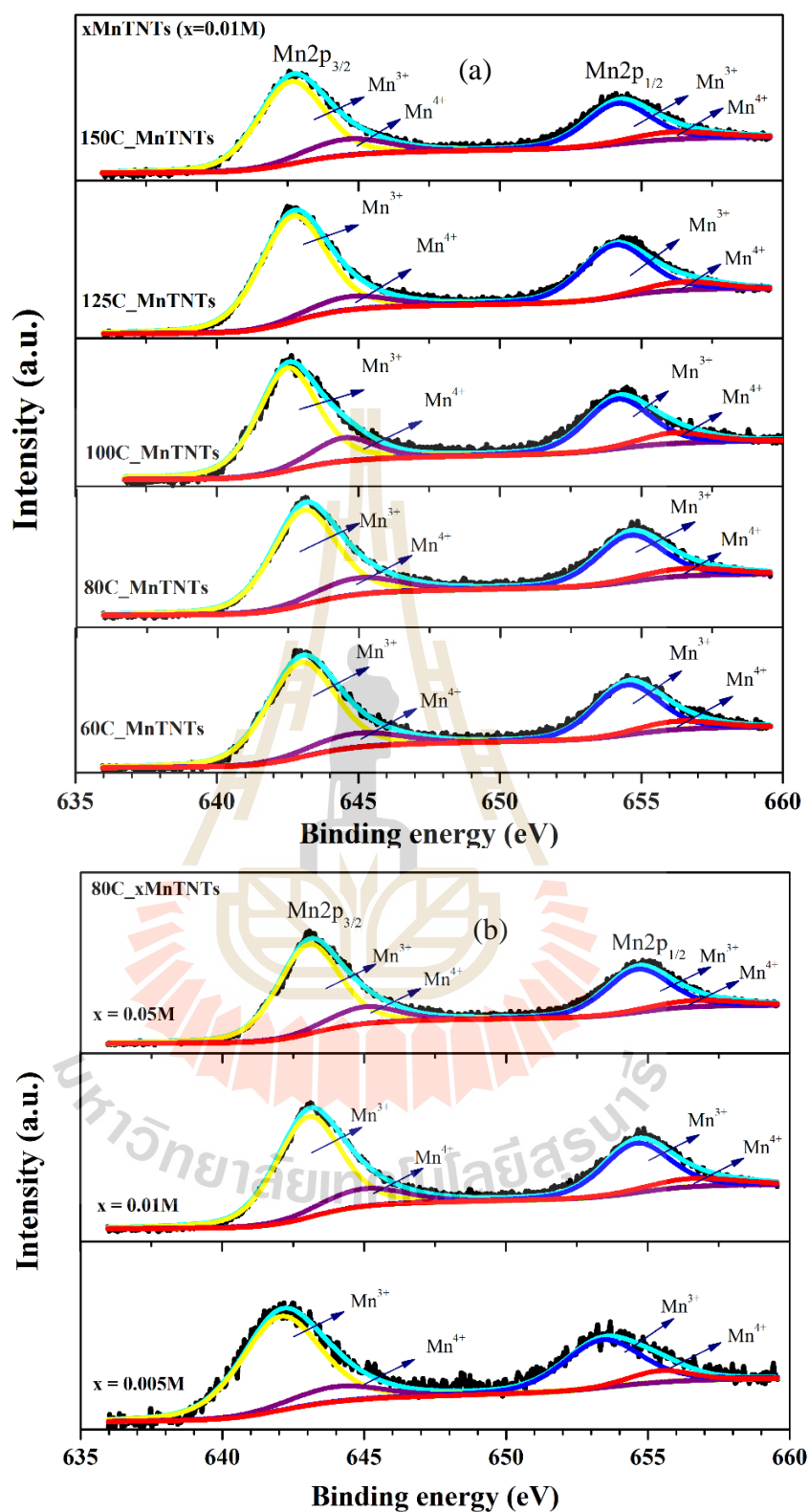


Figure 4.14 XPS Mn 2p spectra of MnO₂-TNTs as (a) a function of temperatures reaction and (b) composition ratios effect.

Table 4.2 Results of peak fitting for MnO₂-TNTs in the Mn 2p region.

Sample	Mn2p binding energy (eV)						Relative peak area (%)					
	Mn 2p _{3/2}		ΔEnergy	Mn 2p _{3/2}		Mn 2p _{1/2}		Mn 2p _{3/2}		Mn 2p _{1/2}		
	Mn 2p _{3/2}	Mn 2p _{1/2}		Mn ³⁺	Mn ⁴⁺	Mn ³⁺	Mn ⁴⁺	Mn ³⁺	Mn ⁴⁺	Mn ³⁺	Mn ⁴⁺	
60C_xMnTNTs	642.81	654.54	11.71	642.96	644.97	654.47	656.25	56.25	10.42	28.13	5.21	
80C_xMnTNTs	643.10	654.84	11.74	643.03	644.97	654.59	656.49	54.47	12.20	27.24	6.10	
100C_xMnTNTs	642.66	654.48	11.82	642.49	643.50	653.16	655.13	54.10	12.56	27.05	6.28	
125C_xMnTNTs	642.52	654.35	11.83	642.67	644.72	654.06	654.44	57.85	8.82	28.92	4.41	
150C_xMnTNTs	642.54	654.10	11.56	642.60	644.60	654.17	656.08	53.70	12.97	26.85	6.49	
80C_xMnTNTs												
x = 0.005M	642.18	653.17	10.99	642.05	644.05	653.39	655.43	56.28	10.39	28.14	5.19	
x = 0.05M	643.05	654.82	11.77	643.03	645.00	654.63	656.62	54.85	11.82	27.43	5.91	

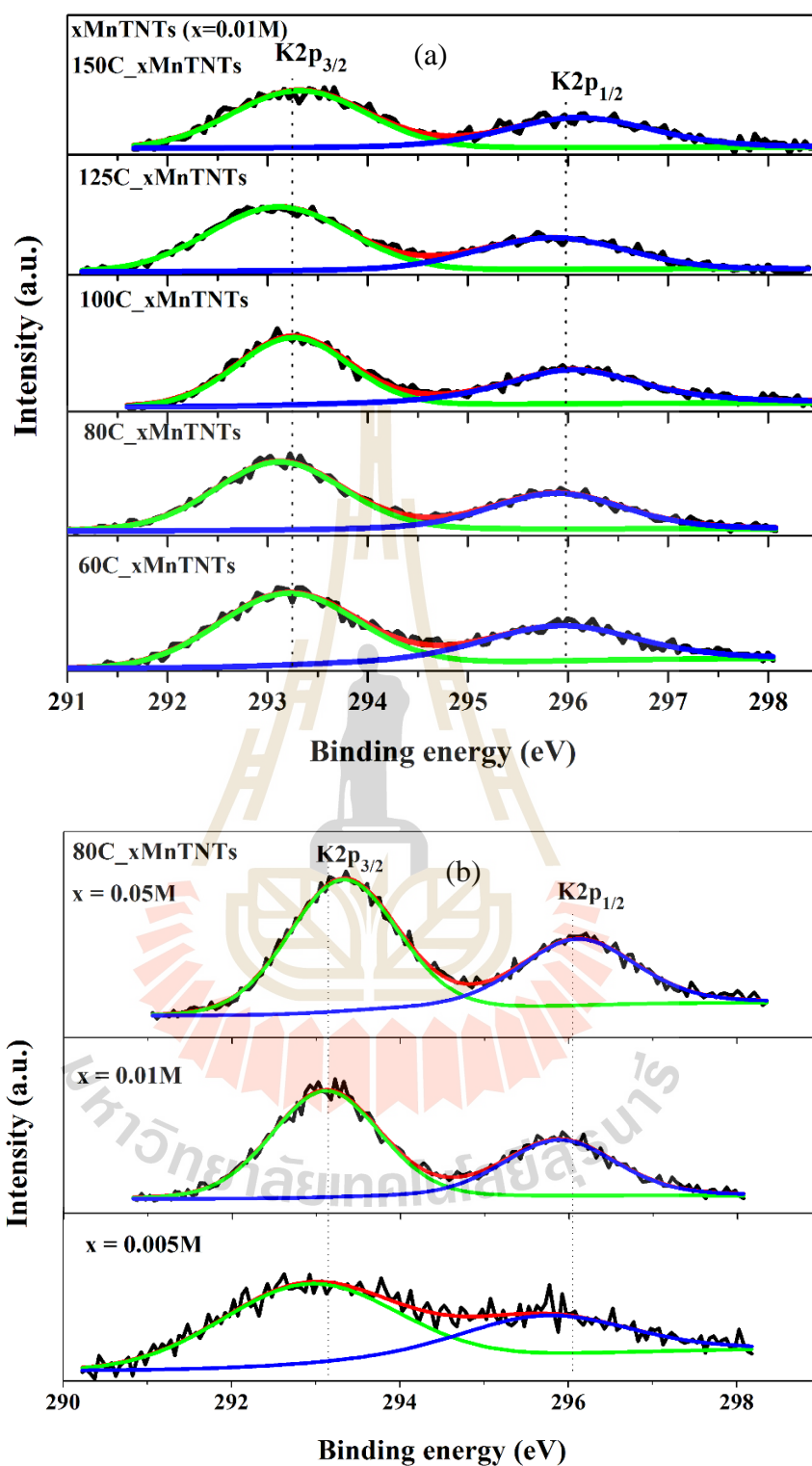


Figure 4.15 XPS K 2p spectra and splitting energy of MnO₂-TNTs as a function of (a) temperatures reaction and (b) composition ratios effect.

Table 4.3 Results of peak fitting for MnO₂-TNTs in the Ti 2p region.

Sample	Ti2p binding energy (eV)			Relative peak area (%)	
	Ti2p _{3/2}	Ti2p _{1/2}	ΔEnergy	Ti2p _{3/2}	Ti2p _{1/2}
xMnTNTs (x=0.01M)					
60C_xMnTNTs	458.58	464.31	5.73	68.02	31.98
80C_xMnTNTs	458.59	464.34	5.75	65.71	34.29
100C_xMnTNTs	458.65	464.29	5.64	67.82	32.18
125C_xMnTNTs	458.54	464.32	5.77	65.66	34.34
150C_xMnTNTs	458.65	464.33	5.68	67.18	32.82
80C_xMnTNTs					
x = 0.005M	458.56	464.23	5.67	64.98	35.02
x = 0.05M	458.94	464.69	5.75	71.57	28.43

To study the Ti elemental valence in MnO₂-TNTs are given in Figure 4.16 confirming that Ti element is in Ti⁴⁺ state which the binding energy and relative area between Ti 2p_{3/2} and Ti 2p_{1/2} are assignment in Table 4.2. The energy splitting between Ti 2p_{1/2} and Ti 2p_{3/2} was 5.7 eV, indicating a normal state of Ti⁴⁺ is present in all samples. The TNTs structure confines Na⁺ presence that synthesized by NaOH high concentration. XPS of Na1s spectra show in Figure 4.17 reveal that low temperature

reaction shows amount of Na^+ and absence with higher temperature reaction as in high content of MnO_2 in MnO_2 -TNTs materials.

The observed binding energy spectrum for the O 1s core level are show in Figure 4.18. The first peak with lowest binding energy (530 eV) of O1s spectra attributed to O1s binding energy in anhydrous of the oxygen atoms bonded with Mn-O ($\text{O}_{\text{lattice}}$) or associated with O^{2-} ions that within the structure of Ti-O lattice. The peak at 529.8 eV is a typical of metal-oxygen bonds (Zhu *et al.*, 2015). Intermediate binding energy (531.5 eV) peak relate with the adsorbed hydroxyl group (O_{OH}) such as O_2^{2-} or O^- in forms of hydroxyl OH^- and carbonate CO_3^{2-} species on the surface of the materials which preferable at the oxygen vacancy sites. Higher energy (532.8 eV) usually corresponding to the adsorbed molecular water (O_{mw}) (Tang *et al.*, 2014; Soumen *et al.*, 2014). Additional peak at 534 eV was observed at 100C_xMnTNTs which agreement with the single bonds of carbon oxygen (O_{C}) (He *et al.*, 2017; Sadri *et al.*, 2017). These values are discussion in Table 4.4.

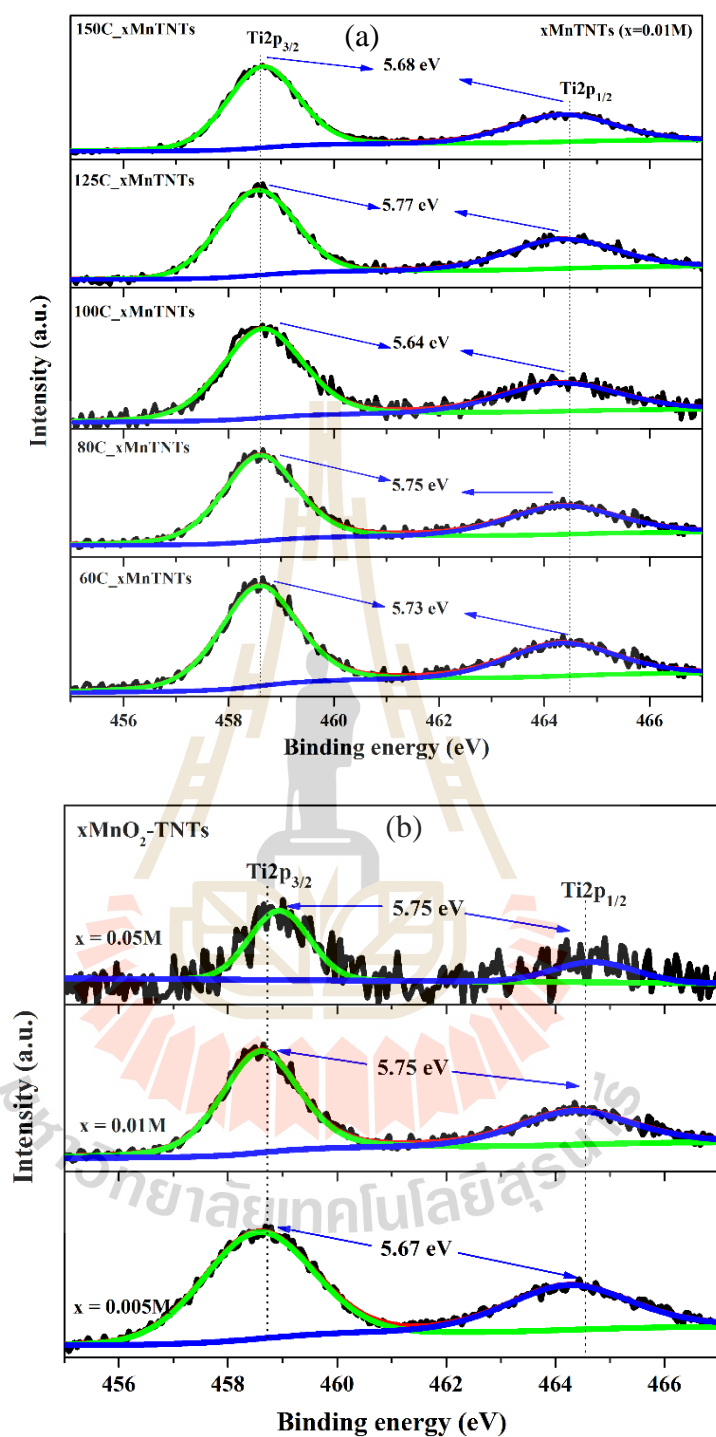


Figure 4.16 XPS measurement results of Ti 2p spectra and splitting energy of MnO₂-TNTs.

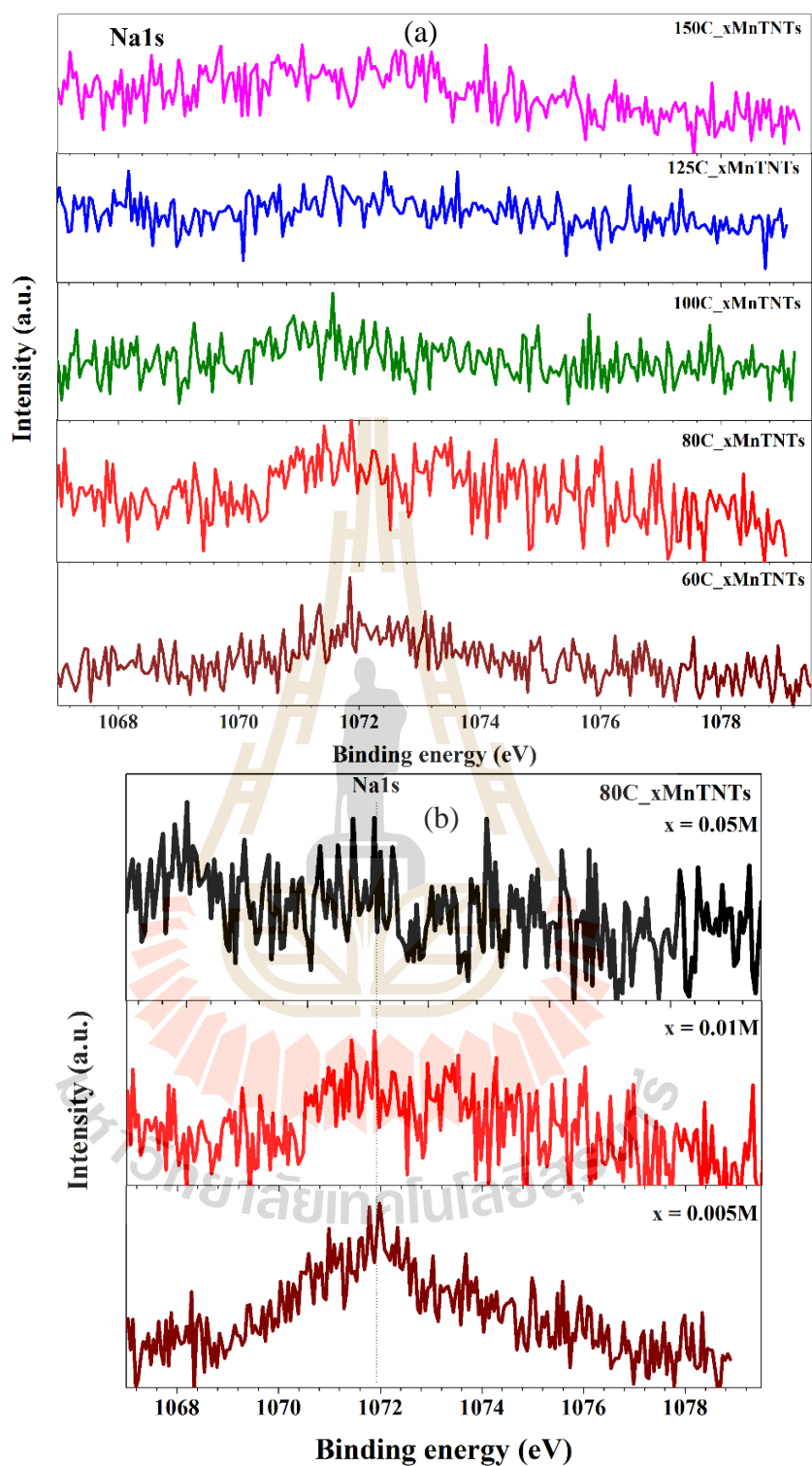


Figure 4.17 XPS Na 1s spectra and splitting energy of MnO₂-TNTs as a function of temperature reaction and composition ratios effect.

Table 4.4 Results of peak fitting for MnO₂-TNTs in the O 1s region.

Samples	O 1s Binding energy (eV)				Relative peak area (%)			
	O _{lattice}	O _{OH}	O _{mw}	O _C	O _{lattice}	O _{wm}	O _{OH}	O _C
xMnTNTs (x = 0.01M)								
60C_xMnTNTs	530.54	532.15	533.22		81.04	12.8	6.16	
80C_xMnTNTs	530.44	532.05	532.89		89.13	5.33	5.54	
100C_xMnTNTs	530.46	531.68	533.42	534.84	51.09	17.72	16.52	14.67
125C_xMnTNTs	530.50	532.13	533.22		83.18	12.82	4.00	
150C_xMnTNTs	530.47	532.10	533.20		81.04	13.14	5.82	
80C_xMnTNTs								
x = 0.005M	530.39	532.22	533.43		77.13	14.08	8.79	
x = 0.05M	530.64	532.23	533.19		75.17	17.42	7.4	

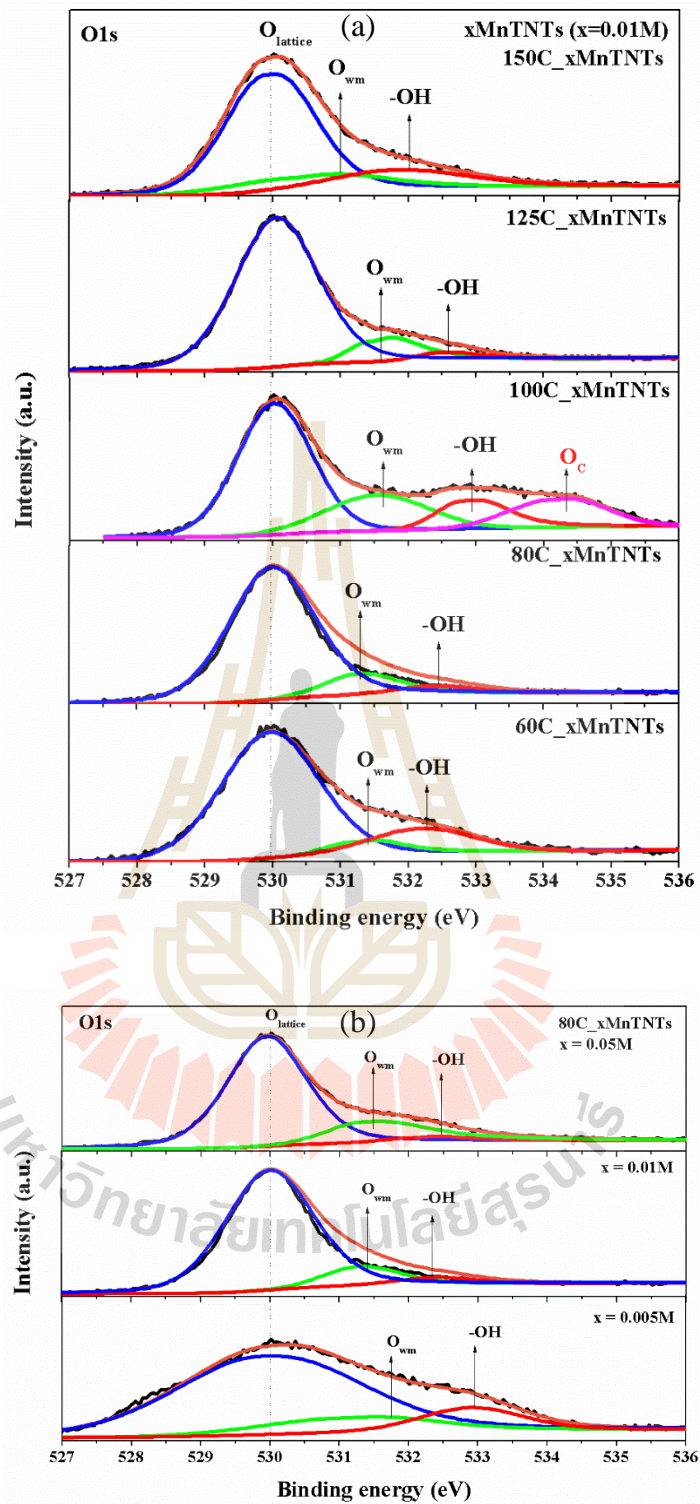


Figure 4.18 XPS O 1s spectra and splitting energy of MnO₂-TNTs as a function of temperatures reaction and composition ratios effect.

4.2.5 Adsorption analysis of MnO₂-TNTs materials

The nitrogen adsorption and desorption isotherms of MnO₂-TNTs powder are shown in Figure 4.19. The N₂ adsorption and desorption isotherms characteristic of type IV are taking place in mesopores. Initial part of the type IV isotherm is attributed to monolayer-multilayer adsorption since it follows the same path as the corresponding part of a type II isotherm obtained with the given adsorptive on the same surface area of the adsorbent in a non-porous form. From the isotherms can be observed that all samples displayed type IV isotherms according to IUPAC classification. Their pore size distributions are observed, the samples had mesopore. The BET surface area of TNTs precursor was agreement to the number and length of nanotubes, the increasing of tubular length corresponding to the time and NaOH concentration (Vu *et al.*, 2014). As in Figure 4.20 and Table 4.5 show highest BET surface area in 80 °C. The smallest total pore volume in 150 °C while high mean pore diameter in 100 °C. The adsorption of MnO₂-TNTs materials is depending on the quality of composition between MnO₂ and TNTs. This significant by temperature reaction which related to their morphology in SEM and TEM image. The phase composition and decoration limit as in MnO₂ in the space of TNTs, ultra thin of MnO₂ flakes and shape changes. Several MnO₂ content was decorated on TNTs relatively in low specific surface area of MnO₂-TNTs.

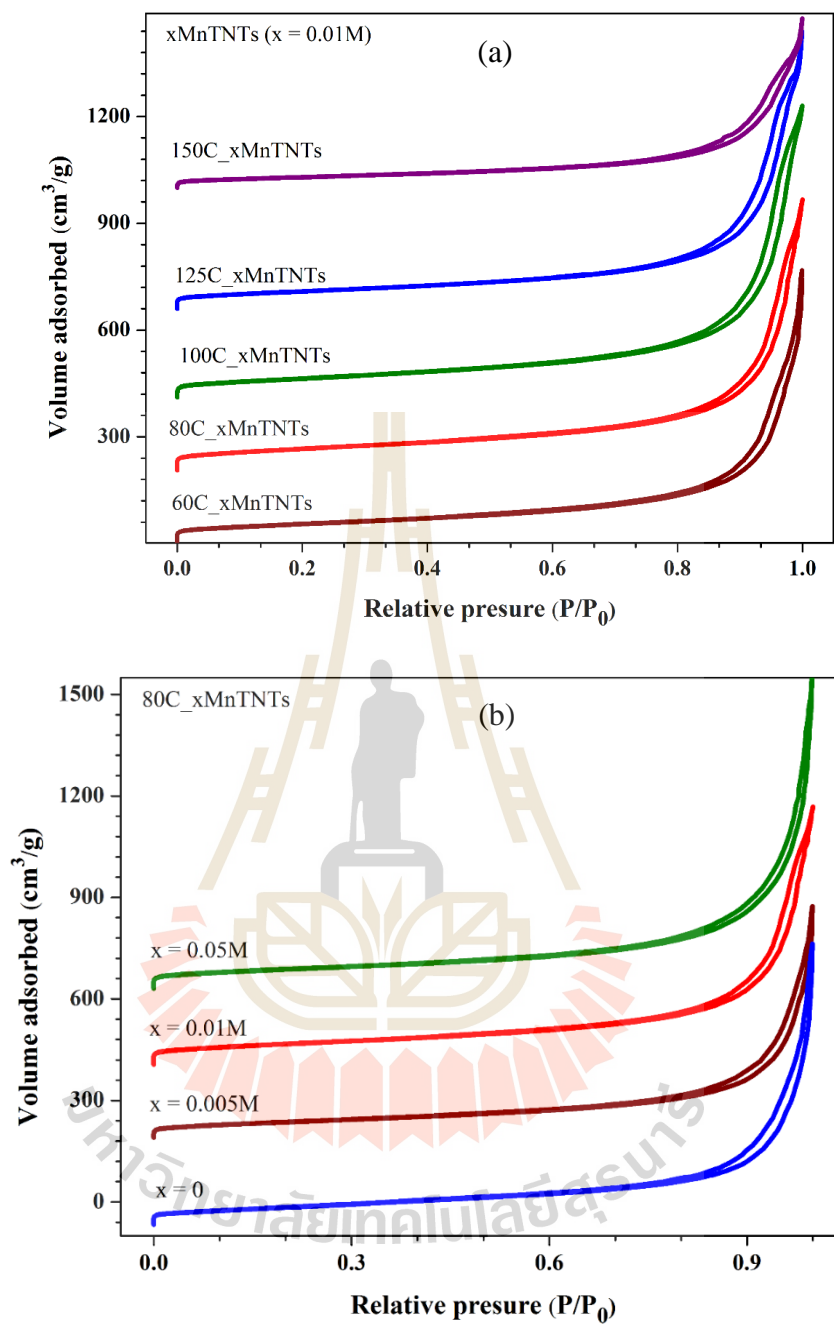


Figure 4.19 The isotherm N₂ adsorption and desorption of MnO₂-TNTs were treatment with (a) different hydrothermal temperature and (b) composition ratios.

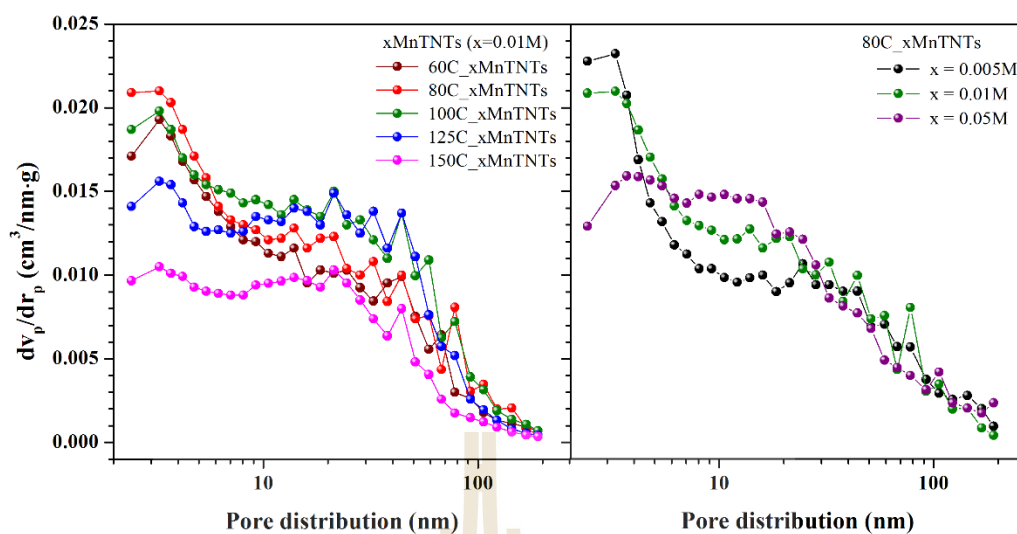


Figure 4.20 A pore volume distribution of MnO₂-TNTs materials.

Table 4.5 Specific surface area, pore volume and diameter of MnO₂-TNTs materials.

xMnO ₂ -TNTs	BET surface area (m ² /g)	Total pore volume (m ³ /g)	Mean pore diameter (nm)
x = 0.01M			
60C_xMnTNTs	194.03	0.85	17.52
80C_xMnTNTs	229.19	1.01	17.59
100C_xMnTNTs	206.97	1.14	22.10
125C_xMnTNTs	185.47	1.00	21.64
150C_xMnTNTs	121.48	0.60	19.72
80C_xMnTNTs			
x = 0.005M	194.00	0.99	20.49
x = 0.01M	229.19	1.01	17.59
x = 0.05M	203.00	1.00	19.61
TNTs	199.19	0.85	17.09

4.3 Electrochemical properties of MnO₂-TNTs materials

4.3.1 Na₂SO₄ electrolyte

Firstly, 1M Na₂SO₄ solution used in electrolyte for all electrode testing refer to reference review. Electrochemical measurement in the CV, GCD and GCD repeated charge-discharge for cycling stability. Optical observation founds dissolution of brown/yellow into the electrolyte are given in Figure 4.21(a) which difference testing in 0.5M Na₂SO₄. Electrode mass loading in 1M Na₂SO₄ is 4.27 mg and in 0.5M Na₂SO₄ is 2.31 mg. Capacity retention were tested with loading mass of electrode materials is 3.36 mg and 1.68 mg for 1M and 0.5M Na₂SO₄, respectively. The observation in experimental system would be perform with low active mass for the stable of record and current applying.

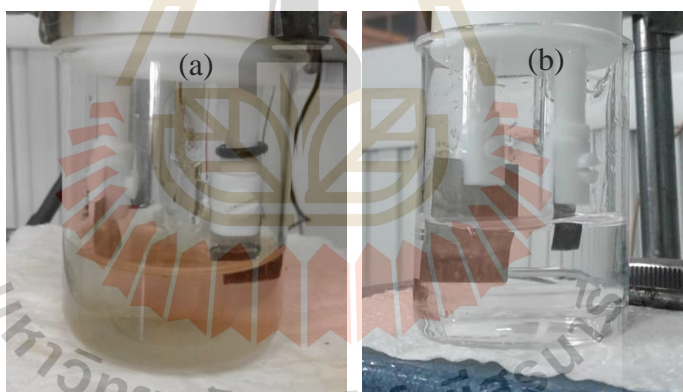


Figure 4.21 The schematic of electrochemical chamber consist of electrodes are performing in (a) 1M and (b) 0.5M Na₂SO₄ solution after 1000 cycles.

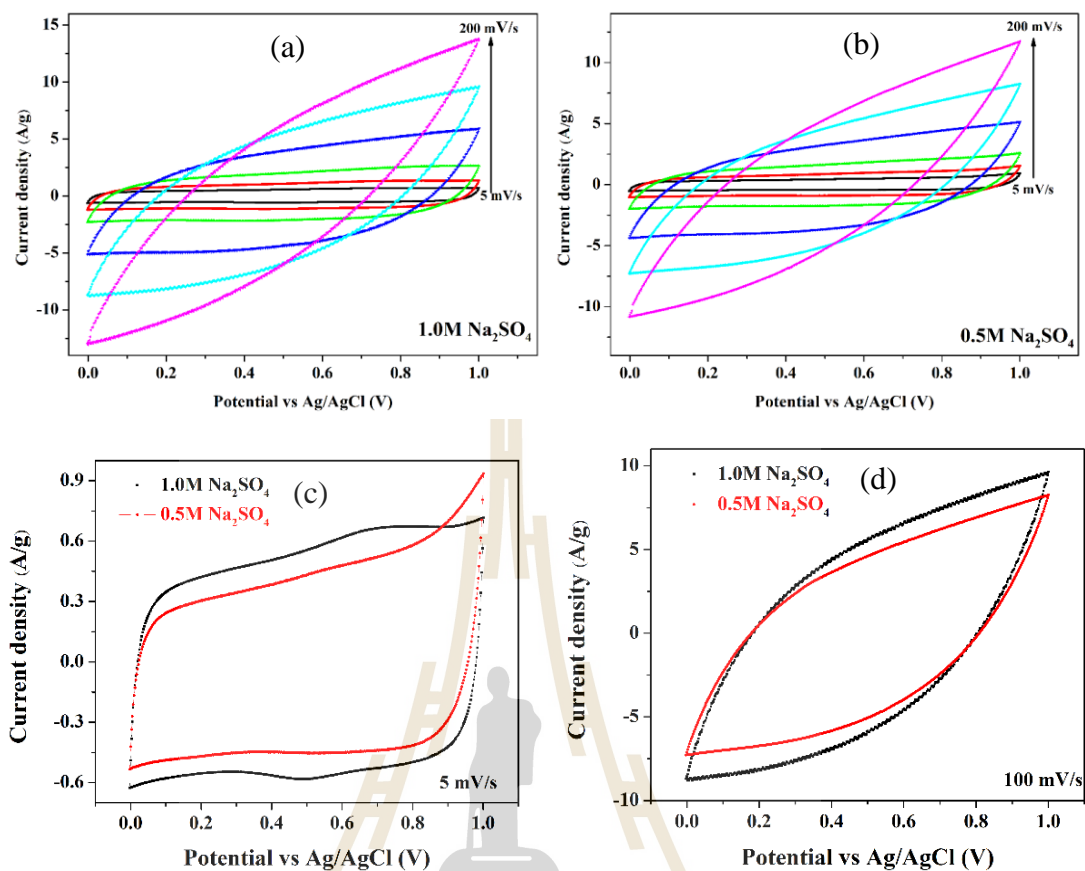


Figure 4.22 CV curve of MnO₂-TNTs electrode as a function of (a) 1M and (b) 0.5M Na₂SO₄ electrolyte. (c-d) CV curves obtained at low (5 mV/s) and high (100 mV/s) scan rate present the electrochemical behavior against different Na₂SO₄ electrolyte concentration.

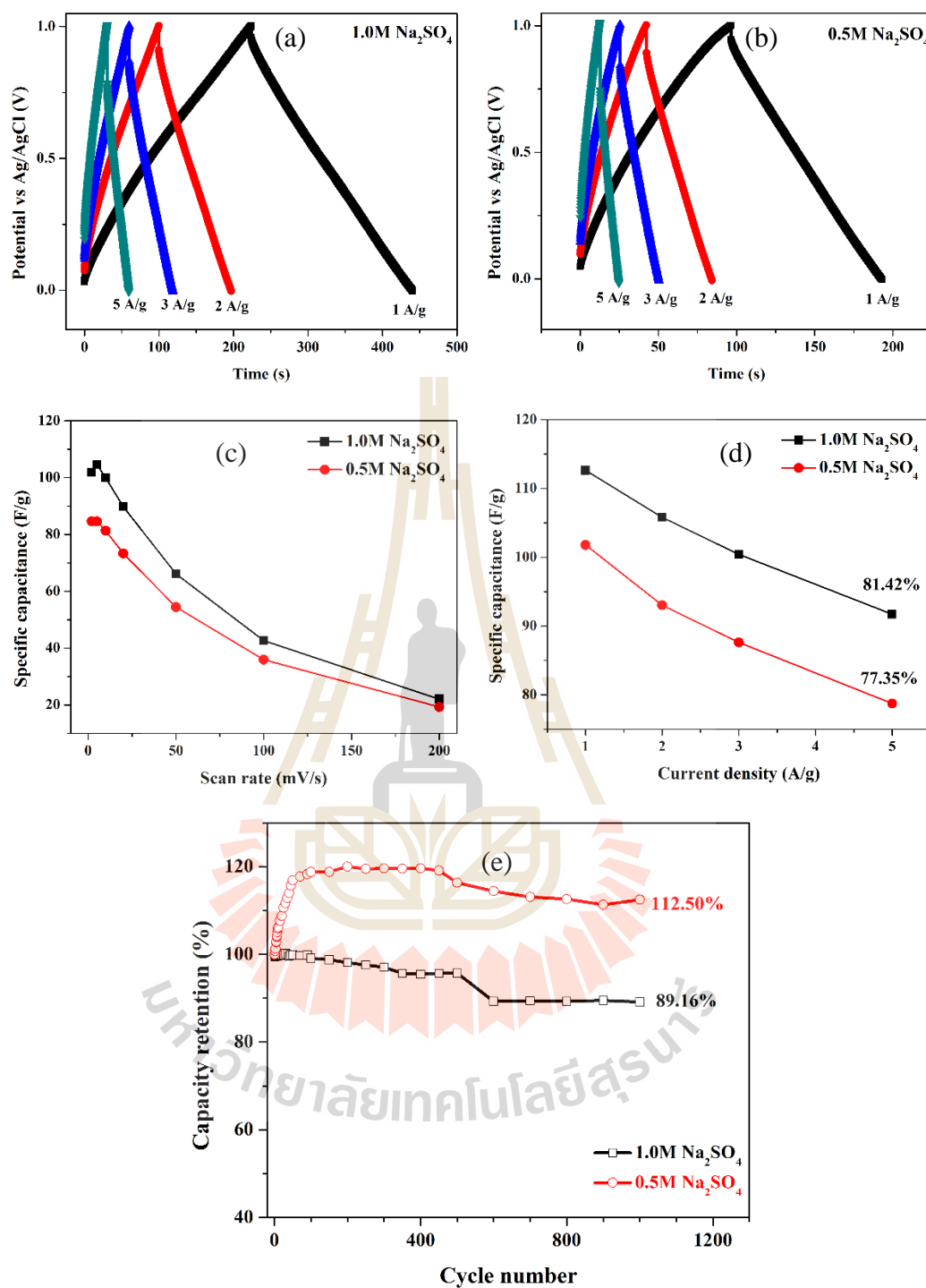


Figure 4.23 The GCD duration of MnO₂-TNTs electrode as a function of (a) 1M and (b) 0.5M Na₂SO₄ electrolyte with current density of 1-5 A/g. The specific capacitance calculated from (c) CV and (d) GCD curves. (e) The capacity retention as different of Na₂SO₄ electrolyte concentration after 1000 cycles.

CV curve versus scan rate from 5 mV/s to 200 mV/s presenting rectangle at low rating and spindle shaped with increasing of rating scan. At 5 mV/s, show parallel curve are clearly obtained in cathodic and anodic peak with 0.5M Na₂SO₄, prominent oxidation tail because the upper end potential (Fatemeh Ataherian, 2010). The area of CV curves depends on the accessible of electrolyte ions number per time. The specific capacitance was estimated from area of CV curve and calculated by discharge time with GCD testing. Electrolyte concentration of system testing are important for the specific capacitance of electrode materials. Long term behavior of electrode was considering for electrode stability with many cycles. Which this result show that higher specific capacitance in 1M Na₂SO₄ may be not fine in long term. Yan *et al.* (2014) reported that the capacitances obtained are quite close at low scan rate (5 mV/s) and show large follow by 2M, 1M and 0.1M. The concentration of electrolytes is important for ion transport resistance. However, active mass is different in comparison for the effect to CV curve and GCD results. Clearly seen the effect of Na₂SO₄ concentration with long term behavior in GCD repeated for study the cycling stability of MnO₂-TNTs electrode materials.

4.3.2 The effect of hydrothermal temperatures on electrochemical properties

The working electrode was fabricated from a mixture of active materials, PVDF, and Carbon black in NMP which coated on Nickle foam as current collector. The active mass found to be 1.26, 1.26, 1.82, 1.69, 1.75 mg for MnO₂-TNTs was related to 60°C, 80°C, 100°C, 125°C, and 150°C, respectively. Electrochemical characterization in CV, GCD and EIS mode with 0.5M Na₂SO₄ used in electrolyte. The CV curve at

various scan rate from 5 mV/s to 200 mV/s show as in Figure 26. All of electrode materials show rectangular shape CV curve and higher CV current indicate the high conductivity and low internal resistance.

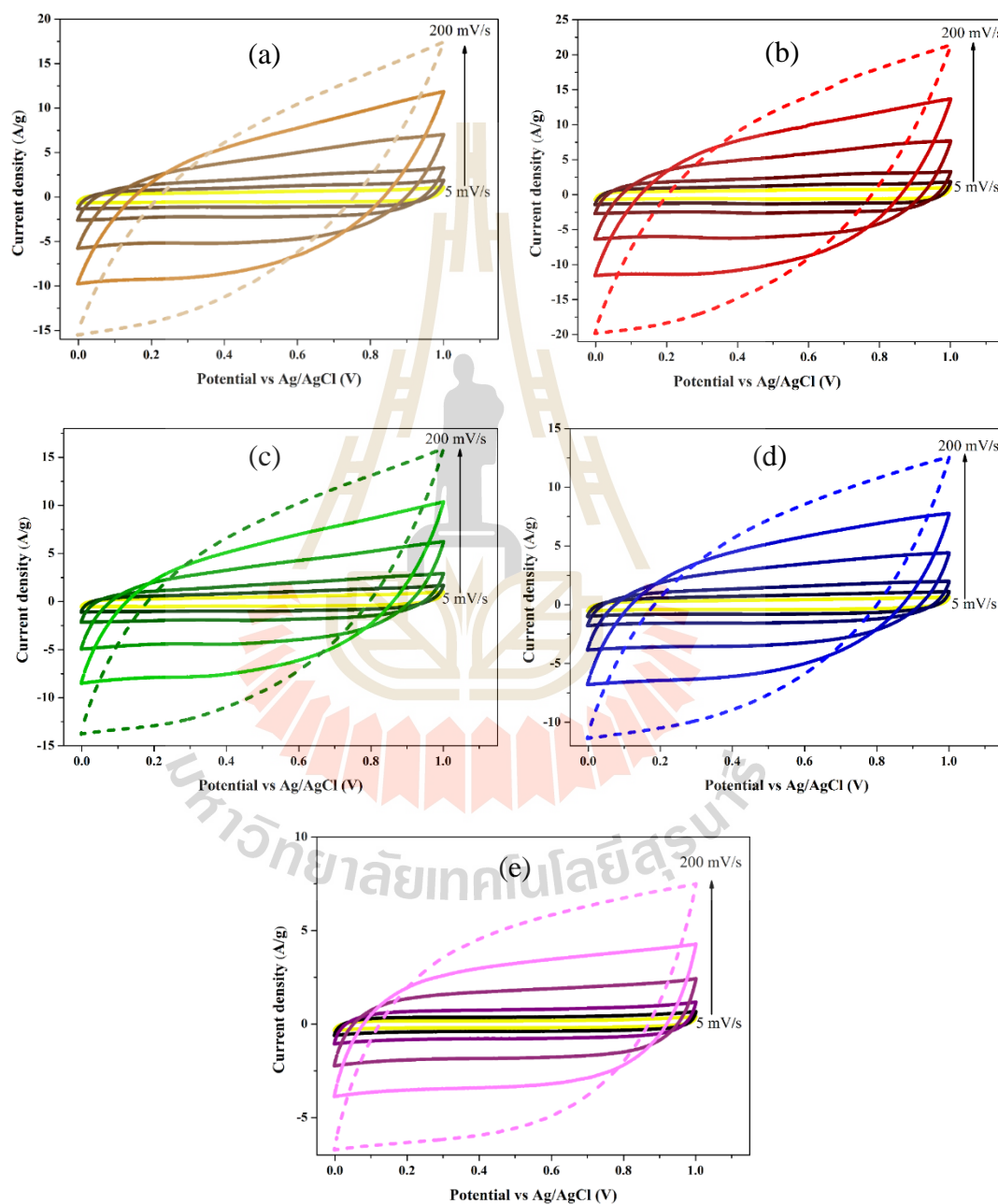


Figure 4.24 CV of MnO₂-TNTs electrode materials were synthesized at (a) 60°C, (b) 80°C, (c) 100°C, (d) 125°C and (e) 150°C.

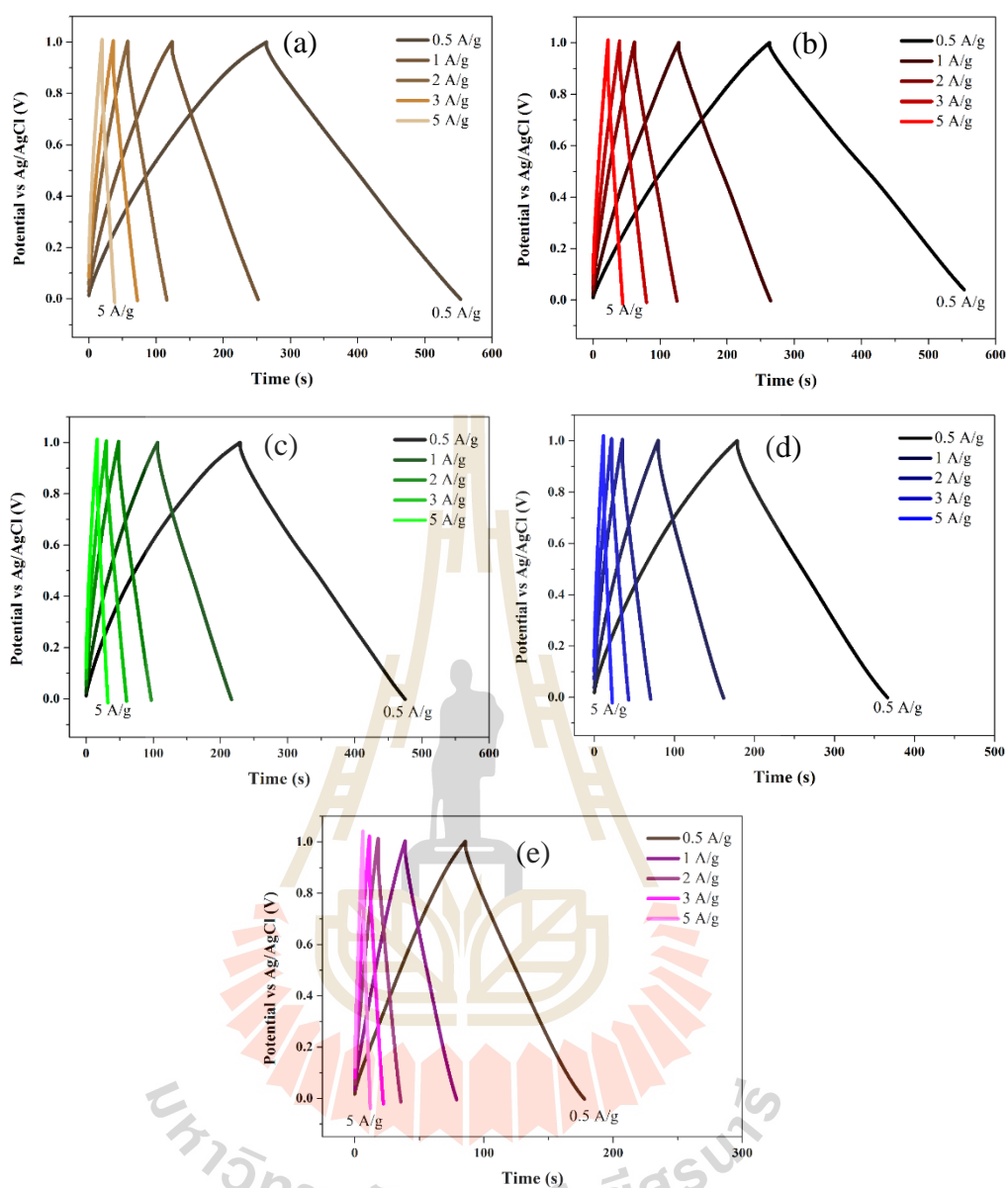


Figure 4.25 GCD curve of MnO_2 -TNTs electrode materials were synthesized (a) 60°C , (b) 80°C , (c) 100°C , (d) 125°C and (e) 150°C .

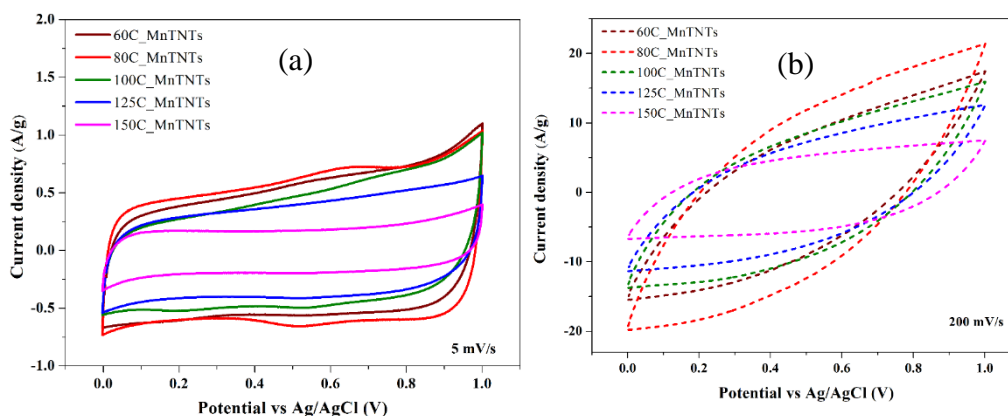


Figure 4.26 CV curve of MnO₂-TNTs electrode for rating scan (a) 5 mV/s and (b) 200 mV/s.

CV curve at low rating scan (5 mV/s) and high rating scan (200 mV/s) were given on Figure 4.26. CV curve at low scan rates 80°C and 100°C illustrations slight redox peaks reveal the pseudocapacitive behavior. This asymmetrical CV curves can be associate to the combined double layer and pseudocapacitive contributions to the total capacitance (Han *et al.*, 2014). Where MnO₂-TNTs was synthesized at 80°C relative larger CV current indicated that good electrochemical properties than another electrode. Sample of 60°C, 125°C and 150°C show without any peak in symmetry ideal rectangular indicated that the charging-discharging took place at a constant rate over the voltage 0 to 1V (Reddy and Reddy, 2003). The electrochemical reaction for MnO₂ in Na₂SO₄ neutral aqueous electrolyte is generally (Zhu *et al.*, 2014) show in below



where $\text{M}^+ = \text{Na}^+$ or H_3O^+ In fact, the MnO₂ involved redox reactions in the CV tests as the Mn atoms in the overlayers were converted into higher/lower valence states, which

was induced by the intercalation/extraction of alkali cations (Na^+) or protons (H_3O^+) into/out of the nanostructure (Shao *et al.*, 2015). CV characteristic for homogeneously without any change and high reversibility. This could be achieved by limiting the charge and discharge to potential window which corresponds to the highest stability of the redox processes (Pang *et al.*, 2000). Electrode materials with a hierarchical nanoarchitecture can not only provide the multiple large contact area, but also allow fast cation transport between the electrolyte and the electrode (Luo *et al.*, 2013). The hierarchical of MnO_2 on TNTs to design by different reaction hydrothermal temperature. The temperature optimized on materials structure for high effective. GCD curve of all electrodes within a potential window of 0-1.0 V at the current density of 1A/g show as in Figure 4.28(a). Long discharge time under current applying offer to large specific capacitance. The calculation results of the specific capacitance of five electrodes at different current densities are summarized in Figure 2.27. The rate capability of electrode materials with current applied in GCD testing. This condition is also good rate in charge-discharge with 0.5-5 A/g current density. The specific capacitance of five synthesized in conditions at 1 A/g is 132.10, 140.22, 113.30, 84.77, and 41.44 F/g for the 60°C, 80°C, 100°C, 125°C, and 150°C, respectively. The best achieved capacitance in 80°C sample, the interconnected MnO_2 create a highest specific surface area and more active sites for the adsorption of Na^+ which hence endows the 80°C show very high specific capacitance (Zhang *et al.*, 2014). The specific capacitance and BET specific surface area relation of different electrode represent as Figure 4.28. The phase composition between MnO_2 and TNTs confirm with XRD results, hierarchical of MnO_2 on TNTs given by SEM and TEM image. The effect of

hydrothermal temperature on MnO₂-TNTs electrode materials depend on the composition process between MnO₂ and TNTs materials. As in Figure 4.29 confirm that TNTs core independent on electrochemical studied. Liu *et al.* (2012) report the beneficial of amorphous MnO₂ for specific capacitance higher than crystal crystalline. This 80°C materials show high specific surface area for effective in high specific capacitance. Such good electrochemical performances are based on the unique coaxial nanostructure of Carbon nanofibers and MnO₂ nanocomposites, in which (i) the CNFs network with porosity and interconnectivity enables a fast electrolyte ions transport and provides continuous charge transfer pathways while (ii) the uniform and ultrathin MnO₂ coating offers short ion diffusion pathways for both ions and electrons (Wang *et al.*, 2011).

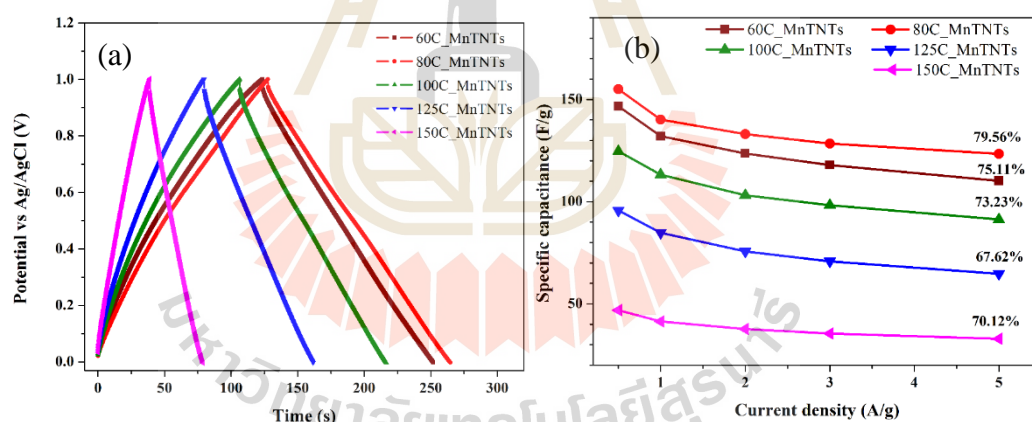


Figure 4.27 (a) GCD duration and (b) specific capacitance of MnO₂-TNTs electrode materials synthesized by different hydrothermal temperature.

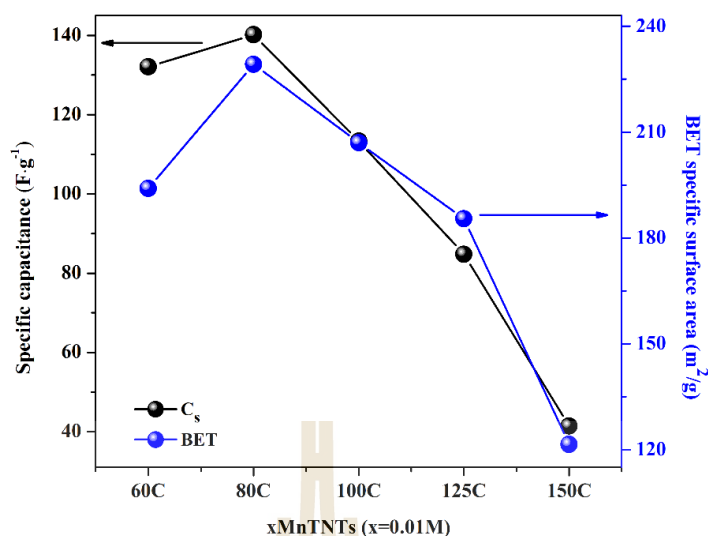


Figure 4.28 Specific capacitance related with BET surface area and of MnO_2 -TNTs synthesized as various hydrothermal temperature.

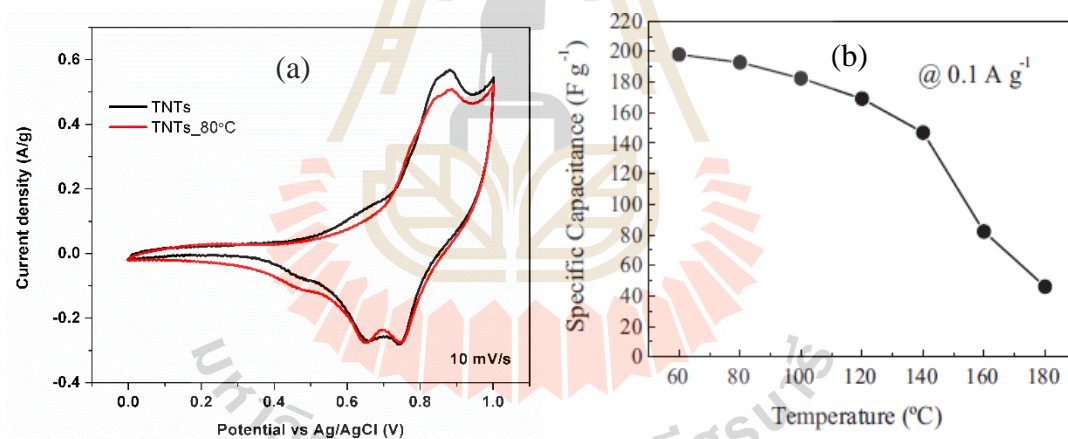


Figure 4.29 (a) CV curve of TNTs and TNTs treatment at $80^\circ C$ and (b) specific capacitance of MnO_2 electrode against hydrothermal temperature (Liu *et al.*, 2012).

The GCD technique was repeated in 1000 cycles to study the stability of electrode materials. At a current applied of $3 A/g$, the specific capacitance was calculated from discharge time for capacity retention (%). All samples, $xMnTNTs$ ($x = 0.01M$) electrodes with different temperatures synthesized show capacity retention of 91.95,

96.48, 111.60, 87.03, and 85.21% after 1000 cycles for 60°C, 80°C, 100°C, 125°C and 150°C, respectively. At 100 first cycles show the increase of capacity retention and are maintain in all sample this because the activation process. 100°C exhibits good retain because the highest pore size and more total pore volume. However, the BET surface area just optimizes for the insert of electrolyte ions. The hydrothermal treatment with different show that the effect on materials compose between two phases. This effect to morphology contact lead to the surface adsorption limiting.

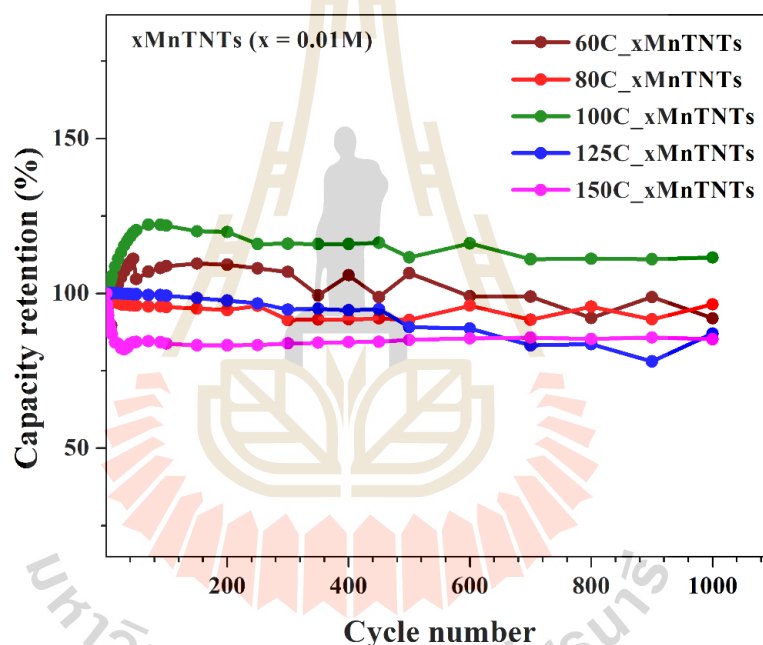


Figure 4.30 Cycling stability of MnO₂-TNTs electrode materials with 1000 cycles. Capacity retention calculate from the specific capacitance of discharge time which GCD tested at 3 A/g current density.

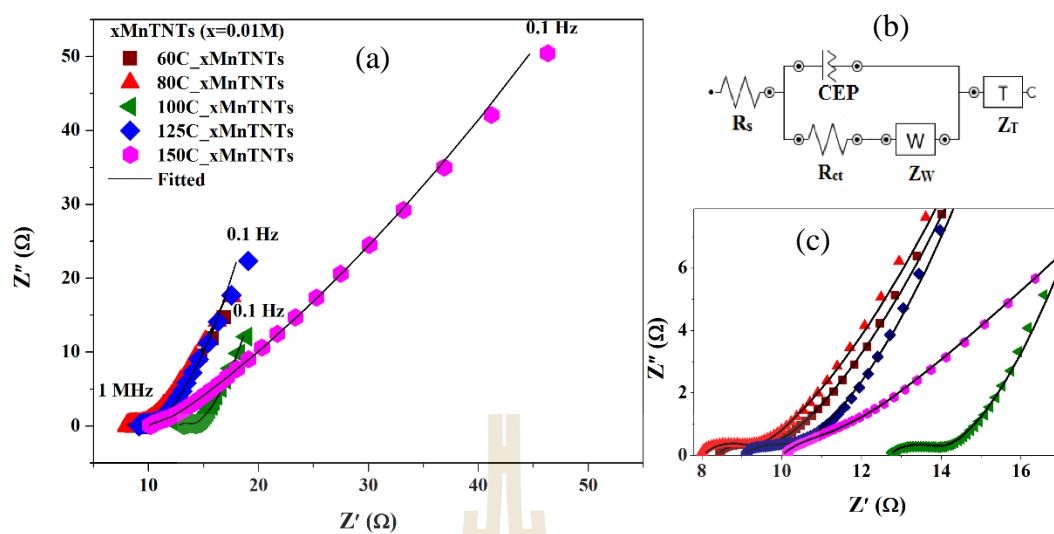


Figure 4.31 (a) Nyquist plot of MnO_2 -TNTs electrode materials synthesized by different hydrothermal temperature. (b) The equivalent circuit fitted and (c) enlargement of impedance.

Table 4.6 Fitted equivalent circuit elements of MnO_2 -TNTs electrode materials.

Electrode materials	R_s (Ω)	R_{ct} (Ω)	Z_W (Ω)	CEP (Ω)	Z_T (Ω)	χ^2
$x\text{MnTNTs}$ ($x = 0.01\text{M}$)						
60°C	8.35	1.28	7.52	507.10	1.40	0.002
80°C	8.05	1.25	8.60	840.12	1.19	0.003
100°C	12.67	1.37	5.14	336.553	1.23	0.001
125°C	9.02	1.34	8.84	219.69	1.88	0.004
150°C	10.00	1.96	43.64	267.97	1.32	0.002

The electrical behavior of MnO₂-TNTs electrode analyzing by EIS technique. As show in the Figure 4.31, Nyquist plots with the EIS data for the MnO₂-TNTs electrodes with various temperature synthesized. The EIS data can be fitted by an equivalent circuit consisting of a bulk solution resistance (R_s), a charge-transfer resistance (R_{ct}), Warburg impedance (Z_W), a constant element phase (CEP) and tan impedance (Z_T). MnO₂-TNTs electrode were synthesized at 60°C-100°C exhibits straight line in the low frequency region and a single semicircle in the high frequency region, indicating a diffusion-limited step in the low frequency region and a charge transfer limited step in the high-frequency region (Gao *et al.*, 2017). 125°C and 150°C, the Nyquist plot does not show any semicircular region, indicating the materials process low faradaic resistances in the electrolyte. The intercepts at the real axis with highest frequency region represent the R_s is the equivalent series resistance (ESR) which generally describes the resistance of the electrolyte combined with the internal resistance of the electrode. The intercept of the plot shows the trend value for R_s of 80°C < 60°C < 125°C < 150°C < 100°C. This a combined resistance of ionic resistance of electrolyte, intrinsic resistance of substrate, and contact resistance at the active material/current collector interface (Zhang *et al.*, 2014). The high to medium frequency semicircles correspond to the R_{ct} is the rate of redox reactions at the electrode interface. Based on fitted data, R_{ct} of 80°C is much lower than that 60°C and 100°C, suggesting that the largest surface area is more favorable for the charge transfer process (Zhang *et al.*, 2014). Low charge transfer resistance suggests fast ion transport within the supercapacitor. The near line plots in the low frequency region indicate the Z_W . Significantly, the optimization of the temperature and increase of the MnO₂ content

of MnO₂-TNTs, the electrode trend to show a lower R_s. The parameter for energy and power density are given the ragone plot as in Figure 4.32

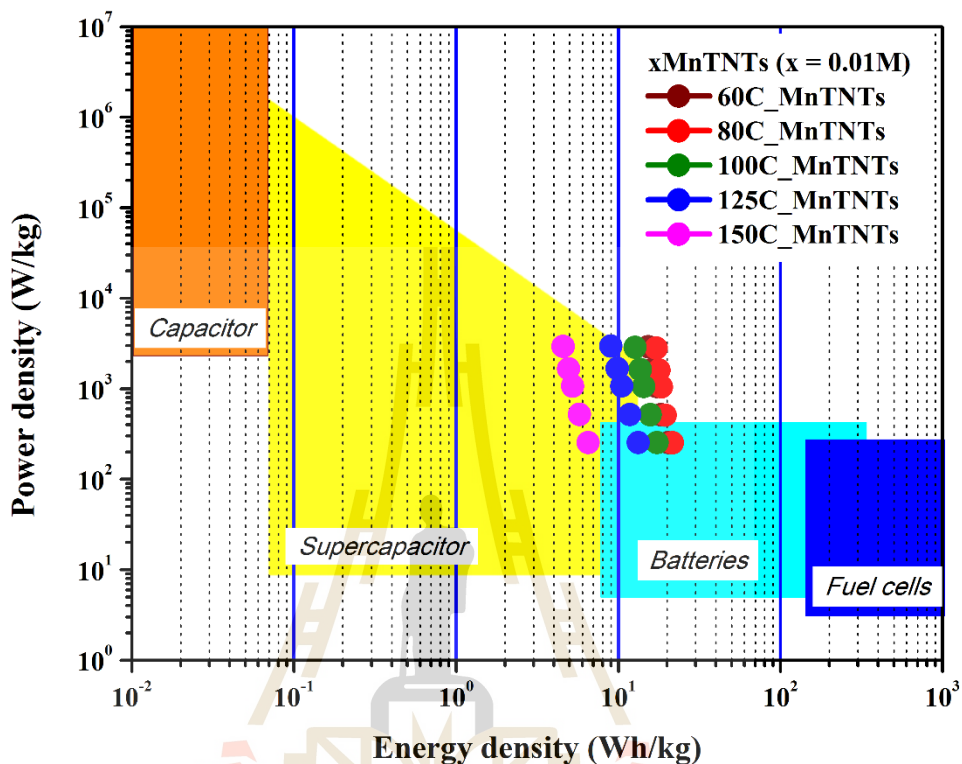


Figure 4.32 Ragone plot for MnO₂-TNTs electrode materials as a different hydrothermal temperature.

4.3.3 The effect of composition ratios of MnO₂-TNTs on electrochemical properties

MnO₂ were decorated on TNTs for improve the MnO₂ stability for electrode materials. KMnO₄ concentration were vary as 0.005M, 0.01M and 0.05M for control MnO₂ content effect on TNTs electrode materials. xMnTNTs where x = 0.005M, 0.01M and 0.05M at 80°C hydrothermal treatment. This loading active mass of 1.96, 1.26, and 1.26 mg, respectively. A comparison of CV curve, the electrochemical studied

were explained by CV technique which show that high content of MnO₂ is high effective area as in figure 4.33.

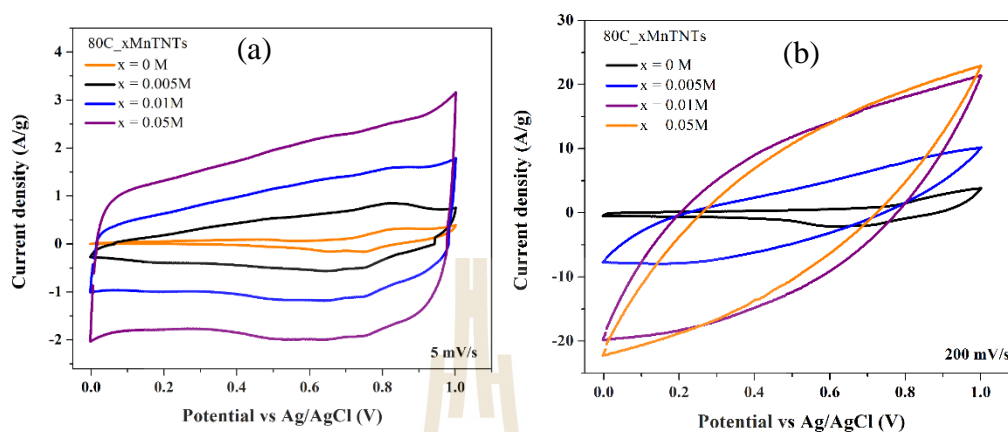


Figure 4.33 CV curve of MnO₂-TNTs electrode materials which consist with different MnO₂ on TNTs. (a) low scan rate is 5 mV/s and (b) high scan rate is 200 mV/s.

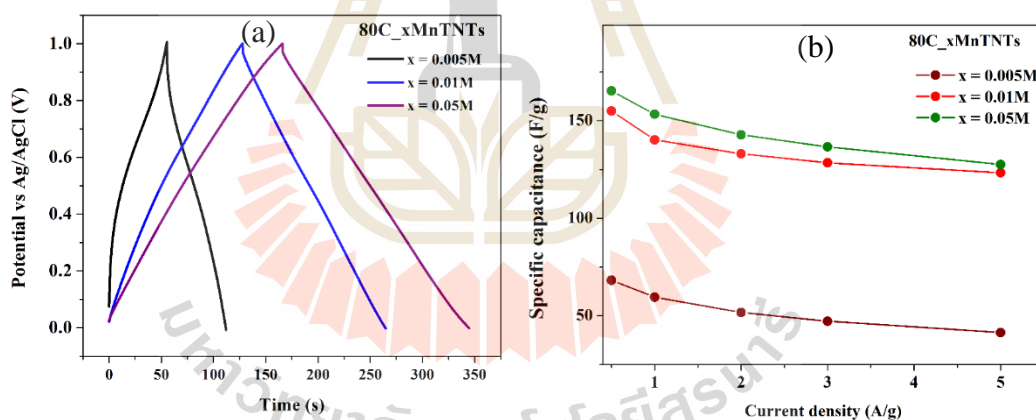


Figure 4.34 (a) GCD plots and (b) the specific capacitance versus current density (0.5-5 A/g) of MnO₂-TNTs electrode materials which consist with different MnO₂.

The GDC duration are given as Figure 4.34(a) for xMnTNTs electrode materials, the discharge time were used to calculate the specific capacitance. The specific capacitance of xMnTNTs electrode with $x = 0.005\text{M}$, $x = 0.01\text{M}$, $x = 0.05\text{M}$ are 59.57, 140.21, and 183.48 F/g, respectively. The specific capacitance as various of

current densities (0.5-5 A/g) of different MnO_2 in MnO_2 -TNTs electrode materials show in Figure 4.34(b). Even though, $x\text{MnTNTs}$ with $x = 0.05\text{M}$ show best in specific capacitance whereas lower in BET surface area. At the same temperature synthesized and different MnO_2 content in MnO_2 -TNTs materials, the specific capacitance depends on the MnO_2 content. At same content of MnO_2 show the effect of surface area, this conclude that TNTs not effective in MnO_2 -TNTs electrode materials. Specially, as in Figure 4.35 show the cycling stability of MnO_2 -TNTs electrode materials confirm that TNTs do not improve of electrochemical performance.

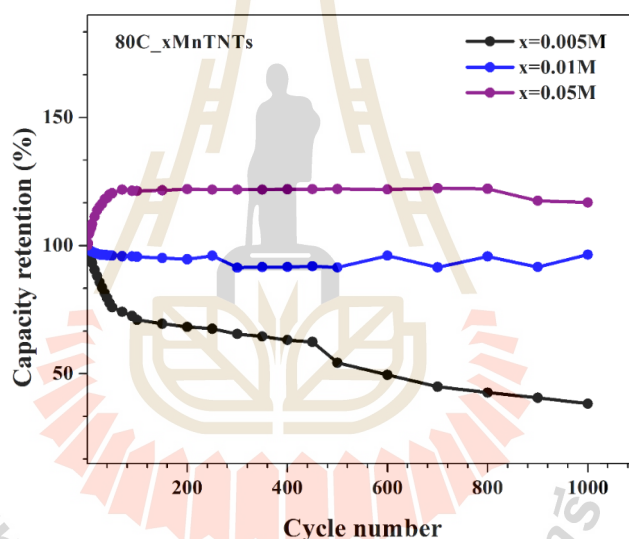


Figure 4.35 Capacity retention of MnO_2 -TNTs electrode materials with different MnO_2 content.

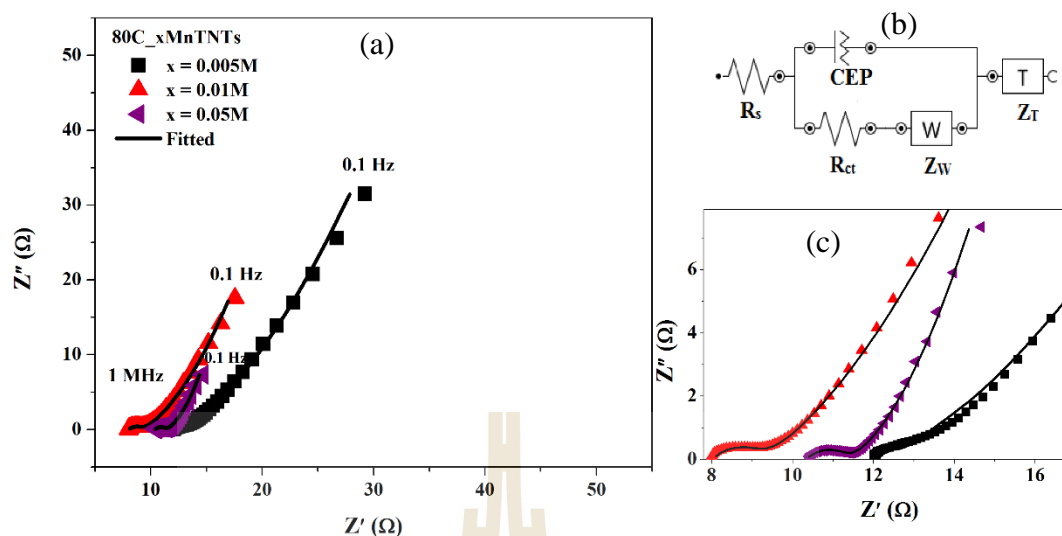


Figure 4.36 (a) Nyquist plot of $x\text{MnO}_2\text{-TNTs}$ electrode materials with different MnO_2 content. (b) The equivalent circuit fitted and (c) enlargement of impedance.

Table 4.7 Fitted equivalent circuit elements of $\text{MnO}_2\text{-TNTs}$ electrode materials.

Electrode materials	R_s (Ω)	R_{ct} (Ω)	Z_W (Ω)	CEP (Ω)	Z_T (Ω)	χ^2
80C_xMnTNTs						
$x = 0.005\text{M}$	12.04	0.8	16.67	6796.71	1.81	0.005
$x = 0.01\text{M}$	8.05	1.25	8.60	840.12	1.19	0.003
$x = 0.05\text{M}$	10.35	1.05	3.28	539.78	0.71	0.001

Nyquist plot, representing the impedance behavior as a function of frequency. A semicircle in the high-to-medium frequencies region and a straight line in the low frequency range. This occurring in $x\text{MnTNTs}$ where $x = 0.01\text{M}$ and 0.05M electrodes. The R_{ct} obtained from EIS fitted as in Table 4.7, the increasing R_{ct} with increasing of MnO_2 content on TNTs. The increasing R_{ct} with the increasing mass loading confirms

would affect the composites rate capacity (Lv *et al.*, 2012). The effective of MnO₂-TNTs electrode materials when MnO₂ increasing were compare with the energy storage conversions as show in figure 4.37. However, the literature review about this electrode materials and condition testing will discussion on Table 4.8.

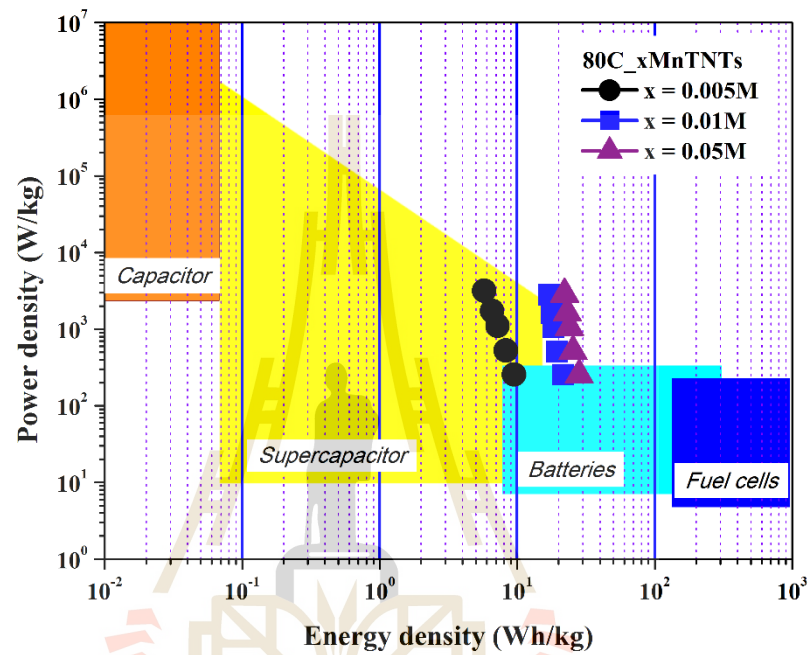


Figure 4.37 Ragone plot for MnO₂-TNTs electrode materials as a various of MnO₂ contents comparison.

Table 4.8 Comparison the specific capacitance of MnO₂-TiO₂ electrode materials were synthesized by hydrothermal method at 1 A/g.

Materials	Hydrothermal condition	Cs (F/g)	Reference
MnO ₂ nanospheres	60 °C 12h	180.00	Liu <i>et al.</i> (2012)
MnO ₂ nanoflowers	160 °C 12h	197.00	Zhao <i>et al.</i> (2015)
MnO ₂	120 °C 16h	200.00	Zhang <i>et al.</i> (2014)
MnO ₂	200 °C 16h	106.25	
MnO ₂ nanotubes	140 °C 24h	325.00	Huang <i>et al.</i> (2014)
TiO ₂ -MnO ₂	160 °C 5h	128.40	Luo <i>et al.</i> (2013)
MnO ₂ /TiO ₂	140 °C 24h	250.00	Zhang <i>et al.</i> (2014)
MnO ₂ /H ₂ Ti ₃ O ₇	140 °C 24h	132.00	
MnO ₂ /TiO ₂	140 °C 24h	286.69	Zhu <i>et al.</i> (2015)
(0.01M) MnO ₂ -TNTs	80 °C 24h	140.22	This work
(0.05M) MnO ₂ -TNTs	80 °C 24h	183.48	
(0.01M) MnO ₂	80 °C 24h	152.35	

CHAPTER V

CONCLUSION

5.1 Synthesis of MnO₂-TNTs materials

Hydrothermal method with TiO₂ solution treated that was highly concentrated hydroxide ions and without sacrificial templates are pathway to synthesis TNTs. And TNTs use as precursor for MnO₂-TNTs composited materials, this leads us to conclude that long terms environments are extremely important for TNTs applications at lower structure maintained of TNTs is 130°C. The completely form of MnO₂-TNTs composition phases although different hydrothermal temperature are occurrence under lower the temperature reaction of TNTs. MnO₂ can be indexed with Birnessite-type MnO₂ while TNTs corresponding to H₂Ti₂O₅·H₂O. Higher that transforms to TiO₂ with MOOH phases, as the characteristic of tubular became some rice shape and MnO₂ nanoflakes are constriction. After hydrothermal temperature for MnO₂ combine with TNTs shows surprising that physical observation brown/yellow solution at low temperature then into precipitation with increasing of temperature. As same as in composition ratio effect, high content MnO₂ show clearly precipitate solution. These represented to the completely formation and phase change of MnO₂-TNTs materials. The hydrothermal synthesis in this research is a simple synthesis, starting materials is low cost and large amount of product.

At lowest temperature treatment (60°C) the MnO_2 -TNTs phases may be incompletely combining phase because of brown solution does not create precipitation as other. The water molecule or OH group on surface and structure of MnO_2 -TNTs were confirm the normally structure in these materials. Both of that are layered structure which contains interlayer water or hydroxyl group on the surface and interlamellar water was lost at high temperature synthesis. Hydrothermal temperatures affect their electrochemical properties based on highest specific capacitance give rise to the optimization temperature of hydrothermal treatment. This temperature was chosen for study the effect of MnO_2 contents with TNTs. Further increasing the KMnO_4 concentration by 0.005M, 0.01M, and 0.05M give rise to large amount MnO_2 contents. The increase number in MnO_2 showed a decrease in the surface area.

5.2 MnO_2 -TNTs electrode materials

MnO_2 -TNTs electrode supercapacitors constructed on Ni foam as working electrode. Three-electrode system with potential-galvanostatic workstation perform in the Na_2SO_4 solution as neutral aqueous electrolytes (green electrolyte). The concentration of Na_2SO_4 was considered on dissolution of MnO_2 into the electrolyte that 0.5M was selected of the electrolyte. The electrochemical measurement stable and reduce the loss of dissolution after 1000 cycle. This is a normal problem of MnO_2 electrode materials with Na_2SO_4 aqueous electrolytes which fresh always with used in 1M Na_2SO_4 .

Different rating scans the area of CV curve corresponds to volume metric specific capacitance. Redox peak occurrence relates with electrode materials that

synthesis at low temperature. The density of current applied on charge-discharge show that longest time as same as result in CV. Specific capacitance show highest in MnO₂-TNTs were synthesized at 80°C in accordance with largest specific surface area. Whereas highest long time stable in cycles test show the best in MnO₂-TNTs was synthesized at 100°C. This condition is the completely phase composition and show highest total pore volume and largest mean pore diameter. However, the specific capacitance decreases with increasing hydrothermal temperature since loss of layered structure and has been phase transition.

Composition ratios effect on electrochemical properties, highly MnO₂ on TNTs exhibited high specific capacitance and good stability. TNTs does not improve the stability of MnO₂, and this are not related to the specific surface area, total pore volume and mean pore diameter. These confirm the highly effective of MnO₂ electrode materials without TNTs effect. However, MnO₂-TNTs has been successfully as the electrode material for supercapacitor application.

5.3 Suggestion

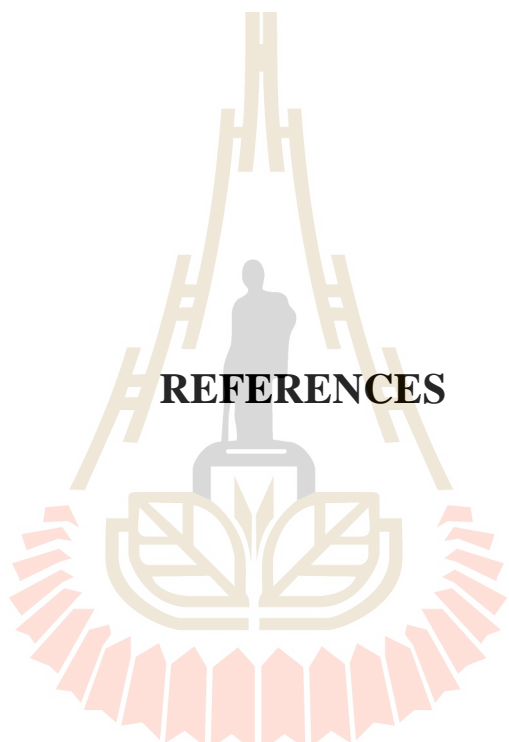
MnO₂-TNTs materials successfully synthesized by hydrothermal method and fabricated as working electrode. Characterization techniques assist explaining MnO₂-TNTs materials and relate with their electrochemical properties. The electrochemical studied for applying supercapacitor shows that the combination of MnO₂-TNTs stability depends on the MnO₂ materials. This because of TNTs materials is low active in electrochemical properties as in the results of specific capacitance calculated and the cycling stability. Additional suggestion following as

5.3.1 To study $\text{MnO}_2\text{-TiO}_2$ electrode materials by annealing or calcining the TNTs before combining because TiO_2 may be high crystallinity.

5.3.2 The limits of potential range therefor let moves to use new reference electrode and new electrolyte as KOH, LiOH, or NaOH and so forth.

5.3.2 Choose new substrate material with hierarchically MnO_2 for improving their stability.





REFERENCES

มหาวิทยาลัยเทคโนโลยีสุรนารี

REFERENCES

- Ali, G. A. M., Tan, L. L., Jose, R., Yusoff, M. M. and Chong, K. F. (2014). Electrochemical performance studies of MnO₂ nanoflowers recovered from spent battery. **Materials Research Bulletin**. 60: 5-9.
- Aziz, M. and Ismail, A. F. (2017) **X-Ray Photoelectron Spectroscopy (XPS)**. In Membrane Characterization(Eds, Hilal, N., Ismail, A. F., Matsuura, T. and Oatley-Radcliffe, D.) Elsevier, pp. 81-93.
- Aziz, R. A., Misnon, I. I., Chong, K. F., Yusoff, M. M. and Jose, R. (2013). Layered sodium titanate nanostructures as a new electrode for high energy density supercapacitors. **Electrochimica Acta**. 113: 141-148.
- Bartłomiejczyk, M. and Mirchevski, S. (2014) Reducing of energy consumption in public transport-Results of experimental exploitation of super capacitor energy bank in Gdynia trolleybus system. In **2014 16th International Power Electronics and Motion Control Conference and Exposition**. (pp. 94-101).
- Bavykin, D. V. and Walsh, F. C. (2009). Elongated titanate nanostructures and their applications. **European Journal of Inorganic Chemistry**. 2009(8): 977-997.
- Bouyanfif, A., Liyanage, S., Hequet, E., Moustaid-Moussa, N. and Abidi, N. (2018). Review of FTIR microspectroscopy applications to investigate biochemical changes in *C. elegans*. **Vibrational Spectroscopy**. 96: 74-82.
- Cesano, F., Bertarione, S., Uddin, M. J., Agostini, G., Scarano, D. and Zecchina, A. (2009). Designing TiO₂ based nanostructures by control of surface morphology

- of pure and silver loaded titanate nanotubes. **The Journal of Physical Chemistry C.** 114(1): 169-178.
- Charinpanitkul, T., Lorturn, P., Ratismith, W., Viriya-empikul, N., Tumcharern, G. and Wilcox, J. (2011). Hydrothermal synthesis of titanate nanoparticle/carbon nanotube hybridized material for dye sensitized solar cell application. **Materials Research Bulletin.** 46(10): 1604-1609.
- Chen, Q., Du, G., Zhang, S. and Peng, L.-M. (2002). **The Structure of Trititanate Nanotubes.** Acta Crystallographica Section b: Author(s).
- Chen, Q., Du, G., Zhang, S. and Peng, L.-M. (2002). The structure of trititanate nanotubes. **Acta Crystallographica Section B: Structural Science.** 58(4): 587-593.
- Ching, S., Petrovay, D. J., Jorgensen, M. L. and Suib, S. L. (1997). Sol-gel synthesis of layered birnessite-type manganese oxides. **Inorganic Chemistry.** 36(5): 883-890.
- Choi, M. G., Lee, Y.-G., Song, S.-W. and Kim, K. M. (2010). Lithium-ion battery anode properties of TiO₂ nanotubes prepared by the hydrothermal synthesis of mixed (anatase and rutile) particles. **Electrochimica Acta.** 55(20): 5975-5983.
- Chu, A. and Braatz, P. (2002). Comparison of commercial supercapacitors and high-power lithium-ion batteries for power-assist applications in hybrid electric vehicles: I. Initial characterization. **Journal of Power Sources.** 112(1): 236-246.
- Conway, B. and Pell, W. (2003). Double-layer and pseudocapacitance types of electrochemical capacitors and their applications to the development of hybrid devices. **Journal of Solid State Electrochemistry.** 7(9): 637-644.

- Cui, L., Wang, Y., Shu, X., Zhang, J., Yu, C., Cui, J., Zheng, H., Zhang, Y. and Wu, Y. (2016). Supercapacitive performance of hydrogenated TiO₂ nanotube arrays decorated with nickel oxide nanoparticles. **RSC Advances**. 6(15): 12185-12192.
- Cullity, B. D. and Stock, S. R. (2001). **Elements of X-Ray Diffraction (3rd Edition)**. Canada: Pearson.
- de Assumpção Pereira-da-Silva, M. and Ferri, F. A. (2017) **Scanning Electron Microscopy**. In Nanocharacterization Techniques(Eds, Da Róz, A. L., Ferreira, M., de Lima Leite, F. and Oliveira, O. N.) William Andrew Publishing, pp. 1-35.
- Engelhard, M. H., Droubay, T. C. and Du, Y. (2017) **X-Ray Photoelectron Spectroscopy Applications**. In Encyclopedia of Spectroscopy and Spectrometry (Eds, Lindon, J. C., Tranter, G. E. and Koppenaal, D. W.) Academic Press, Oxford, pp. 716-724.
- Fang, D., Huang, K., Liu, S. and Li, Z. (2008). Electrochemical properties of ordered TiO₂ nanotube loaded with Ag nano-particles for lithium anode material. **Journal of Alloys and Compounds**. 464(1-2): L5-L9.
- Fatemeh Ataherian, K.-T. L., Nae-Lih Wu (2010). Long-term electrochemical behaviors of manganese oxide aqueous electrochemical capacitor under reducing potentials. **Electrochimica Acta**. 55(25): 7429-7435.
- Fernández-Sánchez, C., McNeil, C. J. and Rawson, K. (2005). Electrochemical impedance spectroscopy studies of polymer degradation: application to biosensor development. **Trends in Analytical Chemistry**. 24(1): 37-48.

- Ferreira, V. C., Nunes, M. R., Silvestre, A. J. and Monteiro, O. C. (2013). Synthesis and properties of Co-doped titanate nanotubes and their optical sensitization with methylene blue. **Materials Chemistry and Physics**. 142(1): 355-362.
- Gaillot, A.-C., Flot, D., Drits, V. A., Manceau, A., Burghammer, M. and Lanson, B. (2003). Structure of synthetic K-rich birnessite obtained by high-temperature decomposition of KMnO_4 . I. Two-layer polytype from 800C experiment. **Chemistry of Materials**. 15(24): 4666-4678.
- Gao, P., Metz, P., Hey, T., Gong, Y., Liu, D., Edwards, D. D., Howe, J. Y., Huang, R. and Misture, S. T. (2017). The critical role of point defects in improving the specific capacitance of $\delta\text{-MnO}_2$ nanosheets. **nature communications**. 8: 14559.
- Ghodbane, O., Pascal, J.-L. and Favier, F. (2009). Microstructural effects on charge-storage properties in MnO_2 -based electrochemical supercapacitors. **ACS Applied Materials & Interfaces**. 1(5): 1130-1139.
- Goldstein, J. I., Newbury, D. E., Michael, J. R., Ritchie, N. W., Scott, J. H. J. and Joy, D. C. (2003). **Scanning electron microscopy and X-ray microanalysis**. Springer.
- González, A., Goikolea, E., Barrena, J. A. and Mysyk, R. (2016). Review on supercapacitors: technologies and materials. **Renewable and Sustainable Energy Reviews**. 58: 1189-1206.
- Hameer, S. and Niekerk, J. L. (2015). A review of large scale electrical energy storage. **International Journal of Energy Research**. 39(9): 1179-1195.

- Han, G., Liu, Y., Zhang, L., Kan, E., Zhang, S., Tang, J. and Tang, W. (2014). MnO₂ nanorods intercalating graphene oxide/polyaniline ternary composites for robust high-performance supercapacitors. **Scientific Reports**. 4: 4824.
- He, J., Wang, M., Wang, W., Miao, R., Zhong, W., Chen, S.-Y., Poges, S., Jafari, T., Song, W., Liu, J. and Suib, S. L. (2017). Hierarchical Mesoporous NiO/MnO₂@PANI Core-Shell Microspheres, Highly Efficient and Stable Bifunctional Electrocatalysts for Oxygen Evolution and Reduction Reactions. **ACS Applied Materials & Interfaces**. 9(49): 42676-42687.
- He, X., Yang, C. P., Zhang, G. L., Shi, D. W., Huang, Q. A., Xiao, H. B., Liu, Y. and Xiong, R. (2016). Supercapacitor of TiO₂ nanofibers by electrospinning and KOH treatment. **Materials & Design**. 106: 74-80.
- Hou, L., Yuan, C., Li, D., Shen, L. and Zhang, X. (2011). Ion-exchange synthesis of Co-functionalized titanate nanotubes and their application in electrochemical capacitors. **Materials Letters**. 65(17): 2632-2634.
- Hu, W., Li, L., Li, G., Meng, J. and Tong, W. (2009). Synthesis of titanate-based nanotubes for one-dimensionally confined electrical properties. **The Journal of Physical Chemistry C**. 113(39): 16996-17001.
- Huang, M., Zhang, Y., Li, F., Zhang, L., Ruoff, R. S., Wen, Z. and Liu, Q. (2014). Self-Assembly of Mesoporous Nanotubes Assembled from Interwoven Ultrathin Birnessite-type MnO₂ Nanosheets for Asymmetric Supercapacitors. **Scientific Reports**. 4: 3878.
- Jung, J. H., Kobayashi, H., van Bommel, K. J. C., Shinkai, S. and Shimizu, T. (2002). Creation of Novel Helical Ribbon and Double-Layered Nanotube TiO₂

- Structures Using an Organogel Template. **Chemistry of Materials**. 14(4): 1445-1447.
- Lang, X., Hirata, A., Fujita, T. and Chen, M. (2011). Nanoporous metal/oxide hybrid electrodes for electrochemical supercapacitors. **Nature Nanotechnology**. 6(4): 232.
- Lei, Z., Zhang, J. and Zhao, X. (2012). Ultrathin MnO₂ nanofibers grown on graphitic carbon spheres as high-performance asymmetric supercapacitor electrodes. **Journal of Materials Chemistry**. 22(1): 153-160.
- Li, J., Tang, Z. and Zhang, Z. (2006). Pseudocapacitive characteristic of lithium ion storage in hydrogen titanate nanotubes. **Chemical Physics Letters**. 418(4-6): 506-510.
- Li, L., Luo, J., Liu, Y., Jing, F., Su, D. and Chu, W. (2017). Self-Propagated Flaming Synthesis of Highly Active Layered CuO- δ -MnO₂ Hybrid Composites for Catalytic Total Oxidation of Toluene Pollutant. **ACS Applied Materials & Interfaces**. 9(26): 21798-21808.
- Libich, J., Máca, J., Vondrák, J., Čech, O. and Sedlaříková, M. (2018). Supercapacitors: Properties and applications. **Journal of Energy Storage**. 17: 224-227.
- Liu, J.-L., Fan, L.-Z. and Qu, X. (2012). Low temperature hydrothermal synthesis of nano-sized manganese oxide for supercapacitors. **Electrochimica Acta**. 66: 302-305.
- Liu, N., Shen, J. and Liu, D. (2013). Activated high specific surface area carbon aerogels for EDLCs. **Microporous and Mesoporous Materials**. 167: 176-181.

- Liu, X. Y., Zhou, M., Chen, C. and Zhang, Y. X. (2017). Electrochemical capacitor performance of TiO₂ nanostructures and porous MnO₂ composite supported on carbon fiber paper. **Ceramics International**. 43(13): 10595-10600.
- Lu, M. (2013). **Supercapacitors: materials, systems, and applications**. John Wiley & Sons.
- Lu, X., Yu, M., Wang, G., Zhai, T., Xie, S., Ling, Y., Tong, Y. and Li, Y. (2013). H-TiO₂@MnO₂//H-TiO₂@C Core-Shell Nanowires for High Performance and Flexible Asymmetric Supercapacitors. **Advanced Materials**. 25(2): 267-272.
- Luo, Y., Kong, D., Luo, J., Chen, S., Zhang, D., Qiu, K., Qi, X., Zhang, H., Li, C. M. and Yu, T. (2013). Hierarchical TiO₂ nanobelts@MnO₂ ultrathin nanoflakes core-shell array electrode materials for supercapacitors. **RSC Advances**. 3(34): 14413-14422.
- Lv, P., Zhang, P., Feng, Y., Li, Y. and Feng, W. (2012). High-performance electrochemical capacitors using electrodeposited MnO₂ on carbon nanotube array grown on carbon fabric. **Electrochimica Acta**. 78: 515-523.
- Manfroi, D. C., dos Anjos, A., Cavalheiro, A. A., Perazolli, L. A., Varela, J. A. and Zaghete, M. A. (2014). Titanate nanotubes produced from microwave-assisted hydrothermal synthesis: Photocatalytic and structural properties. **Ceramics International**. 40(9): 14483-14491.
- McKenzie, R. (1971). The synthesis of birnessite, cryptomelane, and some other oxides and hydroxides of manganese. **Mineralogical Magazine**. 38(296): 493-502.

- Meng, C., Gall, O. Z. and Irazoqui, P. P. (2013). A flexible super-capacitive solid-state power supply for miniature implantable medical devices. **Biomedical Microdevices**. 15(6): 973-983.
- Miao, L., Ina, Y., Tanemura, S., Jiang, T., Tanemura, M., Kaneko, K., Toh, S. and Mori, Y. (2007). Fabrication and photochromic study of titanate nanotubes loaded with silver nanoparticles. **Surface Science**. 601(13): 2792-2799.
- Miao, L., Tanemura, S., Huang, R., Liu, C. Y., Huang, C. M. and Xu, G. (2010). Large Seebeck Coefficients of Protonated Titanate Nanotubes for High-Temperature Thermoelectric Conversion. **ACS Applied Materials & Interfaces**. 2(8): 2355-2359.
- Mison, I. I., Aziz, R. A., Zain, N. K. M., Vidhyadharan, B., Krishnan, S. G. and Jose, R. (2014). High performance MnO₂ nanoflower electrode and the relationship between solvated ion size and specific capacitance in highly conductive electrolytes. **Materials Research Bulletin**. 57: 221-230.
- Mohamed, M. M., Khairy, M. and Eid, S. (2016). Activity and stability studies of titanates and titanate-carbon nanotubes supported Ag anode catalysts for direct methanol fuel cell. **Journal of Power Sources**. 304: 255-265.
- Nakahira, A., Kubo, T. and Numako, C. (2010). Formation Mechanism of TiO₂-Derived Titanate Nanotubes Prepared by the Hydrothermal Process. **Inorganic Chemistry**. 49(13): 5845-5852.
- Nesbitt, H. W. and Banerjee, D. (1998). Interpretation of XPS Mn(2p) spectra of Mn oxyhydroxides and constraints on the mechanism of MnO₂ precipitation. **American Mineralogist**. 83(3-4): 305.

- Pandolfo, A. and Hollenkamp, A. (2006). Carbon properties and their role in supercapacitors. **Journal of Power Sources**. 157(1): 11-27.
- Pang, S. C., Anderson, M. A. and Chapman, T. W. (2000). Novel electrode materials for thin-film ultracapacitors: comparison of electrochemical properties of sol-gel derived and electrodeposited manganese dioxide. **Journal of the Electrochemical Society**. 147(2): 444-450.
- Ramadoss, A. and Kim, S. J. (2013). Vertically aligned TiO₂ nanorod arrays for electrochemical supercapacitor. **Journal of Alloys and Compounds**. 561: 262-267.
- Ray, R. S., Sarma, B., Jurovitzki, A. L. and Misra, M. (2015). Fabrication and characterization of titania nanotube/cobalt sulfide supercapacitor electrode in various electrolytes. **Chemical Engineering Journal**. 260: 671-683.
- Reddy, R. N. and Reddy, R. G. (2003). Sol-gel MnO₂ as an electrode material for electrochemical capacitors. **Journal of Power Sources**. 124(1): 330-337.
- Sadri, R., Hosseini, M., Kazi, S. N., Bagheri, S., Zubir, N., Solangi, K. H., Zaharinie, T. and Badarudin, A. (2017). A bio-based, facile approach for the preparation of covalently functionalized carbon nanotubes aqueous suspensions and their potential as heat transfer fluids. **Journal of Colloid and Interface Science**. 504: 115-123.
- Salari, M., Aboutalebi, S. H., Chidembo, A. T., Nevirkovets, I. P., Konstantinov, K. and Liu, H. K. (2012). Enhancement of the electrochemical capacitance of TiO₂ nanotube arrays through controlled phase transformation of anatase to rutile. **Physical Chemistry Chemical Physics**. 14(14): 4770-4779.

- Shao, J., Zhou, X., Liu, Q., Zou, R., Li, W., Yang, J. and Hu, J. (2015). Mechanism analysis of the capacitance contributions and ultralong cycling-stability of the isomorphous $\text{MnO}_2@\text{MnO}_2$ core/shell nanostructures for supercapacitors. **Journal of Materials Chemistry A**. 3(11): 6168-6176.
- Shao, Y., El-Kady, M. F., Sun, J., Li, Y., Zhang, Q., Zhu, M., Wang, H., Dunn, B. and Kaner, R. B. (2018). Design and Mechanisms of Asymmetric Supercapacitors. **Chemical reviews**. 118(18): 9233-9280.
- Shen, Q., Katayama, K., Sawada, T., Yamaguchi, M. and Toyoda, T. (2006). Optical Absorption, Photoelectrochemical, and Ultrafast Carrier Dynamic Investigations of TiO_2 Electrodes Composed of Nanotubes and Nanowires Sensitized with CdSe Quantum Dots. **Japanese Journal of Applied Physics**. 45(6B): 5569-5574.
- Shi, L., Cao, L., Liu, W., Su, G., Gao, R. and Zhao, Y. (2014). A study on partially protonated titanate nanotubes: enhanced thermal stability and improved photocatalytic activity. **Ceramics International**. 40(3): 4717-4723.
- Shirpour, M., Cabana, J. and Doeff, M. (2013). New materials based on a layered sodium titanate for dual electrochemical Na and Li intercalation systems. **Energy & Environmental Science**. 6(8): 2538-2547.
- Sikhwivhilu, L. M., Mpelane, S., Mwakikunga, B. W. and Sinha Ray, S. (2012). Photoluminescence and hydrogen gas-sensing properties of titanium dioxide nanostructures synthesized by hydrothermal treatments. **ACS Applied Materials & Interfaces**. 4(3): 1656-1665.

- Sing, K. S. (1985). Reporting physisorption data for gas/solid systems with special reference to the determination of surface area and porosity (Recommendations 1984). **Pure and Applied Chemistry**. 57(4): 603-619.
- Soumen, D., Kenji, I., Minoru, M. and Minoru, F. (2014). Reply to Comment on 'Europium doping induced symmetry deviation and its impact on the second harmonic generation of doped ZnO nanowires'. **Nanotechnology**. 25(45): 458002.
- Subramanian, V., Zhu, H., Vajtai, R., Ajayan, P. and Wei, B. (2005). Hydrothermal synthesis and pseudocapacitance properties of MnO₂ nanostructures. **The Journal of Physical Chemistry B**. 109(43): 20207-20214.
- Taberna, P., Simon, P. and Fauvarque, J.-F. (2003). Electrochemical characteristics and impedance spectroscopy studies of carbon-carbon supercapacitors. **Journal of the Electrochemical Society**. 150(3): A292-A300.
- Takashima, T., Hashimoto, K. and Nakamura, R. (2012). Mechanisms of pH-dependent activity for water oxidation to molecular oxygen by MnO₂ electrocatalysts. **Journal of the American Chemical Society**. 134(3): 1519-1527.
- Tang, Q., Jiang, L., Liu, J., Wang, S. and Sun, G. (2014). Effect of Surface Manganese Valence of Manganese Oxides on the Activity of the Oxygen Reduction Reaction in Alkaline Media. **ACS Catalysis**. 4(2): 457-463.
- Toupin, M., Brousse, T. and Bélanger, D. (2004). Charge storage mechanism of MnO₂ electrode used in aqueous electrochemical capacitor. **Chemistry of Materials**. 16(16): 3184-3190.

- Umek, P., Korošec, R. C., Jančar, B., Dominko, R. and Arčon, D. (2007). The influence of the reaction temperature on the morphology of sodium titanate 1D nanostructures and their thermal stability. **Journal of Nanoscience and Nanotechnology**. 7(10): 3502-3508.
- Vol'fkovich, Y. M. and Serdyuk, T. (2002). Electrochemical capacitors. **Russian Journal of Electrochemistry**. 38(9): 935-959.
- Vu, T. H. T., Au, H. T., Tran, L. T., Nguyen, T. M. T., Tran, T. T. T., Pham, M. T., Do, M. H. and Nguyen, D. L. (2014). Synthesis of titanium dioxide nanotubes via one-step dynamic hydrothermal process. **Journal of Materials Science**. 49(16): 5617-5625.
- Wang, G., Zhang, L. and Zhang, J. (2012). A review of electrode materials for electrochemical supercapacitors. **Chemical Society Reviews**. 41(2): 797-828.
- Wang, J.-G., Yang, Y., Huang, Z.-H. and Kang, F. (2011). Coaxial carbon nanofibers/MnO₂ nanocomposites as freestanding electrodes for high-performance electrochemical capacitors. **Electrochimica Acta**. 56(25): 9240-9247.
- Wang, Y., Lai, W., Wang, N., Jiang, Z., Wang, X., Zou, P., Lin, Z., Fan, H. J., Kang, F., Wong, C.-P. and Yang, C. (2017). A reduced graphene oxide/mixed-valence manganese oxide composite electrode for tailorable and surface mountable supercapacitors with high capacitance and super-long life. **Energy & Environmental Science**. 10(4): 941-949.

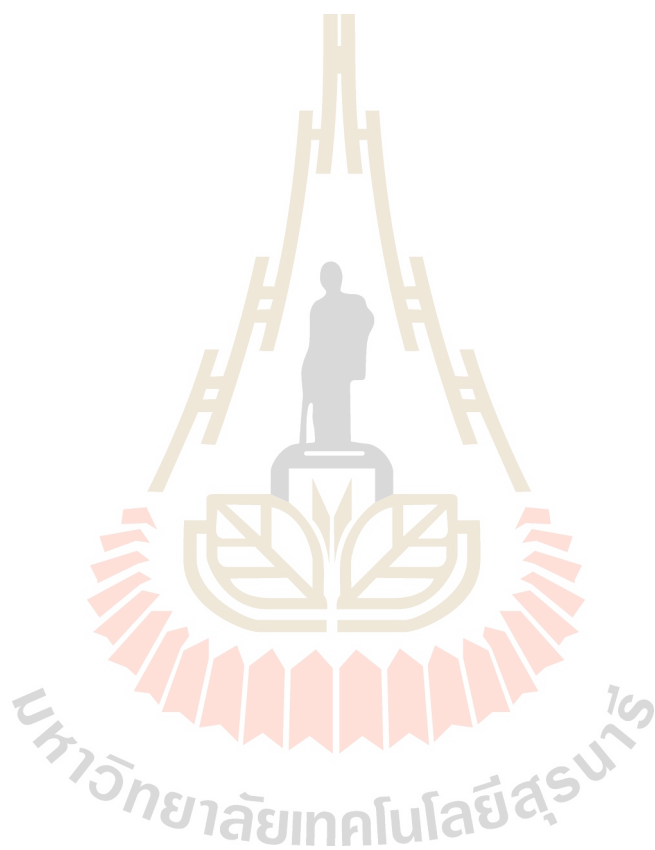
- Wang, Z. L. (2001) **Characterization of nanophase materials**. In Particle & Particle Systems Characterization: Measurement and Description of Particle Properties and Behavior in Powders and Other Disperse Systems, Vol. 18, pp. 142-165.
- Xiong, Q., Zheng, C., Chi, H., Zhang, J. and Ji, Z. (2016). Reconstruction of TiO₂/MnO₂-C nanotube/nanoflake core/shell arrays as high-performance supercapacitor electrodes. **Nanotechnology**. 28(5): 055405.
- Yan, J., Sumboja, A., Wang, X., Fu, C., Kumar, V. and Lee, P. S. (2014). Insights on the fundamental capacitive behavior: a case study of MnO₂. **Small**. 10(17): 3568-3578.
- Yassine, M. and Fabris, D. (2017). Performance of Commercially Available Supercapacitors. **Energies**. 10(9): 1340.
- Ye, Z., Li, T., Ma, G., Peng, X. and Zhao, J. (2017). Morphology controlled MnO₂ electrodeposited on carbon fiber paper for high-performance supercapacitors. **Journal of Power Sources**. 351: 51-57.
- Yılmaz, M. S., Kasap, S. and Pişkin, S. (2013). Preparation, characterization and thermal dehydration kinetics of titanate nanotubes. **Journal of Thermal Analysis and Calorimetry**. 112(3): 1325-1333.
- Yin, J. and Zhao, X. (2008). Electrorheological properties of titanate nanotube suspensions. **Colloids and Surfaces A: Physicochemical and Engineering Aspects**. 329(3): 153-160.
- Yoshida, K., Miao, L., Tanaka, N. and Tanemura, S. (2009). Direct observation of TiO₆ octahedron forming titanate nanotube by advanced transmission electron microscopy. **NANOTECHNOLOGY**. 20(40): 405709.

- Yu, P., Zhang, X., Chen, Y., Ma, Y. and Qi, Z. (2009). Preparation and pseudo-capacitance of birnessite-type MnO_2 nanostructures via microwave-assisted emulsion method. **Materials Chemistry and Physics**. 118(2-3): 303-307.
- Yun, J.-H., Kim, I. K., Ng, Y. H., Wang, L. and Amal, R. (2014). Optical modeling-assisted characterization of dye-sensitized solar cells using TiO_2 nanotube arrays as photoanodes. **Beilstein Journal of Nanotechnology**. 5: 895.
- Zhan, Y., Guo, Y., Zhu, J. and Li, L. (2015). Power and energy management of grid/PEMFC/battery/supercapacitor hybrid power sources for UPS applications. **International Journal of Electrical Power & Energy Systems**. 67: 598-612.
- Zhang, B., Liu, Y., Chang, Z., Yang, Y., Wen, Z. and Wu, Y. (2014). Nanowire $\text{K}_{0.19}\text{MnO}_2$ from hydrothermal method as cathode material for aqueous supercapacitors of high energy density. **Electrochimica Acta**. 130: 693-698.
- Zhang, H., Gao, X., Li, G., Yan, T. and Zhu, H. (2008). Electrochemical lithium storage of sodium titanate nanotubes and nanorods. **Electrochimica Acta**. 53(24): 7061-7068.
- Zhang, L., Lin, H., Wang, N., Lin, C. and Li, J. (2007). The evolution of morphology and crystal form of titanate nanotubes under calcination and its mechanism. **Journal of Alloys and Compounds**. 431(1-2): 230-235.
- Zhang, X., Sun, X., Zhang, H., Li, C. and Ma, Y. (2014). Comparative performance of birnessite-type MnO_2 nanoplates and octahedral molecular sieve (OMS-5) nanobelts of manganese dioxide as electrode materials for supercapacitor application. **Electrochimica Acta**. 132: 315-322.

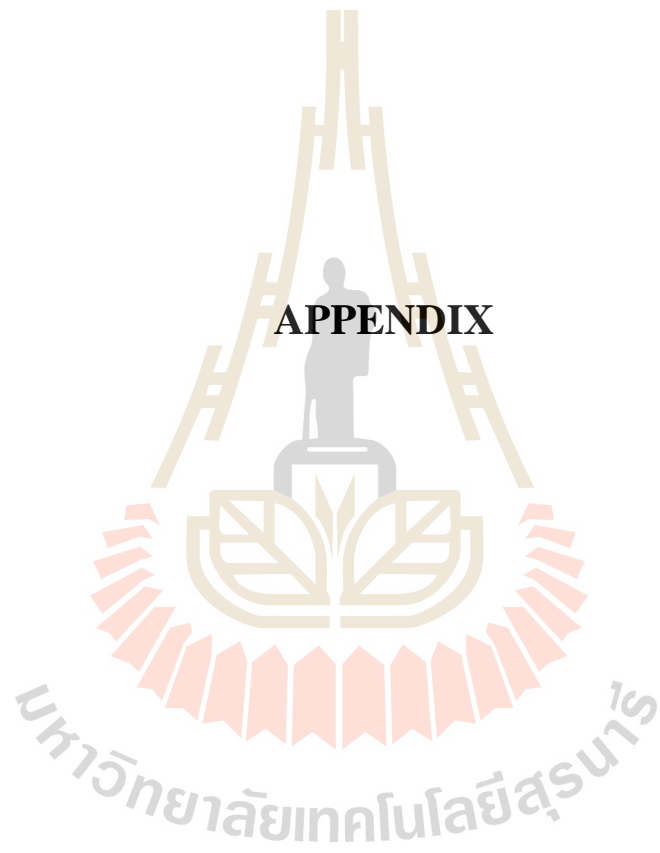
- Zhang, Y., Jiang, Z., Huang, J., Lim, L. Y., Li, W., Deng, J., Gong, D., Tang, Y., Lai, Y. and Chen, Z. (2015). Titanate and titania nanostructured materials for environmental and energy applications: a review. **RSC Advances**. 5(97): 79479-79510.
- Zhang, Y. X., Kuang, M., Hao, X. D., Liu, Y., Huang, M., Guo, X. L., Yan, J., Han, G. Q. and Li, J. (2014). Rational design of hierarchically porous birnessite-type manganese dioxides nanosheets on different one-dimensional titania-based nanowires for high performance supercapacitors. **Journal of Power Sources**. 270: 675-683.
- Zhao, S., Liu, T., Hou, D., Zeng, W., Miao, B., Hussain, S., Peng, X. and Javed, M. S. (2015). Controlled synthesis of hierarchical birnessite-type MnO₂ nanoflowers for supercapacitor applications. **Applied Surface Science**. 356: 259-265.
- Zheng, J., Huang, J. and Jow, T. (1997). The limitations of energy density for electrochemical capacitors. **Journal of the Electrochemical Society**. 144(6): 2026-2031.
- Zhi, M., Xiang, C., Li, J., Li, M. and Wu, N. (2013). Nanostructured carbon–metal oxide composite electrodes for supercapacitors: a review. **Nanoscale**. 5(1): 72-88.
- Zhou, H., Zou, X. and Zhang, Y. (2016). Fabrication of TiO₂@MnO₂ nanotube arrays by pulsed electrodeposition and their application for high-performance supercapacitors. **Electrochimica Acta**. 192: 259-267.
- Zhu, H., Liu, Q., Liu, J., Li, R., Zhang, H., Hu, S. and Li, Z. (2015). Construction of porous hierarchical manganese dioxide on exfoliated titanium dioxide

nanosheets as a novel electrode for supercapacitors. **Electrochimica Acta**. 178: 758-766.

Zhu, T., Zheng, S., Chen, Y., Luo, J., Guo, H. and Chen, Y. (2014). Improvement of hydrothermally synthesized MnO₂ electrodes on Ni foams via facile annealing for supercapacitor applications. **Journal of Materials Science**. 49(17): 6118-6126.



APPENDIX



APPENDIX

PUBLICATION AND PRESENTATION

A.1 List of publication

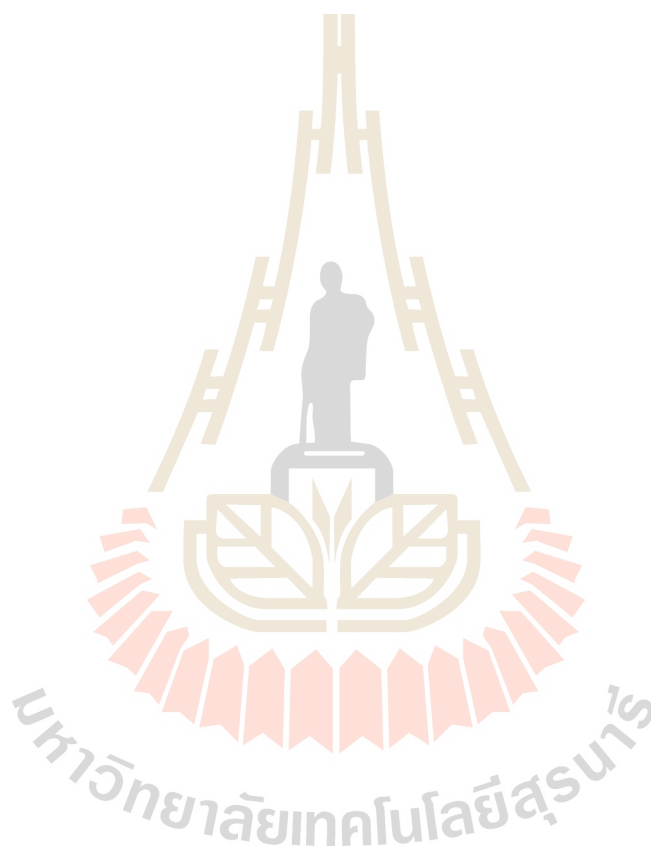
1. **Siwawongkasem, K.**, Prasoetsopha, N., Kasian, P., Wongpratrat, P., Maensiri, S. The Effect of Ag nanoparticles on electrochemical properties of Titanate nanotubes electrode materials, *Materials Today: Proceedings*. (Accepted)

A.2 List of oral presentation

1. **Siwawongkasem, K.**, Prasoetsopha, N., Kasian, P., Wongpratrat, P., Maensiri, S. The Effect of Ag nanoparticles on electrochemical properties of Titanate nanotubes electrode materials. **International Union of Materials Research Society-19th International Conference in Asia**; Oct. 31-Nov. 3, 2018, Bali, Indonesia.
2. **Siwawongkasem, K.**, Prasoetsopha, N., Kasian, P., Wongpratrat, P., Maensiri, S. The Effect of Ag nanoparticles on electrochemical properties of Titanate nanotubes electrode materials; **The First Materials Research Society of Thailand International Conference**; Oct. 31-Nov. 3, 2017 Chiangmai, Thailand.
3. **Siwawongkasem, K.**, Prasoetsopha, N., Kasian, P., Wongpratrat, P., Maensiri, S. Titanate nanotubes-AgO nanocomposites: Synthesis, characterization, and dielectric properties. **The 5th Thailand International Nanotechnology Conference**; Nov. 27-29, 2016, Nakorn Ratchasima, Thailand.

A.3 List of poster presentation

1. **Siwawongkasem, K.**, Prasoetsopha, Maensiri, Synthesis and electrochemical properties of Titanate nanotube loaded with silver nanoparticles. **8th International Workshop on Advanced Materials Science and Nanotechnology (IWAMSN 2016)**; 8th-12th November 2016, Ha Long City, Vietnam.



CURRICULUM VITAE

Name Miss Kwunta Siwawongkasem

Date of Birth August 31, 1992

Place of Birth 55 Moo 15, Tambol Nabua, Nakornthai Didtrict,
Phisanulok, 92110, Thailand.

Educations

2016-2019 Suranaree University of Technology, Nakhon
Ratchasima, Thailand.
Candidate in M.Sc. in Applied Physics

2011-2015 Pibulsongkram Rajabhat Pibulsongkram University,
Phisanulok, Thailand.
B.S. in Physics

มหาวิทยาลัยเทคโนโลยีสุรนารี